The Pennsylvania State University

The Graduate School

Intercollege Graduate Programs in Materials

INTEGRATION OF A PIEZOELECTRIC ULTRASONIC MOTOR INTO A LOW TEMPERATURE COFIRED CERAMIC PACKAGE FOR ACTIVE OPTICAL FIBER ALIGNMENT

A Thesis in

Materials

by

Seung Ho Park

Submitted in Partial Fulfillment
of the Requirements
for the Degree of

Doctor of Philosophy

August 2007

The thesis of Seung Ho Park was reviewed and approved* by the following:

Kenji Uchino
Professor of Electrical Engineering and Materials
Thesis Co-advisor
Co-chair of Committee

Clive A. Randall
Professor of Materials Science and Engineering
Thesis Co-advisor
Co-chair of Committee

L. Eric Cross
Evan Pugh Professor Emeritus of Electrical Engineering

Michael T. Lanagan
Associate Professor of Engineering Science and Mechanics

Heath Hofmann
Associate Professor of Electrical Engineering

Gary L. Messing
Distinguished Professor of Materials Science and Engineering
Head of the Department of Materials Science and Engineering

*Signatures are on file in the Graduate School

ABSTRACT

The major goal of this thesis was to integrate an ultrasonic motor into a ceramic package and demonstrate a useful function of the device. The chosen demonstration was a fiber-optic alignment package that utilized the strengths of the piezoelectric motor, such as its small size, low power consumption, fine position resolution, quick response and high power to weight ratio. In order to demonstrate this functionality a number of key research tasks had to be undertaken.

Specifically, materials development of a low fire, piezoelectric ceramic with properties that would remain stable under high power drive conditions was required. The piezoelectric ceramic had to be processed at a firing temperature that made it compatible with low temperature cofired ceramics (LTCC) and silver electrodes.

A piezoelectric miniaturized motor was designed using the electromechanical properties of piezoelectric ceramic. The motor was designed around two resonance modes that enabled an elliptical motion of the tip, which then permitted the possibility of 2 degrees of freedom when a bimorph structure was used. The motor was designed and optimized using ATILA finite element method (FEM) simulations. The motor design considered the key geometric factors controlling the resonance modes and vibration amplitudes. The motor was also considered with a variety of different electrical drive conditions and the properties were tested with prototyped motors. The properties included resonance behaviors, characterization of displacements, torque, efficiency, and so on. Based on these studies a cofired structure was then developed and similarly characterized.

One of the important goals in this research was to cofire the ultrasonic motor with LTCC in order to create a reliable housing structure with low fabrication costs and facilitate mass production. In order to achieve this, various thermal, mechanical and structural factors were considered during a cofiring process. Finally, the ultrasonic motors were successfully cofired with commercial LTCC green tapes as well as with silver electrodes without encountering delamination or bending problems.

In the final part of the thesis, a LTCC packaged structure was designed and fabricated with the integrated piezoelectric motors. These motors were then driven with a computer controlled circuit that was designed to aid a procedure aimed at optical alignment between a fiber and a laser. Once alignment was achieved, a pre-stressed structure with springs maintained the position of the fiber without any external electrical field or adhesive material. This package design provided a unique ability to adjust and realign an optical fiber in the case where misalignment occurs during installation or use. The optical package was characterized for thermal stability over a temperature ranging from room temperature to 50 ^{o}C.

TABLE OF CONTENTS

LIST OF FIGURES

LIST OF TABLES

ACKNOWLEDGEMENTS

First of all, I deeply appreciate invaluable support and guidance from my advisors, Prof. Kenji Uchino and Prof. Clive A. Randall. They provided great suggestions and encouragement that made this thesis possible. Prof. Uchino's passion for the research has made a deep impression on me. I owe him lots of gratitude for having me shown the way of real research. I would like to express my deepest regards for Prof. Randall. He has been a great mentor all along. He taught me how to think and discuss in scientific manner without loosing contact with real world. Every meeting with him was a moment of joy for learning something new. He was always enthusiastic in the progress of my work and was available when I needed his advises.

I would also like to thank the members of my Ph. D. committee who took effort in reading my thesis and providing me with valuable comments: Prof. L. Eric Cross, Prof. Michael Lanagan and Prof. Heath Hofmann. I am very thankful to Prof. Cross for his encouragement and guidance on several occasions. I would like to express my gratitude to Prof. Lanagan who has always reminded me of important points in the research. I am thankful to Prof. Hofmann for helpful discussion and support. I thank you all.

I would like to thank my colleagues Seyit Onurhan Ural, Safakcan Tuncdemir and Aditya Rajapurkar for their incredible support. Seyit helped me from my first time in International Center for Actuators and Transducers and still one of the most helpful guys. His kindness and generosity is beyond expectation. I will miss the happy hour with my friends in ICAT.

I wish to thank my family. I would like to thank my parents for their support through my life. They gave me unconditional love and trust so that I can endure through any difficulties and overcome any obstacles. Thank you and I love you.

Finally, I would like to acknowledge the funding from the Center for Dielectric Studies, Center for Optical Technologies and the Office of Naval Research.

Chapter 1

INTRODUCTION

1.1 High Power Piezoelectrics

High power devices, such as ultrasonic motors, are usually driven with a high electric field and a high vibration level, which are associated with significant heat generation [**1**,**2**]. This chapter presents a brief introduction to piezoelectricity and relevant research trends in high power piezoelectric materials and low temperature sintering.

1.1.1 Piezoelectricity

In 1880, Pierre and Jacques Curie reported the first experimental results demonstrating the piezoelectric effect, using specially prepared crystals, such as quartz, tourmaline, cane sugar, and Rochelle salt. Mechanical stress on these crystals successfully induced a surface charge, later, this was called the “the direct piezoelectric effect”, which illustrates electrical charge generation based on applied mechanical stress. In contrast to direct piezoelectricity, converse piezoelectricity demonstrates a phenomenon wherein the application of an electrical field creates mechanical strain. In 1881, Lippman mathematically proved the converse piezoelectric effect, using fundamental thermodynamic principles: the Curie’s quickly confirmed this effect. Quantitative proof of the complete reversibility of electro-elasto mechanical deformations in piezoelectric crystals was also later obtained [**3**].

In crystallography, combinations of symmetry elements that can compatibly pass through a common point are called point groups, and only 32 non-identical point groups are possible [**4**]. The structural symmetry of a crystal geometrically affects its structural and physical properties, for instance, its dielectric, elastic, piezoelectric, thermal and optic properties, etc. The 32 point groups can be categorized into 11 centrosymmetric types and 21 non-centrosymmetric types. A crystal with a symmetric center does not show any third rank tensor properties such as piezoelectricity, d_{ijk}. Among these crystals, 20 exhibit finite piezoelectric effects and 10 have only one unique polar direction. Along the unique axis, a polarity is obtained with finite pyroelectric effects. When the equilibrium spontaneous polarizations exist and can be reoriented by an external electric field with sufficient strength, these materials are termed ferroelectric [**5**,**6**,**7**].

The application of stress on a non-centrosymmetric crystal exhibits a movement of the positive and negative ions with respect to each other, generating an electric charge difference at the surface of the material. This is the generator action through which we obtain the direct piezoelectric effect: the conversion of mechanical energy into electrical energy [**8**]. In contrast, when an electric field is applied to a crystal, either a compressive or tensile strain is produced in the material, depending on the direction of the field and the size of the respective piezoelectric coefficients. This motion is the actuator or motor action through the converse piezoelectric effect: the conversion of electrical energy into mechanical energy.

Ferroelectricity can exist in a number of crystal structures and compositions within those structures. One of the most important structures is perovskite. Perovskite is the name of the mineral calcium titanate ($CaTiO_3$), a non-ferroelectric material. Most of

the useful piezoelectric and ferroelectric ceramics, such as barium titanate, ($BaTiO_3$) potassium niobate ($KNbO_3$), and lead titanate ($PbTiO_3$) have perovskite-type structures. These oxide ceramics have the general formula ABO_3, where O represents oxygen, A represents a cation with a larger ionic radius in twelve-fold coordination, and B represents a cation with a smaller ionic radius in octahedral six-fold coordination. Figure **1.1** shows a cubic ABO_3 perovskite-type unit cell.

The first piezoelectric ceramic with perovskite is barium titanate, which shows anomalous dielectric properties. Other materials such as $PbTiO_3$, $KNbO_3$ and $(K,Na)NbO_3$ have also been studied for their piezoelectric applications in single crystal and polycrystalline form [**5**]. The performance of these materials, however, is insufficient for practical applications. The discovery of lead zirconate titanate ($Pb(Zr_xTi_{1-x})O_3$) ceramics by Jaffe et al. in 1954 led to the wide usage of piezoelectricity possible in polycrystalline materials. This composition is adjacent to the morphotropic phase boundary (MPB). The MPB compositions have relatively temperature-independent phase boundaries between ferroelectric phases and high symmetric phases. The polycrystalline solids can be easily poled due to the large number of polarization directions that can be utilized. Moreover the phase boundary reduces anisotropy energy, which reduces domain wall energy and thus increases wall mobility. In turn, this provides a high extrinsic domain wall contribution to electromechanical properties [**9**].

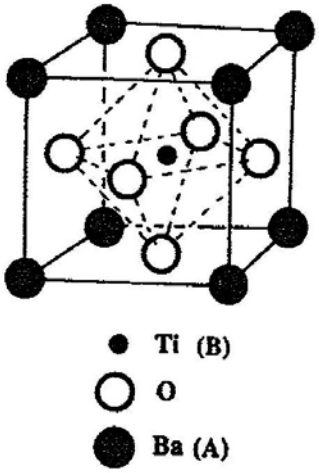

Figure **1.1**: A cubic ABO_3 perovskite-type unit cell

A variety of compositional modifications of PZT-based ceramics have been made to enhance and to optimize dielectric and piezoelectric properties for specific applications. PZT ceramics can be categorized into two groups: 'hard' and 'soft.' Generally, acceptor ions make 'hard' PZTs, which have a small displacement at off-resonance strain, but a large strain with a resonance condition, low dielectric loss, and high mechanical quality factor ($Q_m = 1/\tan\delta_m$). They are suitable for ultrasonic applications, such as ultrasonic welders and ultrasonic motors. On the other hand, 'soft' PZTs present a large strain at off-resonance, a high dielectric loss, and a low mechanical quality factor. Off-resonance devices, such as multi-layer actuators, are the main applications for these materials. Further modifications can be made to manipulate the transition of the ferroelectric phases, in order to enhance electromechanical properties, but this results in increased loss and temperature dependence.

1.1.2 High Power Piezoelectric Materials

Recently, high power piezoelectric devices, such as piezoelectric actuators, ultrasonic motors, and piezoelectric transformers, have been intensively developed. For example, a transformers for LCD panel applications as shown in figure **1.2** [**10**,**11**,**12**]. These high power devices are usually driven under a high electric field to obtain a high vibration level; consequently, significant heat is generated from the dielectric and mechanical losses. The maximum mechanical energy density generated in a piezoelectric ceramic material can be evaluated by the maximum vibration velocity, v_o, above which the temperature rise in the piezoelectric exceeds 20^{o}C above room temperature. The vibration velocity is proportional to the mechanical quality factor, Q_m, piezoelectric constant, d, and applied electric field, E.

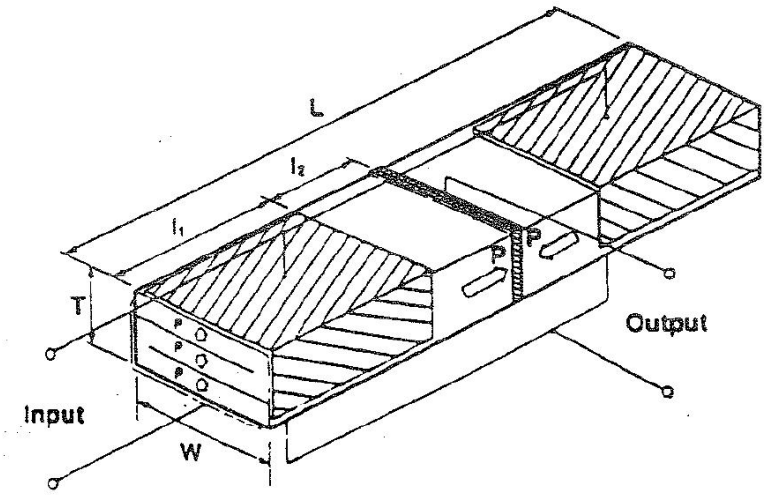

Figure **1.2**: Multilayer type transformer by NEC [**12**].

There are three different kinds of Figures-of-Merit (FOM) for evaluating high power characteristics. (1) For piezoelectric actuators used with DC or Slow-AC, off-resonance state, the piezoelectric strain constant, d, or electromechanical coupling factor, k, is a primary FOM, and (2) for ultrasonic motors, the maximum vibration velocity v_0 is the FOM, while (3) for piezoelectric transformers, the product of v_0 and k is the FOM, because the converted mechanical energy (at resonance) must be re-converted to electrical energy at a rate of k^2 [**1**,**2**]. The Figures-of-Merit are summarized in table **1.1**.

Table **1.1**: Figures-of-Merit for high power devices

Applications	Figures-of-Merit (FOM)
Actuator	High piezoelectric constant, d High electromechanical coupling factor, k
Ultrasonic Motor	High vibration velocity, v_0
Transformer	High vibration velocity, v_o High electromechanical coupling factor, k

Previously, much effort has been put forth to developing "soft" lead zirconate titanate (PZT) ceramics with a high piezoelectric constant d and a high electromechanical coupling factor k and transition temperature T_c. One of the most important materials developed is the $Pb(Zr,Ti)O_3$-$Pb(Ni_{1/3}Nb_{2/3})O_3$ system developed by NEC in Japan, which is widely used for cofired multilayer actuators [**13**]. In contrast, in the 1990s, such efforts were shifted to "hard" PZT with a high Q_m, aiming at ultrasonic motor (USM) and piezoelectric transformer applications. One of the materials developed was the rare-earth (e.g., Yb and Eu) doped $Pb(Zr,Ti)O_3$-$Pb(Mn_{1/3}Sb_{2/3})O_3$ system, which exhibits a maximum vibration velocity of more than 1 m/s, which is more than 3 times higher than those of commercially available "hard" PZTs [**14**]. However, because these PZT-PMnS ceramics do not possess a high d or k, the superiority of the transducer performance

(coupling effect of converse and direct piezoelectric effects, such as in piezoelectric transformers) was not as great as initially hoped.

In the last decade new research has focused on 'hard' and 'soft' compromised piezoelectric ceramics with relatively high d and k that maintain a maximum vibration velocity around 0.6 m/s. The $Pb(Zr,Ti)O_3$-$Pb(Zn_{1/3}Nb_{2/3})O_3$-$Pb(Ni_{1/3}Nb_{2/3})O_3$ system near the morphotropic phase boundary (MPB) is one of the most promising materials, because of its ability to significantly suppress heat generation during a large vibration level drive with reasonable electromechanical coupling factors. In particular, $0.8Pb(Zr,Ti)O_3$-$0.16Pb(Zn_{1/3}Nb_{2/3})O_3$-$0.04Pb(Ni_{1/3}Nb_{2/3})O_3$ + 0.5wt% MnO_2 was reported for its good piezoelectric properties of k_p=0.554, Q_m=1502, and d_{33}=265 pC/N [**15**]. Furthermore, this composition is utilized as a base composition for low sintering temperature piezo-ceramics [**16**].

1.1.3 Low Temperature Sintering of Piezoelectric Ceramics

The sintering temperature of lead zirconate titanate PZT-based hard compositions is usually very high (approximately above 1200^{o}C) in comparison with that of soft PZTs. Thus, a Ag/Pd alloy is usually used as the electrode to suppress the migration of Ag into the ceramics or the oxidation of the base metal Cu at high temperature.

For a multilayer type piezoelectric transformer application, serious performance degradation was found using Ag/Pd electrodes. The main reason for this is the high resistivity of the Ag/Pd alloy with respect to pure Pd. If pure Ag or base metal Cu can be used for internal electrodes, then enhanced performance can be expected due to higher

conductivity. This is one of the motivations for the low temperature of 'hard' ceramics. Furthermore, low temperature sintering can provide advantages such as reduced energy consumption and the reduced PbO volatilization.

Various techniques were employed by several researchers to obtain low temperature sinterable "soft" PZT compositions. The addition of dopants, which improve solid-state sintering, and the addition of oxides and compounds, which have low melting points for liquid-phase sintering are the most popular strategy [**17**,**18**,**19**]. The other processes, such as sintering in an inert atmosphere followed by hot pressing [**20**], or the use of fine submicron starting powders [**21**], are not generally used due to the expensive, complicated and laborious procedures needed to synthesize them.

Table **1.2 [9]** presents some of the oxides and compounds that have been used for assisting liquid-phase sintering, including $BiFeO_3$+$Ba(Cu_{1/2}W_{1/2})O_3$ [**22**], Li_2CO_3-Bi_2O_3-$CdCO_3$ [**23**], $LiBiO_2$ (melting temperature of 700^oC) [**24**], 4PbO-B_2O_3 [**25**], B_2O_3-Bi_2O_3-CdO [**19**], and PbO + CuO [**26**]. Even though these techniques are able to obtain dense ceramics at low sintering temperatures, the piezoelectric properties are not good enough to be used in industrial mass-production. In the initial and middle sintering stages, low temperature sintering aids form a liquid phase and promote densification. In the final sintering stage, however, additives enter into a lattice that eventually interferes with the dielectric and piezoelectric properties; in general, liquid phase sintering dopants make the PZT "softer." Hence, the low temperature sintering of hard materials was one of the necessary materials development steps in this thesis, before cofiring with LTCC materials to form integrated ultrasonic motors.

Table **1.2**: Liquid phase sintering aids for piezoelectric ceramics

	Addition†	Sintering Temperature*	Melting
PbO	0.1 to 3 wt%	950 to 1000°C	886°C
$LiBiO_2$	0.1 to 1 wt%	780°C to 850°C	700°C
$4PbO–B_2O_3$	0.1 to 0.5 wt%	1150°C	500°C
$5CdO–2SiO_2$	0.5 to 1.0 wt%	1150°C	1100°C
$Pb_5Ge_3O_{11}$	0.2 to 1.0 wt%	950°C to 1000°C	750°C
LiF	0.5 to 2 wt%	950°C to 1050°C	875°C
CuO–PbO	1.0 wt%	950°C to 1000°C	812°C
V_2O_5	0.5 to 1.0 wt%	900°C to 1070°C	675°C
$3Bi_2O_3–B_2O_3$	0.5 to 1.0 wt%	1000°C to 1070°C	542°C
P_2O_5	1 wt%	1100°C to 1150°C	1050°C
$Ba(Cu_{1/2}W_{1/2})O_3$-CuO	0.1 wt%	935°C	800°C

†Addition depends on composition, flux mixing, and particle reactivity.
*Sintering depends on flux amount, flux mixing, particle reactivity, sintering profile.

1.2 Piezoelectric Ultrasonic Motors

Recently, micro motors have been integrated into popular applications, such as cellular phones, digital cameras, and laptop computers, which has accelerated the need for simple, precise, low-cost, and multifunctional piezoelectric ultrasonic motor development [**27**]. Some of the advantages of piezoelectric motors include fast response, high precision (no backlash), a high power-over-weight ratio, the absence of extrinsic or intrinsic magnetic fields, and a smaller package size when compared to conventional electromagnetic motors. Owing to the above, piezoelectric motors are becoming very competitive with electromagnetic motors for sizes below 10 mm.

1.2.1 Background of the Ultrasonic Motor

Electromagnetic motors have actually existed for more than a hundred years. While these motors still dominate the industry, further improvement of suitable new magnetic and superconducting materials will be required for advanced applications. Efficient motors of this type smaller than 1 cm are difficult to produce. An electromagnetic motor with a sub millimeter rotor, used in a wristwatch for example, requires a permanent magnet about 1cm in diameter. The efficiency of piezoelectric ultrasonic motors is independent of their size, and therefore they have gained much attention for miniaturized motor applications [**10**].

The basic structure of an ultrasonic motor is depicted in figure **1.3**. It consists essentially of a high frequency power supply, a stator, and a slider/rotor piece. The stator is composed of a piezoelectric driver and an elastic vibrator. The slider has an elastic moving component with a friction coat on the side facing the stator. The motor is driven by a compact and inexpensive drive circuit, which, in conjunction with its simple design, makes it especially suitable for mass production. The first ultrasonic motor was proposed and demonstrated by H.V. Barth et al. of IBM in 1973 [**28**]. The rotor in this design is in contact with two horns placed on either side of it, as shown in figure **1.4**. When one of the horns is driven by its piezoelectric vibrator, the rotor is driven in one direction, with rotation in the opposite direction occurring when the other horn is driven. Various mechanisms based on virtually the same principle have subsequently been proposed. Ultimately however, the motors of this design were not very useful, due to changes in the vibration amplitude that tend to occur at higher temperatures and the mechanical

degradation that occurs as a consequence. In 1975, Burleigh Instruments patented an inchworm linear motor [**29**]. Even though this motor utilized piezoelectricity, it was not categorized as an ultrasonic motor. The linear motor market was opened up to ultrasonic motors in 1988 by the development of Π-shaped motors that employed a "horse trotting" like motion [**30**,**31**]. Kurosawa et al. (1998) demonstrated a linear motor that used vibrators at right angles (L-shape) and produced higher thrusts and speeds than any previous linear motors [**32**]. One of the objectives of this work is to miniaturize a motor that could potentially be used for alignment in packaged optoelectronics and permit motion in 2-degrees of freedom.

In the 1980's, more precise and sophisticated positioners, which do not generate magnetic field noise, were required by integrated circuit manufacturers as the pattern density on chips continued to increase. This trend helped to accelerate the development of new ultrasonic motors. The merits and demerits of modern ultrasonic motors are summarized in Table **1.3**.

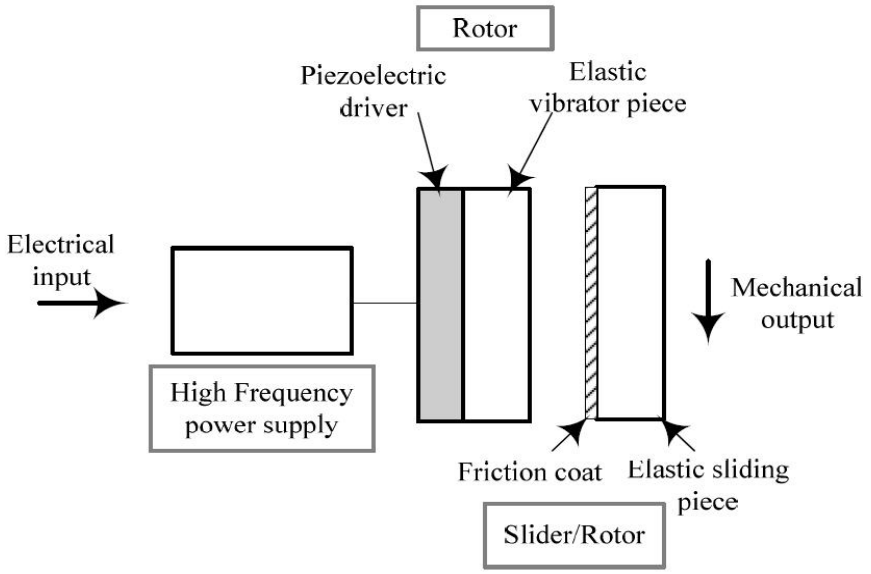

Figure **1.3**: The basic structure of an ultrasonic motor

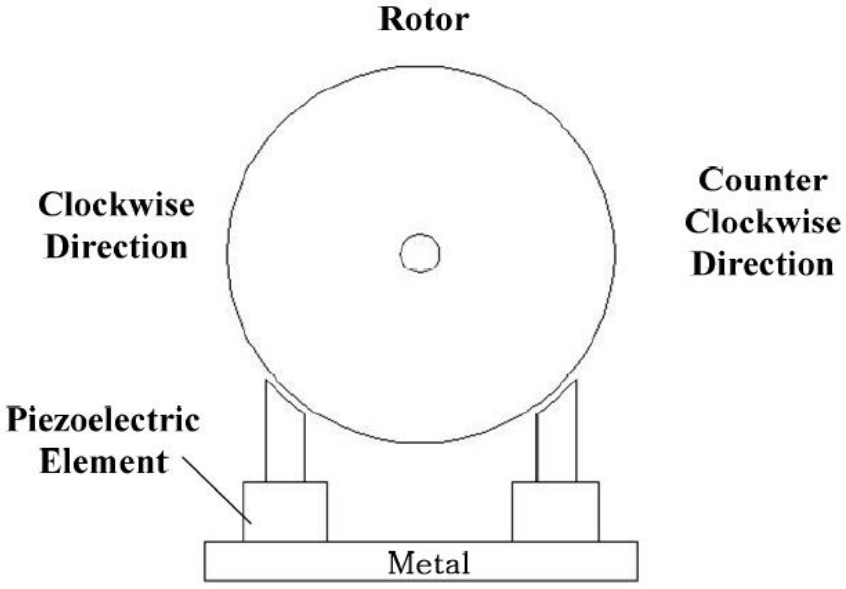

Figure **1.4**: The first practical piezoelectric ultrasonic motor

Table **1.3**: The merits and demerits of the ultrasonic motor

Merits	**Demerits**
Low speed with high torque	High frequency power supply required
Direct drive	Torque vs. speed drop
Quick response	Low durability
Wide range of speeds	Small displacement
Hard braking with no backlash	Spring mechanism required
Excellent controllability	
Fine position resolution	
High power to weight ratio	
Silent drive	
Compact size and light weight	
Simple structure	
Unaffected by external electric	
No magnetic noise	

1.2.2 Classification of Ultrasonic Motors

Depending on the motion induced by the ultrasonic motor vibration, there are generally two types of ultrasonic motors: a rotary type and a linear type. Another criterion for classification is the vibration source: a standing wave or a traveling wave. However, as various ultrasonic motors were developed, new categories were introduced, such as the multi-mode excitation type and mode rotation type [**33**].

The standing wave type motor transfers longitudinal vibration to a rotor or a slider. One of the best known standing wave motors was developed by Sashida et al. in 1982. As shown in figure **1.5**, the impact between the stator and slider/rotor parts causes an indirect bending mode excitation, converting longitudinal vibration into displacement in a desired direction. Rotational direction of the standing wave motor can be controlled by using a stator design as shown in figure **1.6**. It has alternating polarization directions and each region has two contact points with a slider/rotor at the opposite angle.

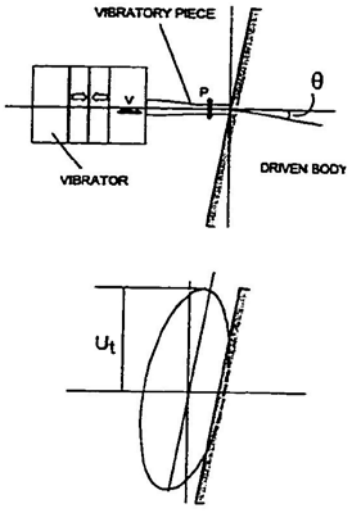

Figure **1.5**: Vibrating piece and elliptical trajectory on the slider surface (Sashida et al., 1980)

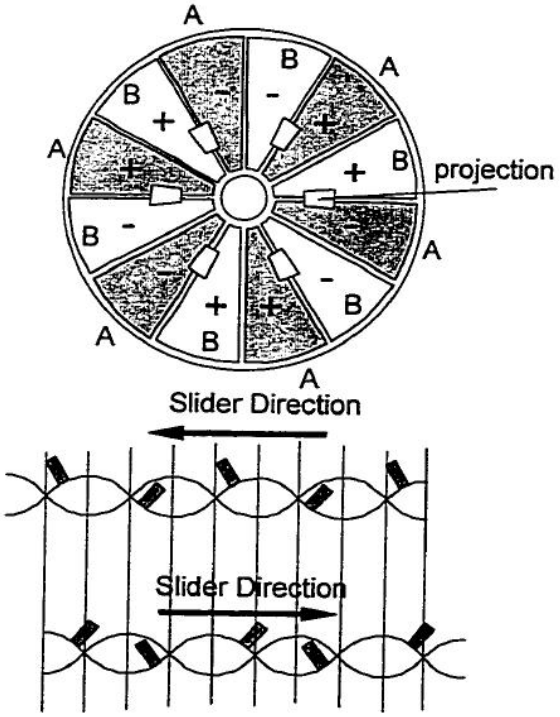

Figure **1.6**: Standing wave type ultrasonic motor with direction change (Takano et al., 1994)

In general, traveling wave type motors use two phases with a 90^{o} phase difference. The standing wave can be described in **Eq.1**, where U is the displacement, A is half of the maximum displacement, k is the wave vector, t is time, and ω is the angular frequency.

$$U_s(x,t)=A[\cos(kx)][\cos(\omega t)] \qquad \text{Eq.}\mathbf{1}$$

while the equation for a traveling wave can be expressed as:

$$U_t(x,t) = A\cos(kx-\omega t) \qquad \text{Eq.}\mathbf{2}$$

Eq.2 can be rewritten as:

$$Ut(x,t)=A[\cos(kx)][\cos(\omega t)]+A[\cos(kx-\pi/2)][\cos(\omega t-\pi/2)] \quad \text{Eq.3}$$

As shown in **Eq.3**, a traveling wave can be obtained by superimposing two standing waves with a 90^{o} phase difference. With the proper pre-stress conditions, an object using a vibrator with a traveling wave can move in the direction of the wave, as shown in figure **1.7**.

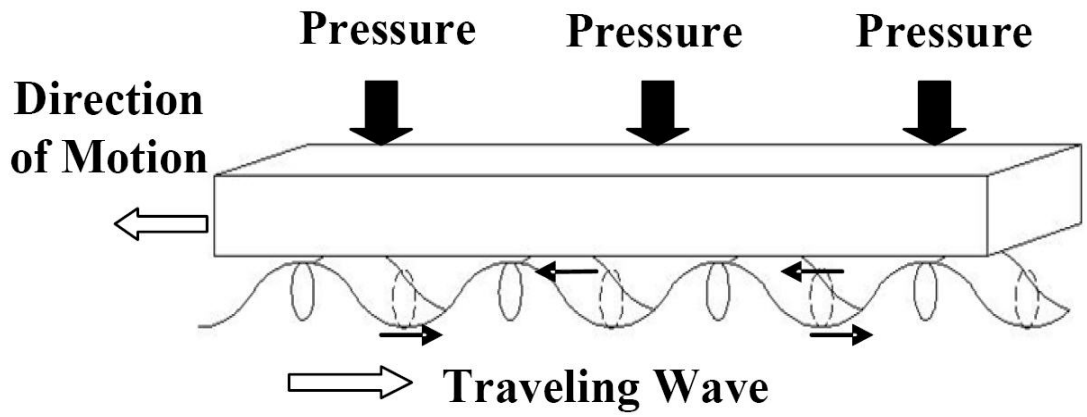

Figure **1.7**: The traveling wave type motor

One of the mode rotation types of ultrasonic motors is the L-shape motor, shown in figure **1.8**. [**32**]. It uses two phases with a 90^{o} phase difference, as in the traveling wave type motor. In this case, two resonance modes, corresponding to vertical and horizontal motion, can be found at the motor tip. By driving the motor with a frequency between the two modes, the two motions are superimposed and an elliptical motion is obtained. This motor showed a higher thrust and speed than previous ultrasonic motors. However, the miniaturization of this motor was difficult because of its metal-ceramic structure, with a bolt joint mechanism.

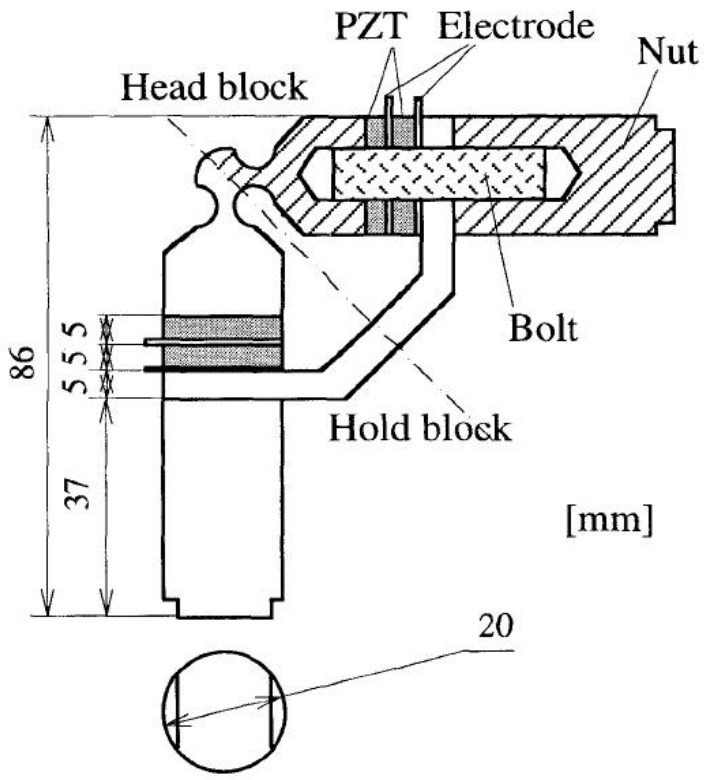

Figure **1.8**: Kurosawa's L-shaped motor

1.2.3 2-degrees of Freedom Ultrasonic Motors

Kurosawa et al. demonstrated a linear motor that uses vibrators at right angles (L-shape) and produces a higher thrust and speed than any previous linear motor [**32**]. This motor, however, has only one degree of freedom.

To increase the versatility of actuators and widen their areas of application, intense research has been carried on within the past 10 years to develop actuators with 2-degrees, or multiple degrees, of freedom. Hu et al. demonstrated an ultrasonic motor with 2-degrees of freedom that has input electrodes divided into four equal parts of a circle

[**34**]. A similar design was used by Aoyagi et al. to control a ball that is placed on the motor using thick film processes [**35**]. Shimoda et al. used four actuators in a pyramid shape for motion with multi-degrees of freedom [**36**]. Later efforts to control a ball in multi-degrees of freedom were also made. These motors stacked piezoelectric rings with alternating polarization directions for longitudinal and bending vibrations [**37**,**38**]. For control of an object in 2-dimensional space with nanometer range control, arrays of standing wave ultrasonic actuators were made on the plane.

However, previous multi-degrees of freedom motors have bulky designs or small thrusts. Hence, in this research, slim and high thrust motors were studied with the objective of integrating them into an LTCC base compact optical fiber alignment package.

1.3 Low Temperature Cofired Ceramics (LTCC)

The technology drive in microelectronic packaging is towards smaller, faster and cheaper devices with increased performance. The transmission of signals in shorter times requires the signal speed to increase, higher frequencies to be used, and distances to be reduced along the transmission line. Additionally, thermal stresses are created due to differences in the thermal expansion behavior of the wide variety of materials used, and these stresses can lead to reliability problems, especially at interfaces. The materials engineering of substrates and components to manage the signal processing of the integrated chip is a continuing challenge [**39**,**40**].

The Low Temperature Cofired Ceramics (LTCC) technique can combine materials that have different characteristics; it is therefore possible to integrate and build different types of components into the ceramic. Furthermore, while it is possible to incorporate low-loss metal into LTCC as a conductor, the ceramic has low dielectric loss at high frequencies, making it effective for achieving low loss performance, compared with other materials such as resin. In addition, its thermal expansion coefficient compared with resin materials and other ceramic materials is low, and it has the merit of excellent connection reliability for high density packaging of Large Scale Integration (LSI) components. For these reasons, LTCC is regarded as a promising technology for the integration of components and substrates for high-frequency applications [**41**]. The advantages and disadvantages of LTCC packaging ceramics are summarized in Table **1.4** [**39**].

Table **1.4**: LTCC packaging advantages and disadvantages [**39**]

Advantages	Disadvantages
Dielectric constants lower than AlN and Al_2O_3, typically 5	The glass-ceramic low-k dielectric are mechanically weaker than alumina Fracture strength 200 versus 350 MPa
Temperature coefficient of expansion can be designed close to Si (3 ppm/^oC) and is also tunable to GaAs (6 ppm/^oC)	The thermal conductivities are lower than that of alumina (15 versus 25 W/mK)
With low temperatures (900^oC) higher conductivity metals such as gold, silver, silver/palladium and copper can be used	The dielectric loss is higher than in polymer and pure phase ceramic materials
With the exception of copper, the LTCC can be fired in air, therefore, giving a much simpler cofiring process than in high-fire packages	
Ability to cofire capacitive and resistor components	
Plating and associated processes are eliminated because chip bonding can be done directly on as-fire conductors	

1.4 Cofiring of PZT with Low Temperature Cofired Ceramics (LTCC)

There were previously several attempts to cofire PZT based devices with LTCC substrate materials. However, a serious inter-diffusion problem and low density were revealed. Hrovat et al. investigated the inter-diffusion of PbO and SiO_2 upon cofiring [**42**,**43**]. The reducing effect on the dielectric constant was also studied. Juuti et al. measured d_{33} and d_{31} values for $(Pb,La)(Zr,Ti)O_3$ cofired with an aluminum oxide substrate, as shown in figure **1.9** [Error! Not a valid link.]. Zarnik et al. used an Al_2O_3 barrier to reduce the inter-diffusion between PZT and LTCC during the cofiring process [**45**]. Golonka et al. investigated the inter-diffusion tendency of PZT and LTCC with various electrode materials [**46**]. Previously, cofiring research focused on cantilever type actuators, with no practical research on cofiring an ultrasonic motor within an LTCC structure. This research is focused on the ambitious development of a compact, slim and simple motor with 2-degrees of freedom integrated into LTCC.

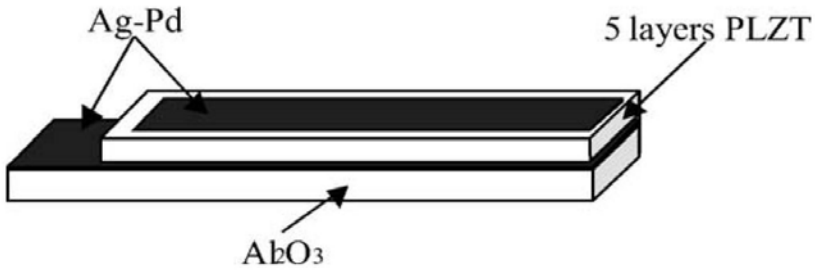

Figure **1.9**: Configuration of PLZT with Al_2O_3 sample [**44**]

1.5 Optical Fiber Alignment

Currently, commercial optical packaging manufacturers are utilizing costly robotic alignment stations with complex computer algorithms to perform fiber alignment [**47**,**48**]. Alignment is then fixed using either UV cured epoxies or laser welding [**49**]. This is a time-consuming iterative process, commonly requiring extensive rework due to initial stress relaxation in the curing epoxy or during cooling following a laser welding process. The total cost of alignment, rework and consistently low yields can add nearly an order of magnitude to the final product cost. Innovation in current packaging technologies through integrating functional materials is necessary for the continued advancement of the optical communications industry.

The major technical challenge in optoelectronic packaging is laser-fiber, fiber-fiber, and fiber-detector alignment. These connections require high optical coupling efficiency and long-term stability for optical communications networks. Passive alignment is a cheap, fast, and simple aligning solution [**50**,**51**]. In order to obtain the desired coupling efficiency, alignment tolerances of <100 nm are required. This is very difficult to obtain with passive alignment. Active alignment is another way of coupling optical fibers. Various actuation mechanisms, such as electrostatic force, shape memory alloy, piezoelectric effect and thermal expansion, were used for the active alignment [**52**,**53**,**54**,**55**]. Figure **1.10** shows the alignment of optical axis with electrostatic force.

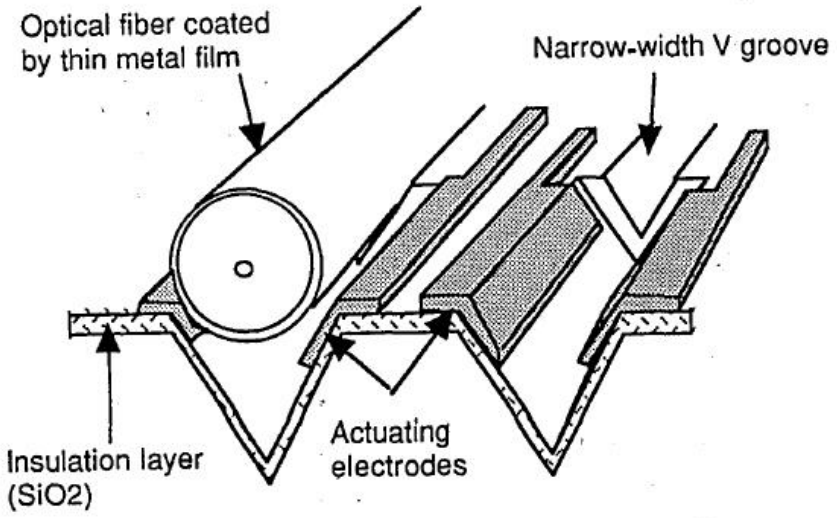

Figure **1.10**: Optical fiber alignment with electrostatic force

Most active alignment, however, is performed in-package via ferrule and precision assembly with elaborate and time consuming adhesive protocols, as shown in figure **1.11** [**47**,**56**]. At present, precision active alignment methods are very expensive and bulky. Furthermore, misalignment can occur in package handling and use in the field. Additionally, long term mechanical stress relaxation and thermal creep can cause a time dependent loss of coupling efficiency. Such stress relaxation in the solders and epoxies used to attach aligned fibers and devices is a common source of premature failure in optoelectronic packages [**57**].

Since the McDonnell Douglas Corporation patented their optical fiber alignment assembly in 1996, a number of alignment mechanisms have been suggested. The PZT-based active alignment system is one of these [**58**]. Recently, research on this subject reveals a PZT deposited SiO_2 actuator that is glued to an LTCC substrate as an optical

fiber alignment system. [**59**] However, the cantilever structure has only one degree of freedom. In addition, a continuous electric field for actuator, or resin for ferrule, is essential for maintaining an aligned position.

A solution that possesses limited power usage and the possibility of re-alignment is the major goal. In this thesis, an alignment system was envisioned with a compact size, low price, and the unique functionality of re-adjusting fiber position when misalignment occurs. All subsequent chapters are focused on the tasks necessary toward this goal.

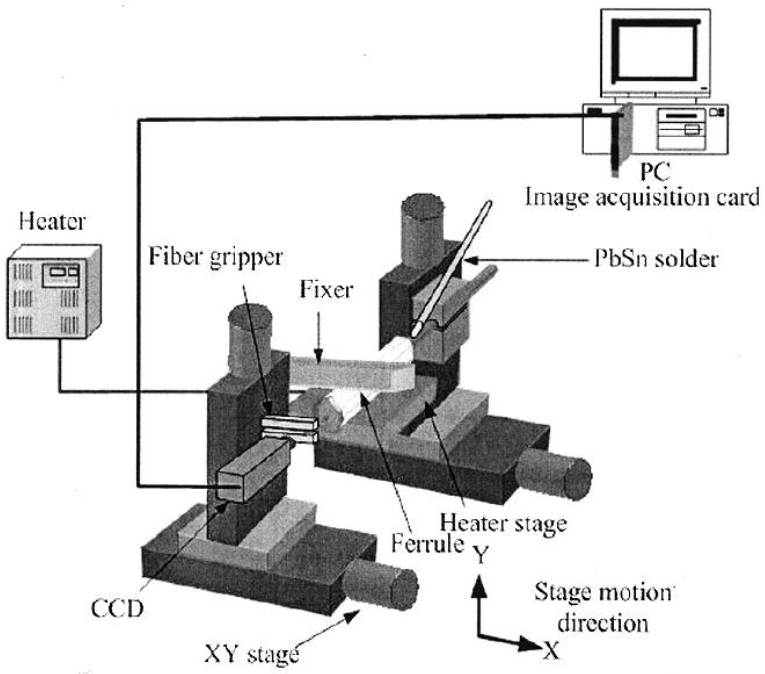

Figure **1.11**: Conventional fiber-solder-ferrule package equipment

Chapter 2

OBJECTIVES AND THESIS OUTLINE

In this research, an approach is to be developed and proven to be effective for active optical fiber alignment by combining a piezoelectric ultrasonic motor with a low-temperature, cofired ceramic (LTCC) system. The main goals of this research were to develop an ultrasonic motor with two degrees of freedom and to integrate the motor into an optical fiber alignment package. To achieve these goals, compositional and thermal process development was required such that a hard piezoelectric ceramic could be cofired with Ag inner electrodes. These powders are to be tape-cast and then cofired, with minimal interactions with LTCC materials. Cofiring conditions had to be determined to allow the possibility of integration in LTCC and piezoelectrics. In addition, design and control of the alignment package were also essential parts of the demonstration. Consequently, the thesis consists of four major parts, and the details and relevance are outlined below.

(1) Materials development

A low-temperature, sinterable, high-power piezoelectric material with a composition that allows cofiring with an LTCC substrate was needed to integrate the ultrasonic motor into a ceramic package. Due to the unavoidable deterioration of piezoelectric properties in low-temperature sintering, the material work will start by developing a suitable, high-performance, base piezoelectric composition. At the same

time, this new high-power composition should have good potential for redefining it into a low-temperature sintering ceramic. Based on this specially-designed piezoelectric ceramic material, low-temperature sintering will be achieved by doping with oxide additives that have low melting points.

The target properties for the specially-designed material for use in low-temperature sinterable ultrasonic applications are:

(1) Maximum vibration velocity (rectangular plate) $\upsilon_{max} > 0.4$ m/sec

(2) Low voltage $Q_m > 500$

(3) Low voltage $d_{33} > 250$ pC/N

(4) Low voltage $k_p > 0.4$

(5) $T_c > 250\ ^oC$

(2) Device design

For optical fiber alignment package applications, a compact ultrasonic motor with two degrees of freedom is needed. The required motor will be obtained by modification of an earlier developed L-shaped motor. Width and angle change effects on motor performance will be analyzed using ATILA finite element method (FEM). A bimorph structure could provide two degrees of freedom, and a thick-film process allows the creation of small, thin motors. Fundamental motions of the motor will be assessed with prototype motors.

(3) Fabrication processes

An LTCC fabrication process would provide compact and thin ultrasonic motors, and a cofiring technique will lower the manufacturing costs. The cofiring process is consists of two steps: 1) cofiring piezoelectric motor with Ag electrode and 2) cofiring with LTCC system. The issues that accompany the cofiring process, such as delamination, camber and inter-diffusion will be dealt with through a combination of mechanical, thermal and structural approaches.

(4) Optical fiber alignment

The optical fiber alignment system will give two-degrees of freedom to an inserted optical fiber, and the aligned position will be sustained without using resins or an external electric field, owing to the newly-designed motor and package. Therefore, misalignment due to mechanical shock, temperature changes, or aging effects could be corrected with the proposed alignment system. For the manipulation of the fiber, a driving circuit that can control four motor inputs independently will be prepared.

Finally, the combination of LTCC technologies and the piezoelectric ultrasonic motors could offer a unique opportunity for the development of advanced electronic and opto-electronic packaging techniques and applications.

Chapter 3

EXPERIMENTAL PROCEDURE

3.1 Materials Development

The specimens studied in this research were fabricated according to the formula: $0.8Pb(Zr_dTi_{1-d})O_3$ - $0.2Pb[(1-c)\{(1-b)\ (Zn_{0.8}\ Ni_{0.2})_{1/3}\ (Nb_{1-a}Sb_a)_{2/3} - b\ (Li_{1/4}\ (Nb_{1-a}Sb_a)_{3/4})\} - c\ (Mn_{1/3}(Nb_{1-a}Sb_a)_{2/3})]O_3$ + x wt% CuO, where a=0~0.3; b=0~0.4; c=0~0.4; d=0.46~0.5; x=0~1.5, respectively. Raw materials of PbO, ZrO_2, TiO_2, ZnO, NiO, Nb_2O_5, Sb_2O_5, Li_2CO_3, MnO_2, and CuO with >99% purity were used to prepare samples by a conventional ceramic sintering process. The obtained mixture was ball-milled using zirconia ball media (diameter 2 mm ~ 10 mm) in a polyethylene jar for 24 h with ethanol. The mixed slurry was dried and calcined at 750 ^oC for 2h. The calcined powders were ball-milled again with additives and consolidated into disks of 12.5 mm diameter and rectangular plates using cold isostatic pressing (CIP) at 30,000 psi. PbO-rich atmosphere sintering of the ceramics was performed in a high-purity alumina crucible at the temperature of 900 ^oC for 2h. The sintered rectangular samples were cut into dimensions 42 x 7 x 1 mm^3 in order to measure vibration velocity in the 31 mode, k_{31} and corresponding Q_m for this k_{31}. The crystal structure and symmetry of the sintered bodies were examined by X-ray diffraction (XRD) and sintered densities were measured by the Archimedes method. Electrode (Dupont, QS 171) was printed on the lapped surfaces for electrode. The electroded specimens were poled in silicone oil at 150^oC by applying a d.c.

field of 3 kV/mm for 30 min. The electromechanical properties were measured using Institute of Acoustics Academida Sinica piezo d_{33} meter (ZJ-2) and Agilent precision impedance analyzer (4294A) based on IEEE standards [**60**]. Dielectric properties as a function of temperature were obtained by measuring the capacitance and loss using Stanford Research Systems LCR meter (SR715) in an automated temperature controlled furnace interfaced with a computer for data acquisition. The observation and analysis of the vibration velocity were performed using HP function/arbitrary waveform generator (33120A), NF Electronic Instruments High Speed Amplifier (4025), HP oscilloscope (54645A), Polytec Vibrometer (OFV 3001) and Polytec Fiber Interfero meter (OFV 511). Under the center portion (nodal line) support, the vibration velocity at the edge was measured, with simultaneous temperature monitoring at the nodal line by an infrared camera.

3.2 2-degrees of Freedom Motor Design

2-degrees of freedom motor was designed by the ATILA (ATILA 5.4.2 Micromechatronics Inc., PA, U.S.A.) finite element method (FEM) software. Prototypes, to verify the 2-dimensional motions of the motor, were prepared from lead zirconate titanate (PZT) based thick films (NCC-NA01, Nihon Ceratec Co., Ltd., Japan). Its properties are shown in the Table **3.1**, and these values were employed in the ATILA. A schematic flow chart of the experimental procedure is shown in figure **3.1**.

Table **3.1**: Material properties of the NA composition (Nihon Ceratec Co., Ltd.)

Property	Value	Unit
Density	7650	kg/m^3
s^E_{11}	12.7×10^{-12}	m^2/N
s^E_{12}	-3.95×10^{-12}	m^2/N
s^E_{13}	-3.35×10^{-12}	m^2/N
s^E_{33}	15.7×10^{-12}	m^2/N
s^E_{44}	36.5×10^{-12}	m^2/N
d_{15}	470×10^{-12}	C/N
d_{31}	-145×10^{-12}	C/N
d_{33}	310×10^{-12}	C/N
$\varepsilon^T_{11}/\varepsilon_0$	1800	
$\varepsilon^T_{33}/\varepsilon_0$	1700	
Q_m	2000	

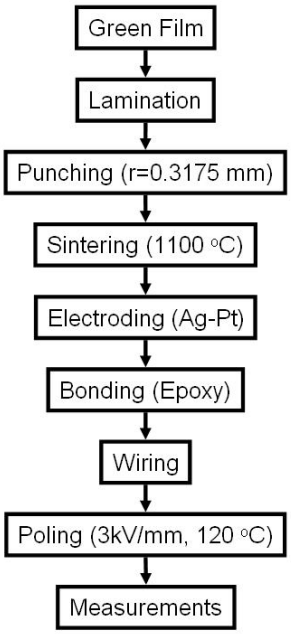

Figure **3.1**: Experimental procedure flow chart of the motor fabrication

Considering a sintering shrinkage, PZT green films were laminated to the thickness of 0.4 mm and were punched into desired shapes which were guided by the simulations. A shrinkage factor was applied to the motor design to account for material densification during firing. After binder removal the motors were sintered at 1100 ^{o}C for 2h. Ag-Pt paste (Dupont QS171) was printed on the motors and post-fired at 850 ^{o}C for 15 min. dwell time at peak temperature. A poling process was performed in a silicone oil bath at 120 ºC under 3 kV/mm for 30 minutes in the thickness direction. To fabricate the bimorph structure motors, two motors were attached together with epoxy (Emerson & Cuming STYCAST 1266). After soldering copper wires to the electrodes, the motor was installed on the motor holder using a cyanoacrylate instant adhesive (Loctite® Quicktite®). 2-dimensional displacement at the motor tip was measured by laser interferometers (OFV 511, Polytec). Speed of revolution, torque and efficiency were measured and calculated by the experimental set-up as shown in figure **3.2**. The spring length was adjusted to apply a desired load conditions. Transient speed and speed of revolution were measured by an optical sensor which detected slits attached to a bearing. From these measurements torque and efficiency of the motor was determined.

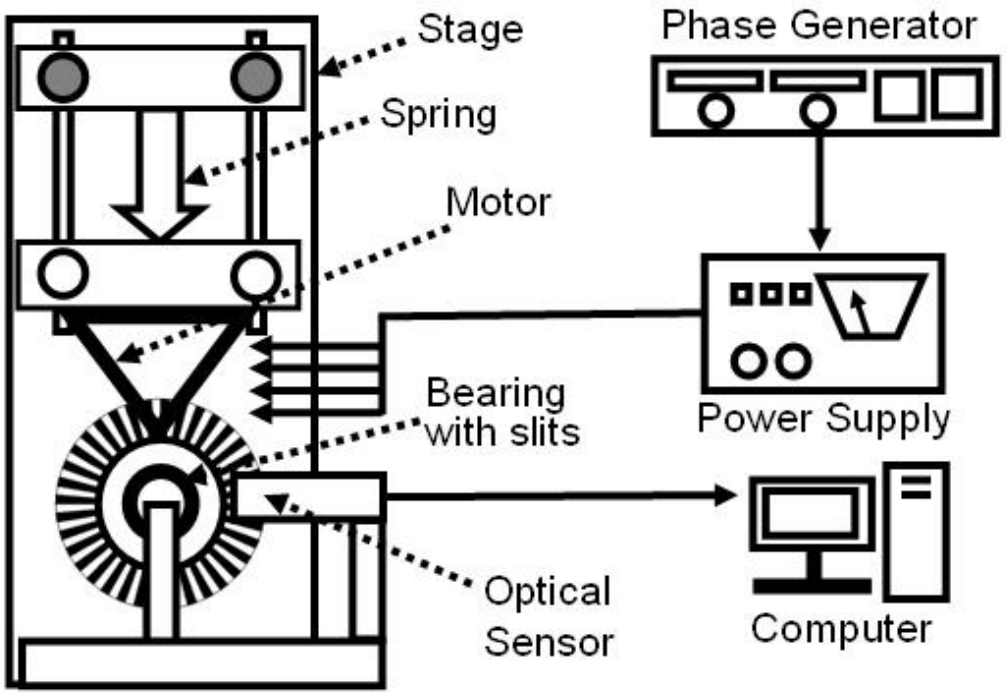

Figure **3.2**: The experimental set-up for characterizing the performance of the motor

3.3 Fabrication Processes

For the cofiring process, material that was specially designed was used, and motor size was also changed from the proof-of-concept prototype in the motor design stage. Therefore, the new material properties of the developed ceramic were employed in finite element method (FEM) simulations for the motor (ATILA). The design of the motor was again optimized for better performance to obtain two-degrees of freedom of motion. LTCC techniques were used for the motor fabrication processes, as shown in figure **3.3**. Thick films were manufactured using tape caster (A. J. Carsten Co., Inc. Laboratory Bench Caster Standard Model) from powders prepared with conventional ceramic processing. The films laminated (Pacific Trinetics Corporation IL-4004 Isostatic Lamination System) to obtain desired thickness and then punched into specific shape (UHT Crop MP-4150 Punch Machine) guided by the AutoCAD.

Fundamental motor motion and properties of the cofired motor were measured using an optical decoder with a bearing. Commercialized LTCC tapes (DuPont 951) and the developed low-temperature, sinterable, piezoelectric materials were used to investigate the feasibility of cofiring an ultrasonic motor within an LTCC substrate, together with silver electrodes. Sintering temperature, ramping up, and holding time were varied to determine the optimal cofiring conditions to successfully fabricate a cofired optical fiber alignment package.

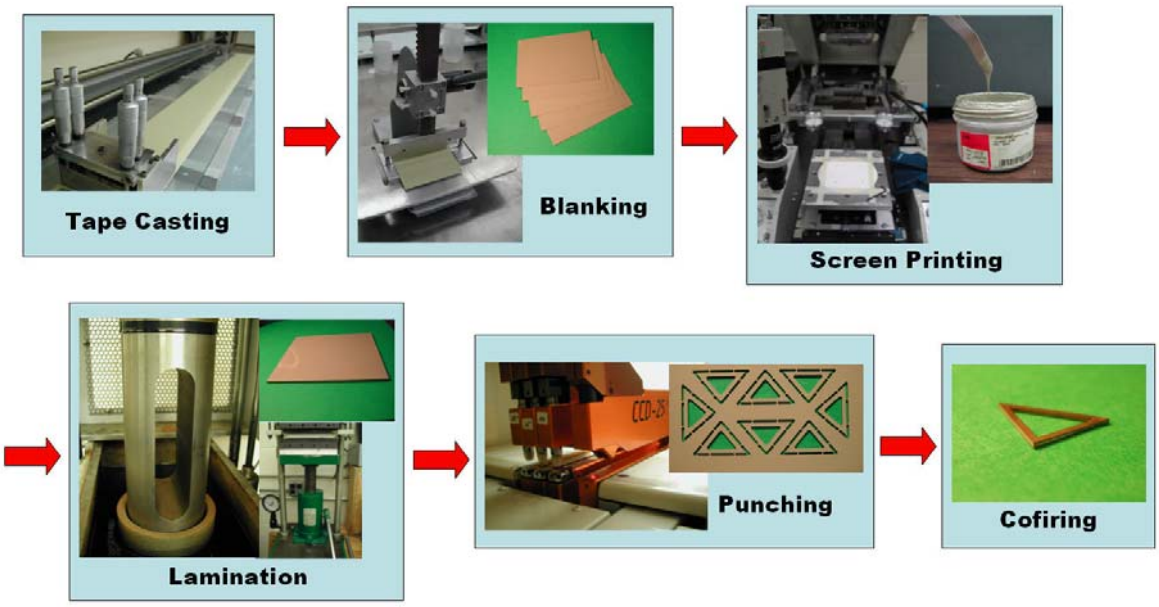

Figure **3.3**: Low temperature cofired ceramic (LTCC) process.

3.4 Optical Fiber Alignment

For a practical alignment test, a package that can effectively transfer the two-dimensional motions of the motor to the slider was designed using AutoCAD. After cofiring all the parts of the motor, springs and an optical fiber were secured to the platform structure and the slider, respectively. For alignment control, a driving circuit was prepared that can generate two phases and allocate them to the four input electrodes of the motor. This circuit was also connected to a computer in order to control easily the direction of movement of the slider. Optical fiber alignment tests were conducted using various optical fibers and a He-Ne laser with a wavelength of 635 nm. The results of the laser-to-fiber alignment were obtained from a laser power meter. After alignment was performed, as a reliability test, ambient temperature was changed from room temperature up to 60 ^{o}C. Aligned laser intensity was measured during the temperature change.

Chapter 4

MATERIALS DEVELOPMENT

4.1 Chapter Overview

This chapter presents information about the development of materials with high-power characteristics and the low-temperature sintering of modified $PbZrO_3$-$PbTiO_3$-$Pb(Zn,Ni)_{1/3}Nb_{2/3}O_3$ ternary system. To integrate a piezoelectric material into a cofirable device in an LTCC package, a material which can be sintered at 850 ^oC to 900 ^oC with silver or copper electrodes. The materials have need of electro-mechanical properties that can be used in high drive conditions or intermediate drive conditions. Particularly both a high-electric field and a high-vibration level operation circumstances are associated with significant heat generation. With such diverse requirements, hard and soft characteristics compromised piezoelectric ceramics, which are called high power piezoelectric materials, were studied in this thesis with low temperature sintering conditions.

There are many binary and ternary piezoelectric compositions with perovskite structure. Especially, those from a PZT-relaxor ternary system near MPB region have been intensively studied to obtain high piezoelectric properties [**61**]. In addition, for the case of the $Pb(Ni_{1/3}Nb_{2/3})O_3$ relaxor, it can enhance the sintering kinetics, which lowers the firing temperature even without flux [**9**].

For the practical ultrasonic motor application with high voltage/power drive condition, the vibration velocity was measured as a function of applied electric field (rms

value). The addition of small amounts of CuO resulted in high vibration velocities of over 0.6 m/s, but high electric fields were required. As the amount of CuO added was increased, high vibration velocity was obtained with lower electric fields, owing to enhanced electro-mechanical properties. When more than 0.5 wt% was added, the maximum vibration was observed at approximately 0.48 m/s.

.

4.2 High Power Piezoelectric Composition

The first purpose of this study is to enhance the piezoelectric properties of the $PbZrO_3$-$PbTiO_3$-$Pb(Zn,Ni)_{1/3}Nb_{2/3}O_3$ system to provide improved high-power piezoelectric ceramics; attractive base compositions for low temperature sintering. We investigated the effect of Sb, Li and Mn substitution, because Sb_2O_5 and PbO provide a eutectic point with a melting point of around 820 ^oC [**62**]. This low melting temperature can help densification of the ceramics via the liquid phase formation. Furthermore, $Pb(Mn_{1/3}Sb_{2/3})$ solid solution with PZT is well known high power material [**14**]. Li_2CO_3 is known as one of the sintering aids at low temperature because of its low melting point (723 ^oC) [**63**]. Low density of the Li_2CO_3 (2.11 g/cm^3) would accompany larger number of particles compare to heavy elements, such as Bi_2O_3, therefore a concentration of Li_2CO_3 can be homogeneous mixed in overall particulate system. In addition, $Pb(Li_{1/4}Nb_{3/4})$ included Pb(Mg,Nb)-Pb(Zr,Ti)+MnO_2 ceramics demonstrated significant characteristic improvement such as k_p=0.54 and Q_m=2132, when they were milled for a long period (100h) [**64**]. Regarding the Mn doping effect, because Mn ions can have

various valencies from Mn^{4+} to Mn^{2+}, and Mn^{4+} occupying the B-sites of perovskite structure can be reduced to Mn^{2+}, consequently Mn^{3+} (acceptor in the B sites) can ameliorate the elastic loss of the piezo-ceramic, i.e., an increase in the Q_m value [**65**].

Figure **4.1** shows a ternary phase diagram of the high power piezoelectric ceramic system studied in this chapter. The complex B-site perovskites are often relaxor ferroelectric materials. These compounds also have a MPB and piezoelectric properties can increase at the boundary [**9**]. Furthermore, some relaxor-PZT systems can be sintered at low temperature (~ 900 ^oC) even before addition of flux materials [**66**]. Based on a complex B-site lead perovskite of $Pb((Zn_{0.8}Ni_{0.2})_{1/3}Nb_{2/3})O_3$, various cations, such as Sb, Li and Mn, were substituted into B_1 and B_2 sites for properties enhancement. After substitutions into the complex B-sites perovskite structure, a Zr/Ti ratio was varied to obtain desired properties.

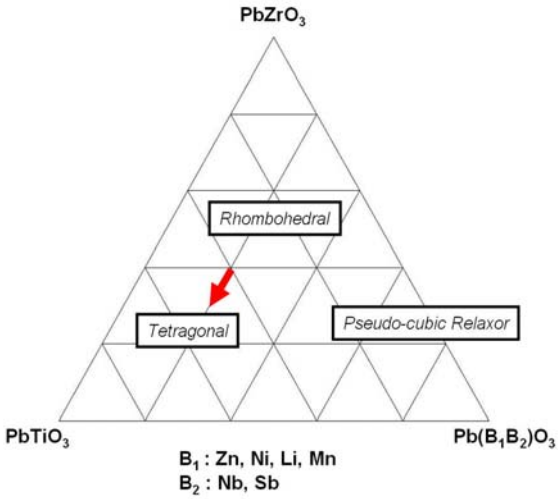

Figure **4.1**: A ternary diagram of developed system

4.2.1 Sb Substitution

Figure **4.2** shows the X-ray diffraction (XRD) patterns for the samples sintered at 1200 ^{o}C in $0.8Pb(Zr_{0.5}Ti_{0.5})O_3$-$0.2Pb(Zn_{0.8}Ni_{0.2})_{1/3}(Nb_{1-a}Sb_a)_{2/3}O_3$ (a=0~0.3) ceramics. It can be seen that all samples exhibit a perovskite structure with no secondary phase detected in the XRD analysis. The base composition (a=0) lies near the morphotropic phase boundary (MPB) with a slight tetragonal symmetry since both the (1 0 0) and (2 0 0) peaks show splitting consistent with the different lattice parameters of a≠c. The substitution of Sb shifts the composition and reduces the tetragonality, because of a successive decrease in the (200) peak splitting, as shown in figures **4.2** (b) ~ **4.2** (d).

SEM surface images of the $0.8Pb(Zr_{0.5}Ti_{0.5})O_3$-$0.2Pb(Zn_{0.8}Ni_{0.2})_{1/3}(Nb_{1-a}Sb_a)_{2/3}O_3$ (a=0~0.3) ceramics sintered at 1200^{o}C 2h are shown in figure **4.3**. The SEM images of the sintered body did not exhibit any evidence of a second phase, consistent with the XRD results. The average grain size, determined by linear intercept method, was 1.8 ㎛ at the composition of a=0, but the number of small grain was decreased and the average grain size increased to around 2.5 ㎛, when Sb substitution is increased.

Density, dielectric permittivity ($\varepsilon^{T}_{3}/\varepsilon_0$), electromechanical coupling factor (k_p), mechanical quality factor and piezoelectric constant (d_{33}) are plotted as a function of the Sb substitution in figure **4.4** in the $0.8Pb(Zr_{0.5}Ti_{0.5})O_3$-$0.2Pb(Zn_{0.8}Ni_{0.2})_{1/3}(Nb_{1-a}Sb_a)_{2/3}O_3$ composition, sintered at 1200^{o}C for 2h. The density was slightly increased with substitution of Sb and this might be because of grain growth which was shown in the SEM images. The properties at a=0.1 in $0.8Pb(Zr_{0.5}Ti_{0.5})$-$0.2Pb(Zn_{0.8}Ni_{0.2})_{1/3}(Nb_{1-a}Sb_a)_{2/3}O_3$ ceramics are summarized: d_{33}=458 pC/N, k_p=0.60, $\varepsilon^{T}_{3}/\varepsilon_0$=1822 and Q_m=70 at

planar mode. The soft piezoelectric characteristics were slightly increased then decreased as the amount of Sb substitution increased. The tendency of the properties k_p, $\varepsilon^T_3/\varepsilon_0$ and d_{33} were similar to that of density. Thus, Sb substitution helped solid state sintering of the ceramics and significantly improved piezoelectric properties at a=0.1. Further substitution of antimony, however, reduced the tetragonality of the ceramics which is shown in figure **4.2**.

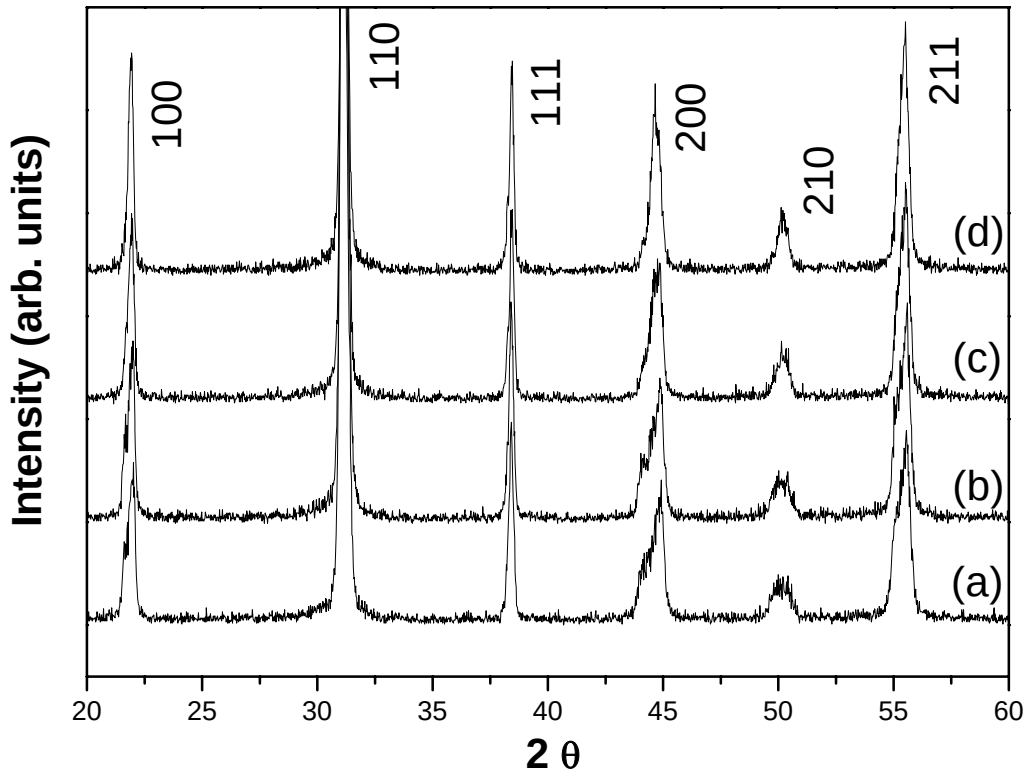

Figure **4.2**: XRD patterns of samples sintered at 1200°C for 2h in $0.8Pb(Zr_{0.5}Ti_{0.5})O_3$-$0.2Pb(Zn_{0.8}Ni_{0.2})_{1/3}(Nb_{1-a}Sb_a)_{2/3}O_3$ ceramics: (a) a=0, (b) a=0.1, (c) a=0.2 and (d) a=0.3

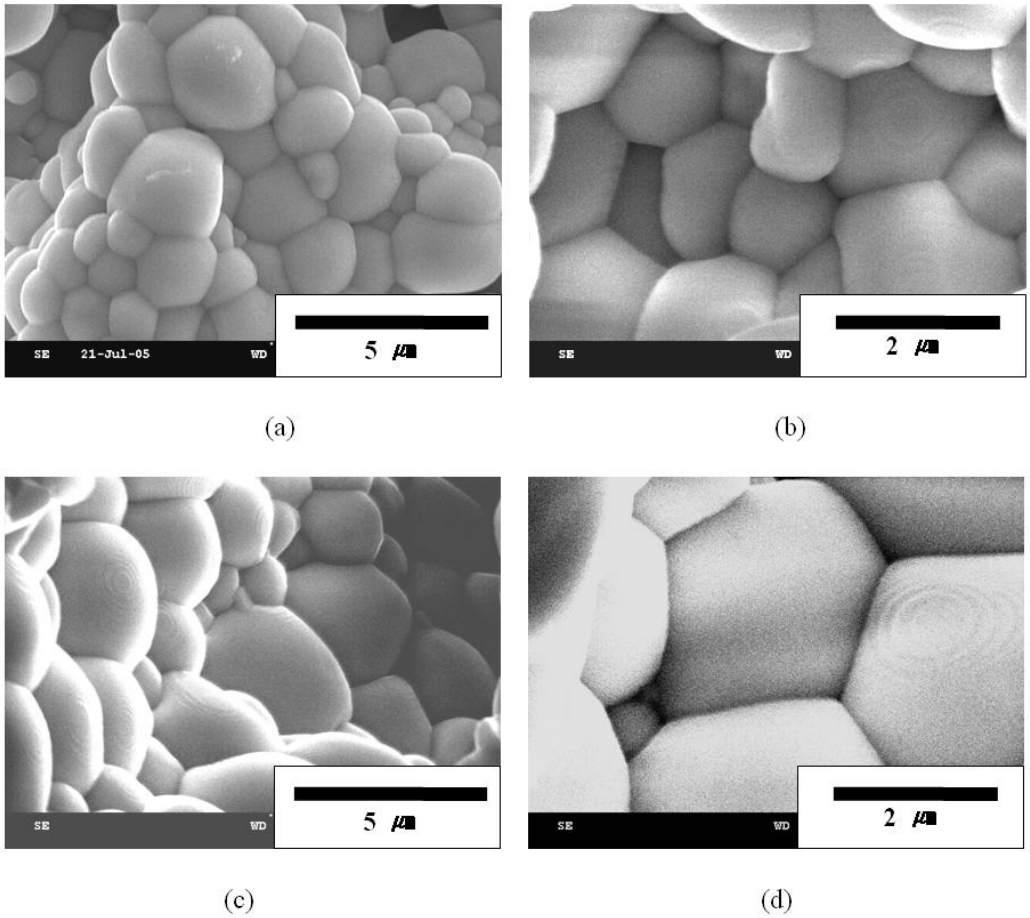

Figure **4.3**: SEM images of specimens sintered at 1200°C for 2h in $0.8Pb(Zr_{0.5}Ti_{0.5})O_3$-$0.2Pb(Zn_{0.8}Ni_{0.2})_{1/3}(Nb_{1-a}Sb_a)_{2/3}O_3$ ceramics: (a) a=0, (b) a=0.1, (c) a=0.2 and (d) a=0.3.

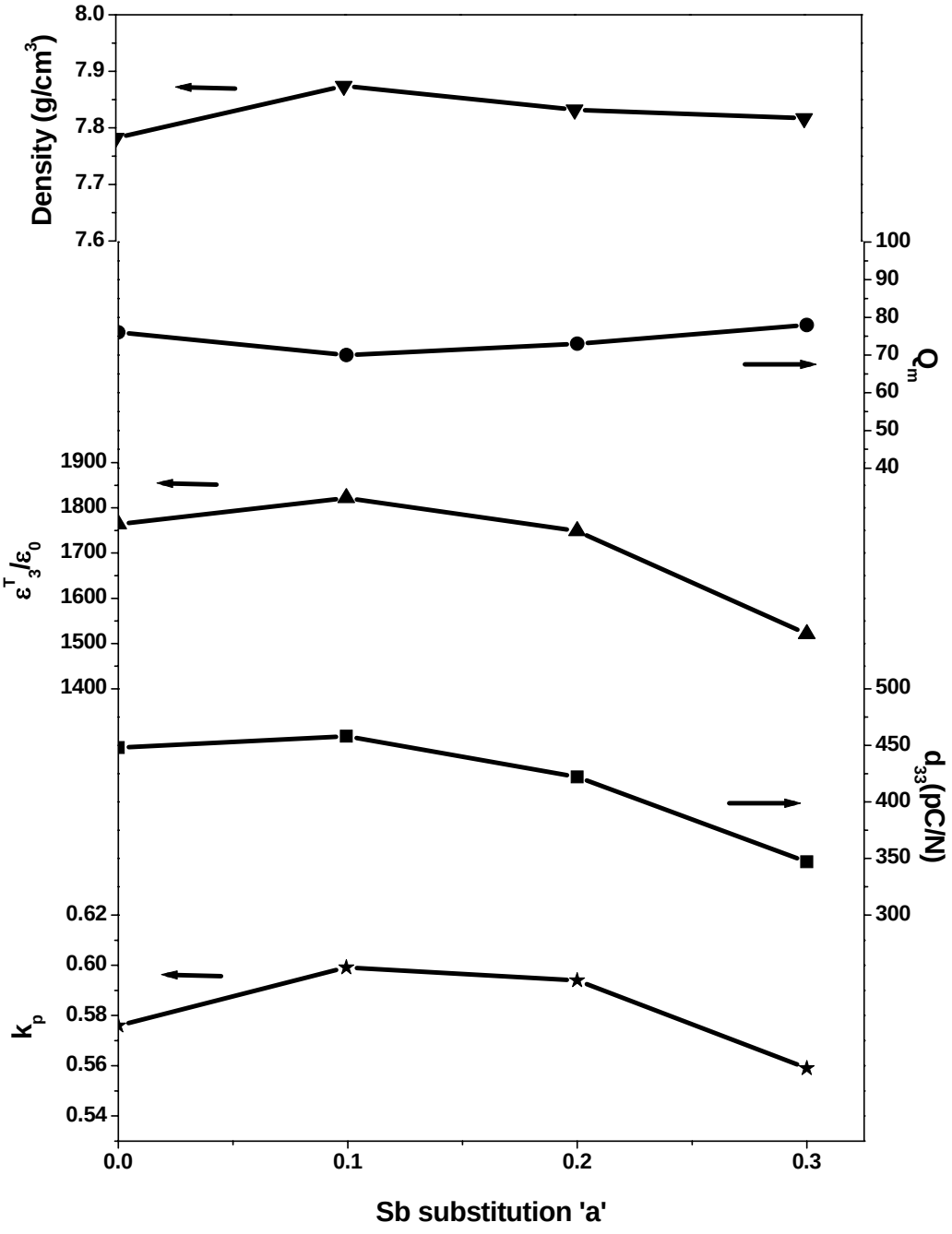

Figure **4.4**:Density, dielectric permittivity ($\varepsilon^{T}_{3}/\varepsilon_0$), electromechanical coupling factor (k_p), mechanical quality factor (Q_m) and piezoelectric constant (d_{33}) of specimens sintered at 1200^{o}C for 2h in $0.8Pb(Zr_{0.5}Ti_{0.5})O_3$-$0.2Pb(Zn_{0.8}Ni_{0.2})_{1/3}(Nb_{1-a}Sb_a)_{2/3}O_3$ ceramics.

4.2.2 Li Substitution

Figure **4.5** shows the XRD patterns of the $0.8Pb(Zr_{0.5}\ Ti_{0.5})O_3$ - $0.2Pb[\ (1\text{-}b)\ (Zn_{0.8}Ni_{0.2})_{1/3}\ (Nb_{0.9}Sb_{0.1})_{2/3} - b\ Li_{1/4}(Nb_{0.9}Sb_{0.1})_{3/4}]O_3$ (b=0~0.4) ceramics. With the Li substitution, the (1 0 0) and (2 0 0) peak splits didn't change much with keeping the (1 1 1) peak sharp; that means the structure of ceramics was maintained as tetragonal phase. Also, no secondary phase was detected in the XRD analysis with Li-addition.

The microstructure variation upon substitution of Li is shown in figure **4.6**. The average grain size did not show significant differences with the Li substitution. However, the densities increased with a small amount of Li, as shown in figure **4.7**, which enhanced also the dielectric permittivity $\varepsilon^T_3/\varepsilon_0$, electromechanical coupling factor k_p and piezoelectric constant d_{33} of Li substituted ceramics. The composition $0.8Pb(Zr_{0.5}Ti_{0.5})O_3$-$0.2Pb[(1\text{-}b)\ (Zn_{0.8}Ni_{0.2})_{1/3}(Nb_{0.9}Sb_{0.1})_{2/3} - b\ Li_{1/4}(Nb_{0.9}Sb_{0.1})_{3/4}]O_3$ (b=0.3) exhibited k_p=0.66, d_{33}=548, $\varepsilon^T_3/\varepsilon_0$=2468 and Q_m=59 at planar mode. The increase of soft piezoelectric characteristics may be due to two reasons: one is the role of Li as a sintering aid that can be assumed from the increase of density, and the other is Nb and Sb amount increase with Li substitution. Due to the ratio between Li and $Nb_{0.9}Sb_{0.1}$ is 1:3, whereas the ratio $Zn_{0.8}Ni_{0.2}$ to $Nb_{0.9}Sb_{0.1}$ is 1:2. Consequently, with the increase of $Li_{1/4}(Nb_{0.9}Sb_{0.1})$ substitution, Nb and Sb amount also increase. This additional Nb and Sb can act as donors. Therefore, k_p, d_{33} and $\varepsilon^T_3/\varepsilon_0$ could increase even though low valence Li was substituted for Zn and Ni.

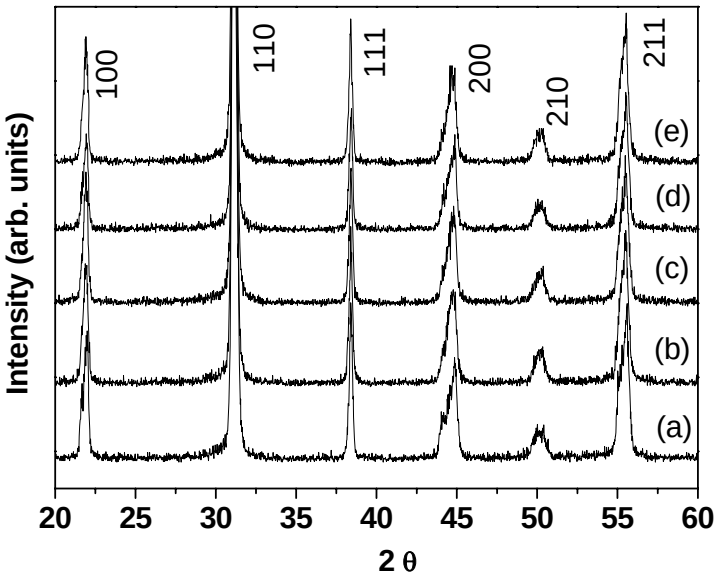

Figure **4.5**:XRD patterns of specimens in $0.8Pb(Zr_{0.5}\,Ti_{0.5})O_3$ - $0.2Pb[\,(1\text{-}b)\,(Zn_{0.8}Ni_{0.2})_{1/3}\,(Nb_{0.9}Sb_{0.1})_{2/3} - b\;Li_{1/4}(Nb_{0.9}Sb_{0.1})_{3/4}]O_3$ ceramics: (a) b=0, (b) b=0.1, (c) b=0.2, (d) b=0.3 and (e) b=0.4 sintered at 1200^oC for 2h.

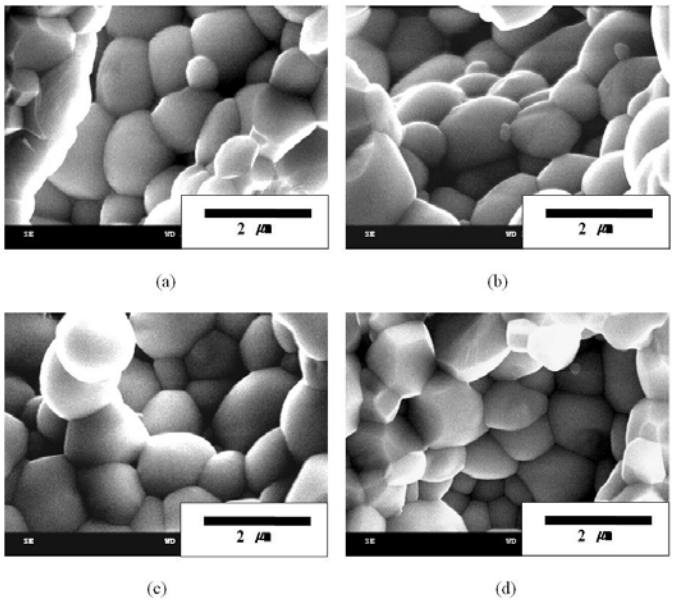

Figure **4.6**:SEM images of specimens in $0.8Pb(Zr_{0.5}\,Ti_{0.5})O_3$ - $0.2Pb[\,(1\text{-}b)\,(Zn_{0.8}Ni_{0.2})_{1/3}(Nb_{0.9}Sb_{0.1})_{2/3} - b\,Li_{1/4}(Nb_{0.9}Sb_{0.1})_{3/4}]O_3$ ceramics: (a) b=0.1, (b) b=0.2, (c) b=0.3 and (d) b=0.4 sintered at 1200^{o}C for 2h.

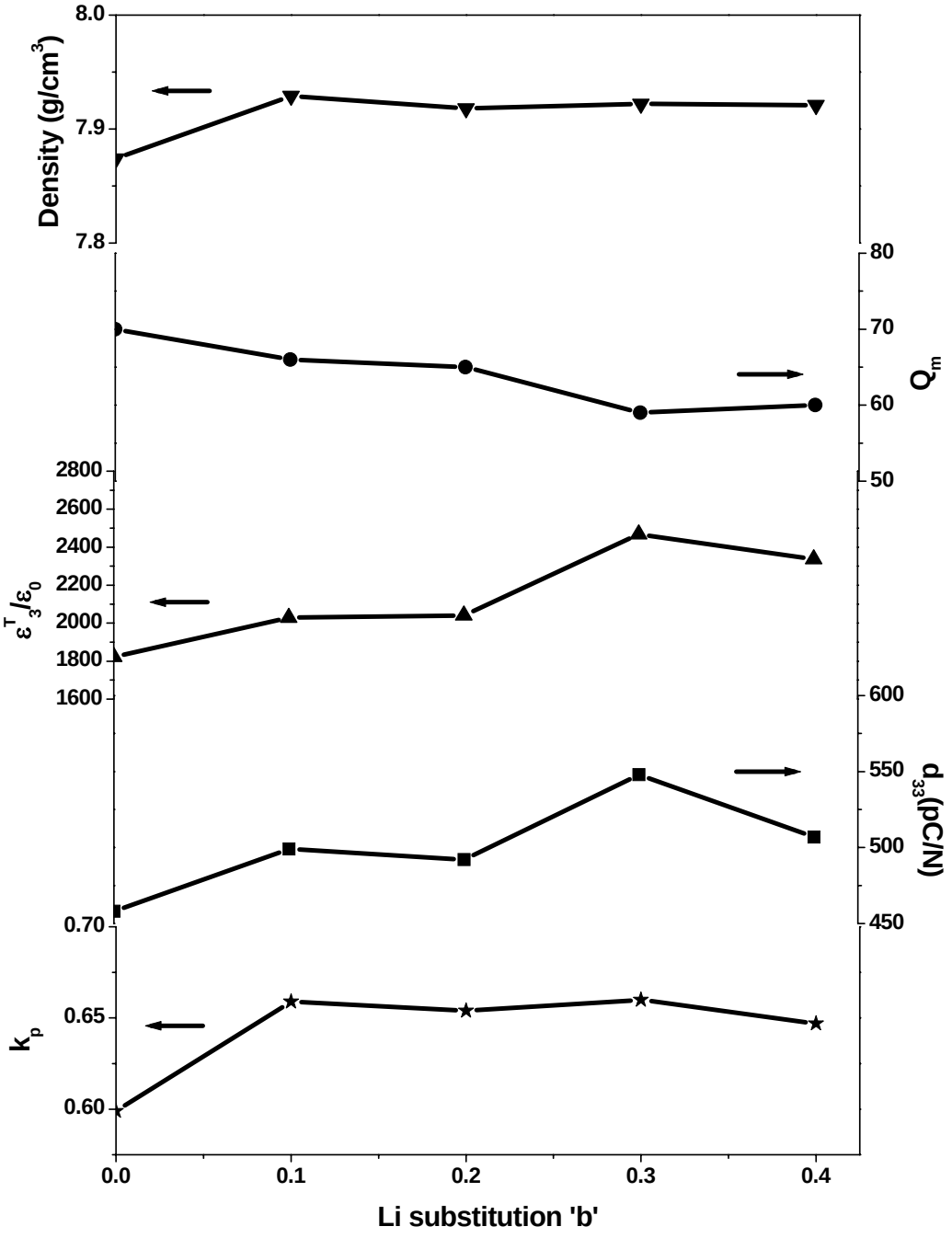

Figure **4.7**: Density, dielectric permittivity ($\varepsilon^{T}_{3}/\varepsilon_0$), electromechanical coupling factor (k_p), mechanical quality factor (Q_m) and piezoelectric constant (d_{33}) of specimens sintered at 1200°C for 2h in $0.8Pb(Zr_{0.5}\ Ti_{0.5})O_3$ - $0.2Pb[\ (1\text{-}b)\ (Zn_{0.8}Ni_{0.2})_{1/3}\ (Nb_{0.9}Sb_{0.1})_{2/3} - b\ Li_{1/4}(Nb_{0.9}Sb_{0.1})_{3/4}]O_3$ ceramics: (a) b=0, (b) b=0.1, (c) b=0.2, (d) b=0.3 and (e) b=0.4.

4.2.3 Mn Substitution

Manganese is a well-known additive for enhancing electrical resistivity, but through direct substitution in the form of perovskite compounds, such as $Pb(Mn_{1/3}Nb_{2/3})O_3$ and $Pb(Mn_{1/3}Sb_{2/3})O_3$, these compounds can act as a relaxor modification to PZT ceramics which would have a softening effect [**67**,**68**]. In either case, depending on the influence to the total system, it could be expected to harden or soften the piezoelectric response. In this study, Mn was substituted on $0.8Pb(Zr_{0.5}Ti_{0.5})O_3$-$0.2Pb[0.7(Zn_{0.8}Ni_{0.2})_{1/3}\ (Nb_{0.9}Sb_{0.1})_{2/3} - 0.3Li_{1/4}(Nb_{0.9}Sb_{0.1})_{3/4}]O_3$ ceramics. Figure **4.8** shows the XRD patterns of the samples sintered at 1200°C for 2h in $0.8Pb(Zr_{0.5}Ti_{0.5})O_3$ - $0.2Pb[(1\text{-}c)\ \{0.7\ (Zn_{0.8}Ni_{0.2})_{1/3}(Nb_{0.9}Sb_{0.1})_{2/3} - 0.3Li_{1/4}(Nb_{0.9}Sb_{0.1})_{3/4}\} - c\ Mn_{1/3}(Nb_{0.9}Sb_{0.1})_{2/3}]O_3$ (c=0~0.4) ceramics. According to these X-ray power diffraction patterns, $Mn_{1/3}(Nb_{0.9}Sb_{0.1})_{2/3}$ substitution increase reduced tetragonality, like the Sb substitution case. The microstructure of $0.8\ Pb(Zr_{0.5}\ Ti_{0.5})O_3$ - $0.2\ Pb[\ (1\text{-}c)\ \{0.7\ (Zn_{0.8}Ni_{0.2})_{1/3}\ (Nb_{0.9}Sb_{0.1})_{2/3} - 0.3Li_{1/4}(Nb_{0.9}Sb_{0.1})_{3/4}\} - c\ Mn_{1/3}\ (Nb_{0.9}Sb_{0.1})_{2/3}\ ]O_3$ (c=0~0.4) ceramics in figure **4.9** exhibits almost the same average grain size without second phase.

Figure **4.10** shows the density, dielectric and piezoelectric properties of the $0.8Pb(Zr_{0.5}\ Ti_{0.5})O_3$ - $0.2Pb[\ (1\text{-}c)\ \{0.7(Zn_{0.8}Ni_{0.2})_{1/3}(Nb_{0.9}Sb_{0.1})_{2/3} - 0.3Li_{1/4}(Nb_{0.9}Sb_{0.1})_{3/4}\} - c\ Mn_{1/3}\ (Nb_{0.9}Sb_{0.1})_{2/3}\ ]O_3$ (c=0~0.4) ceramics. According to the formula, Mn was substituted for Zn, Ni and Li which have the same or lower valence than manganese, so hardening effect could be predicted. The optimum characteristics for high power applications were obtained for the composition of $0.8Pb(Zr_{0.5}Ti_{0.5})O_3$ - $0.2Pb[(1\text{-}c)\ \{0.7$

$(Zn_{0.8}Ni_{0.2})_{1/3}$ $(Nb_{0.9}Sb_{0.1})_{2/3}$ – 0.3 $Li_{1/4}(Nb_{0.9}Sb_{0.1})_{3/4}\}$ – c $Mn_{1/3}$ $(Nb_{0.9}Sb_{0.1})_{2/3}]O_3$ when c=0.3. This composition yielded the coefficients k_p=0.56, Q_m=1951 (planar mode), d_{33}=239pC/N and $\varepsilon^T_3/\varepsilon_0$=739.

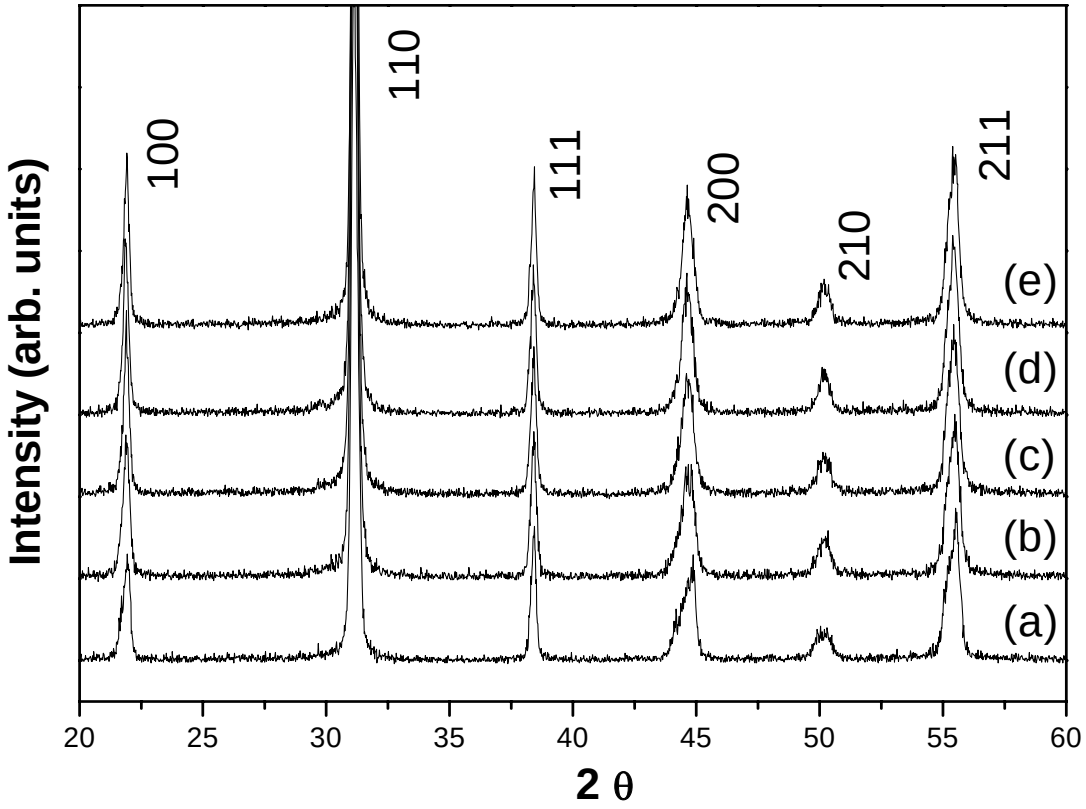

Figure **4.8**: XRD patterns of specimens sintered at 1200°C for 2h in $0.8Pb(Zr_{0.5}Ti_{0.5})O_3$ - $0.2Pb[(1-c)\{0.7(Zn_{0.8}Ni_{0.2})_{1/3}(Nb_{0.9}Sb_{0.1})_{2/3}–0.3Li_{1/4}(Nb_{0.9}Sb_{0.1})_{3/4}\} – c\ Mn_{1/3}(Nb_{0.9}Sb_{0.1})_{2/3}]O_3$ ceramics: (a) c=0, (b) c=0.1, (c) c=0.2, (d) c=0.3 and (e) c=0.4.

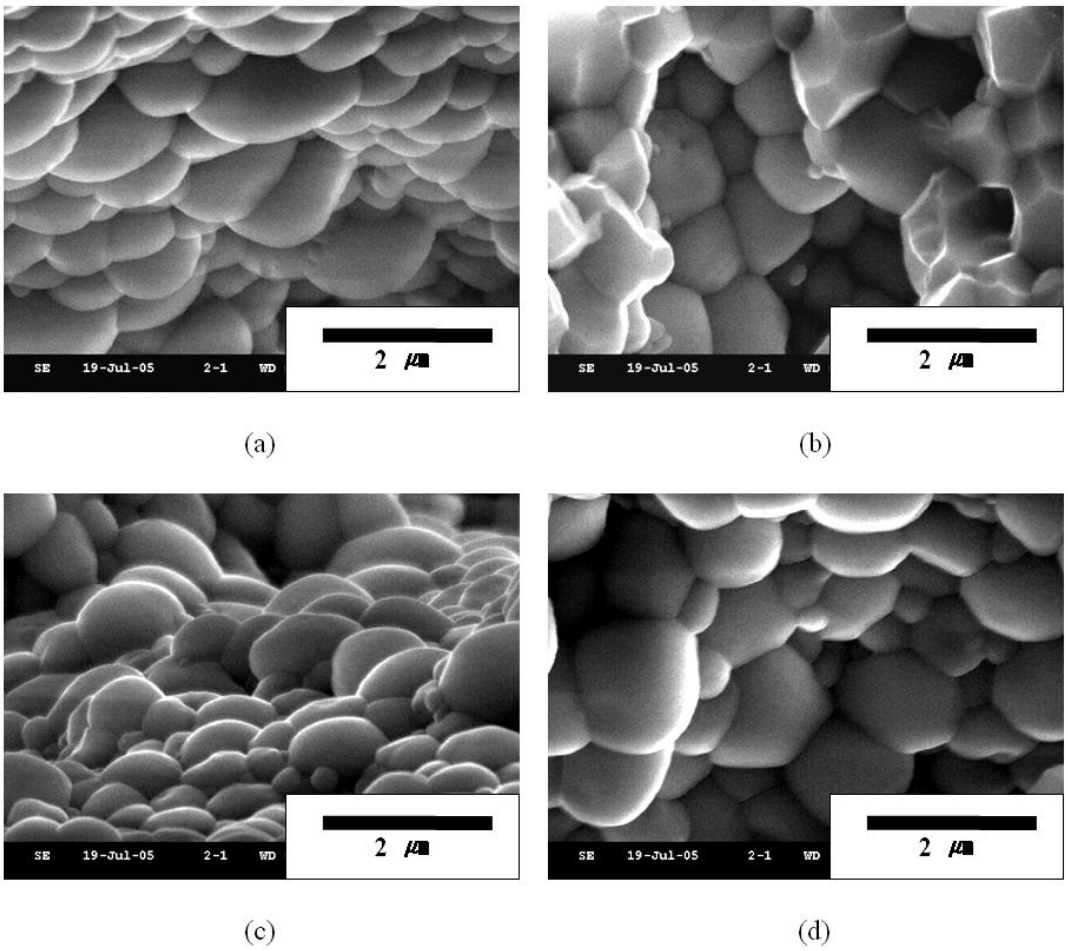

Figure **4.9**: SEM images of specimens sintered at 1200°C for 2h in $0.8Pb(Zr_{0.5}\,Ti_{0.5})O_3$ - $0.2Pb[\ (1\text{-}c)\ \{0.7(Zn_{0.8}Ni_{0.2})_{1/3}\ (Nb_{0.9}Sb_{0.1})_{2/3}\text{–}0.3Li_{1/4}(Nb_{0.9}Sb_{0.1})_{3/4}\}\ -\ c\ Mn_{1/3}\ (Nb_{0.9}Sb_{0.1})_{2/3}\ ]O_3$ ceramics: (a) c=0.1, (b) c=0.2, (c) c=0.3 and (d) c=0.4.

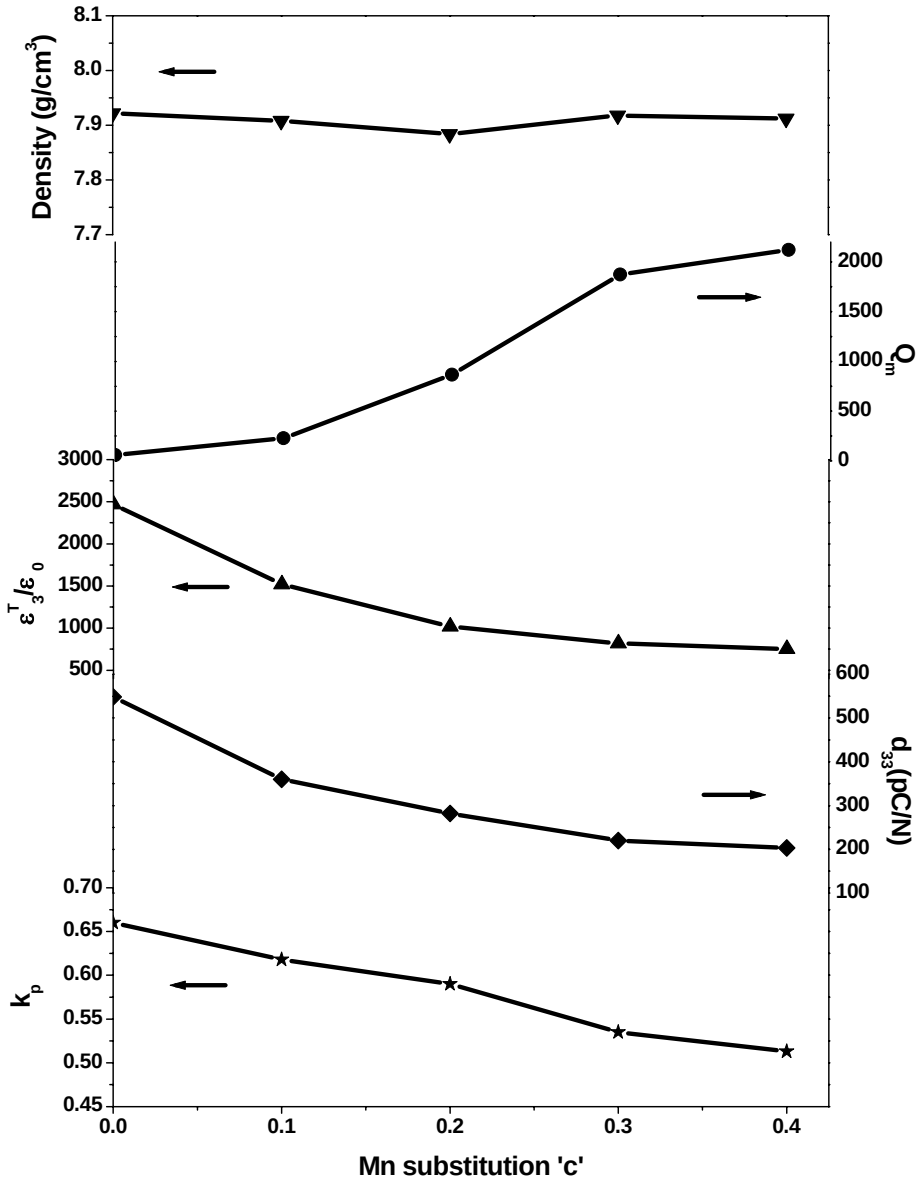

Figure **4.10**: Density, dielectric permittivity ($\varepsilon^{T}_{3}/\varepsilon_0$), electromechanical coupling factor (k_p), mechanical quality factor (Q_m) and piezoelectric constant (d_{33}) of specimens sintered at 1200°C for 2h in $0.8Pb(Zr_{0.5}\ Ti_{0.5})O_3$ - $0.2Pb[\ (1\text{-}c)\ \{0.7(Zn_{0.8}Ni_{0.2})_{1/3}\ (Nb_{0.9}Sb_{0.1})_{2/3}-0.3Li_{1/4}(Nb_{0.9}Sb_{0.1})_{3/4}\} - c\ Mn_{1/3}\ (Nb_{0.9}Sb_{0.1})_{2/3}\ ]O_3$ ceramics.

4.2.4 Zr/Ti Ratio Adjustment

The d_{33} value of a complex formula of $0.8Pb(Zr_{0.5}Ti_{0.5})O_3$ - $0.2Pb[\ (1\text{-}c)\ \{0.7(Zn_{0.8}Ni_{0.2})_{1/3}(Nb_{0.9}Sb_{0.1})_{2/3}\text{–}0.3Li_{1/4}(Nb_{0.9}Sb_{0.1})_{3/4}\}\ -\ c\ Mn_{1/3}\ (Nb_{0.9}Sb_{0.1})_{2/3}\ ]O_3$ ceramics (c=0.3) may suffer from a relative bending of the MPB. To optimize the d_{33}, a reformulation of the Zr/Ti ratio was made to obtain enhanced properties. Figure **4.11** shows the XRD patterns of the $0.8Pb(Zr_dTi_{1-d})O_3$ - $0.2Pb[\ 0.7\ \{0.7(Zn_{0.8}Ni_{0.2})_{1/3}(Nb_{0.9}Sb_{0.1})_{2/3}\text{–}0.3Li_{1/4}(Nb_{0.9}Sb_{0.1})_{3/4}\}\ -\ 0.3\ Mn_{1/3}\ (Nb_{0.9}Sb_{0.1})_{2/3}\ ]O_3$ ceramics (d=0.46~0.5) sintered at 1200°C for 2h. A split of peak the (h 0 0) was small when d=0.5, however, as the Zr concentration is decreased, the split became significant on (1 0 0), (2 0 0), (2 1 0) and (2 1 1) peaks, suggesting the crystal symmetry change from the MPB across to the tetragonal.

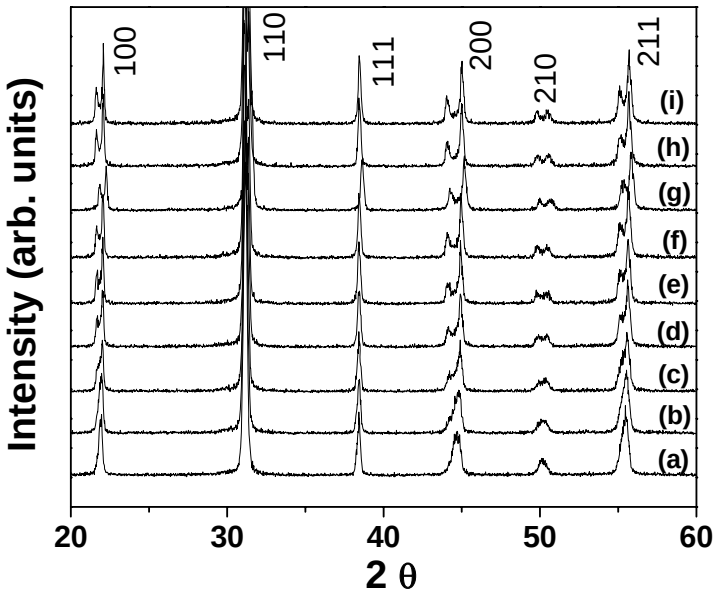

Figure **4.11**: XRD patterns of specimens sintered at 1200°C for 2h in $0.8Pb(Zr_d\,Ti_{1-d})O_3$ - $0.2Pb[\ 0.7\{0.7(Zn_{0.8}Ni_{0.2})_{1/3}\ (Nb_{0.9}Sb_{0.1})_{2/3}\text{–}0.3Li_{1/4}(Nb_{0.9}Sb_{0.1})_{3/4}\}\ -\ 0.3Mn_{1/3}\ (Nb_{0.9}Sb_{0.1})_{2/3}\ ]O_3$ ceramics: (a) d=0.5, (b) d=0.495, (c) d=0.49, (d) d=0.485 (e) d=0.48, (f) d=0.475, (g) d=0.47 (h) d=0.465 and (i) d=0.46.

The density, dielectric and piezoelectric properties of $0.8Pb(Zr_dTi_{1-d})O_3$ - $0.2Pb[\ 0.7\ \{0.7(Zn_{0.8}Ni_{0.2})_{1/3}(Nb_{0.9}Sb_{0.1})_{2/3}–0.3Li_{1/4}(Nb_{0.9}Sb_{0.1})_{3/4}\}\ –\ 0.3\ Mn_{1/3}\ (Nb_{0.9}Sb_{0.1})_{2/3}\ ]O_3$ ceramics (d=0.46~0.5) sintered at 1200°C for 2h are shown in figure **4.12**. The values k_p, d_{33} and dielectric constant increased until the Zr amount decreased to d=0.48. Over this quantity, the soft characteristics decreased again, and Q_m showed a minimum when k_p, d_{33} maximum are obtained. The optimum properties of k_p=0.573, Q_m=1502 (planar mode), d_{33}=330pC/N, and $\varepsilon^T_3/\varepsilon_0$=1653 were obtained for the $0.8Pb(Zr_d\ Ti_{1-d})O_3$ - $0.2Pb[0.7\{0.7(Zn_{0.8}Ni_{0.2})_{1/3}\ (Nb_{0.9}Sb_{0.1})_{2/3} – 0.3Li_{1/4}\ (Nb_{0.9}Sb_{0.1})_{3/4}\} – 0.3Mn_{1/3}\ (Nb_{0.9}\ Sb_{0.1})_{2/3}\ ]O_3$ ceramics (d=0.48). In addition, k_{31} and Q_m in this mode were measured with rectangular samples of d=0.48 and d=0.5. For d=0.5, k_{31}=0.3 and Q_m=1815 and k_{31}=0.33 and Q_m=1404 when d=0.48. The Q_m in 31-mode showed a smaller value than that of planar mode and the relation between the k_p and k_{31} can be given as Eq. 4:

$$k_p = k_{31}\sqrt{2/(1-\sigma)} \qquad \text{Eq.}\mathbf{4}$$

where σ is the Poisson's ratio [**1**]. Thus, σ for d=0.5 and 0.48 can be obtained as 0.43 and 0.34, respectively.

Figure **4.13** plots temperature dependence of the dielectric permittivity in two samples, d = 0.48 and 0.5 of the $0.8Pb(Zr_dTi_{1-d})O_3$ - $0.2Pb[\ 0.7\ \{0.7\ (Zn_{0.8}Ni_{0.2})_{1/3}\ (Nb_{0.9}Sb_{0.1})_{2/3}–0.3Li_{1/4}(Nb_{0.9}Sb_{0.1})_{3/4}\} – 0.3\ Mn_{1/3}\ (Nb_{0.9}Sb_{0.1})_{2/3}\ ]O_3$ ceramics. When Zr/Ti ratio was changed from 0.5/0.5 to 0.48/0.52 the Curie temperature increased from 285.6 °C to 289.58 °C. Furthermore, a slight hump around 160 °C in the composition with d=0.50 at the exact MPB composition, which may be originated from the rhombohedral

to tetragonal phase transition, disappeared for the composition d=0.48, suggesting the pure tetragonal phase and more stable temperature dependence of for this composition.

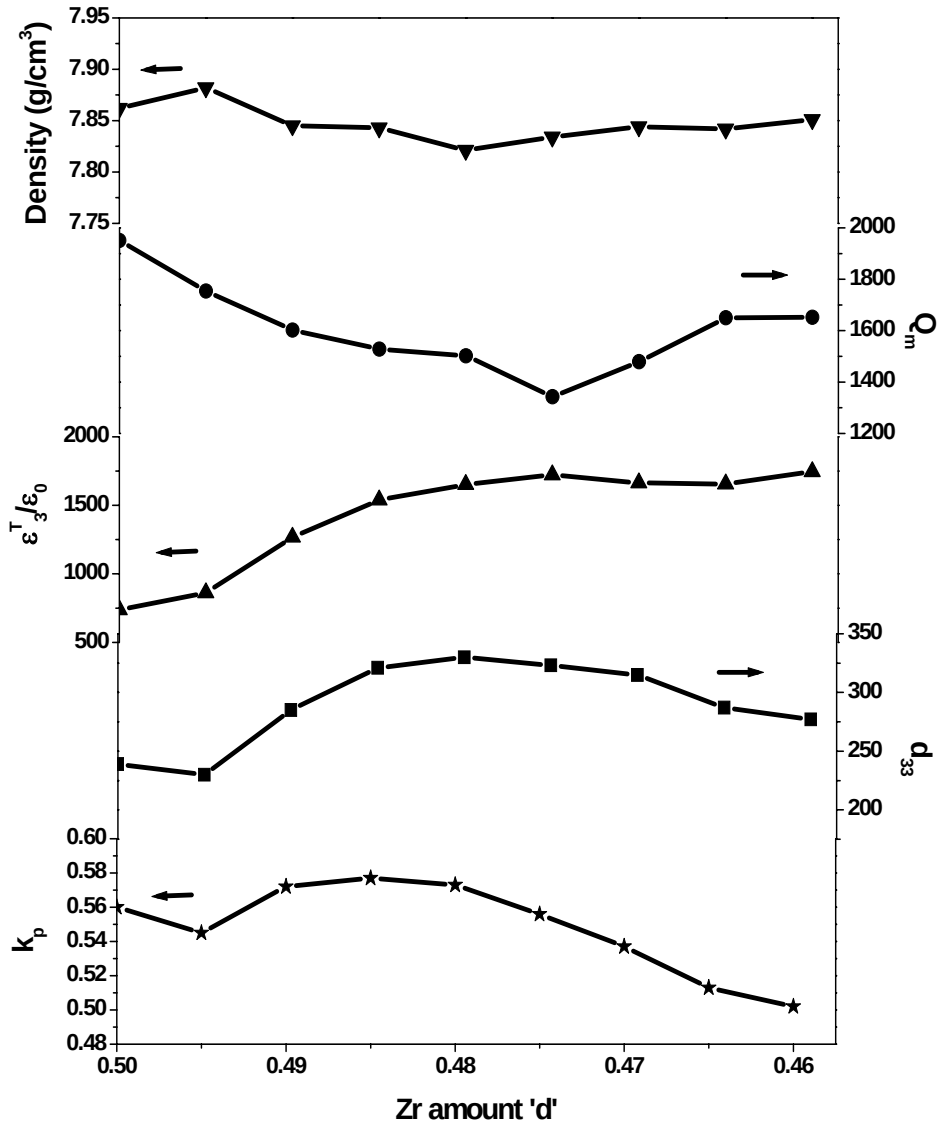

Figure **4.12**: Density, dielectric permittivity ($\varepsilon^T_3/\varepsilon_0$), electromechanical coupling factor (k_p), mechanical quality factor (Q_m) and piezoelectric constant (d_{33}) of specimens sintered at 1200°C for 2h in $0.8Pb(Zr_x\ Ti_{1-x})O_3$ - $0.2Pb[0.7\{0.7(Zn_{0.8}Ni_{0.2})_{1/3}\ (Nb_{0.9}Sb_{0.1})_{2/3}$– $0.3Li_{1/4}(Nb_{0.9}Sb_{0.1})_{3/4}\}$ – $0.3Mn_{1/3}\,(Nb_{0.9}Sb_{0.1})_{2/3}\ ]O_3$ ceramics (d=0.46 ~ 0.5).

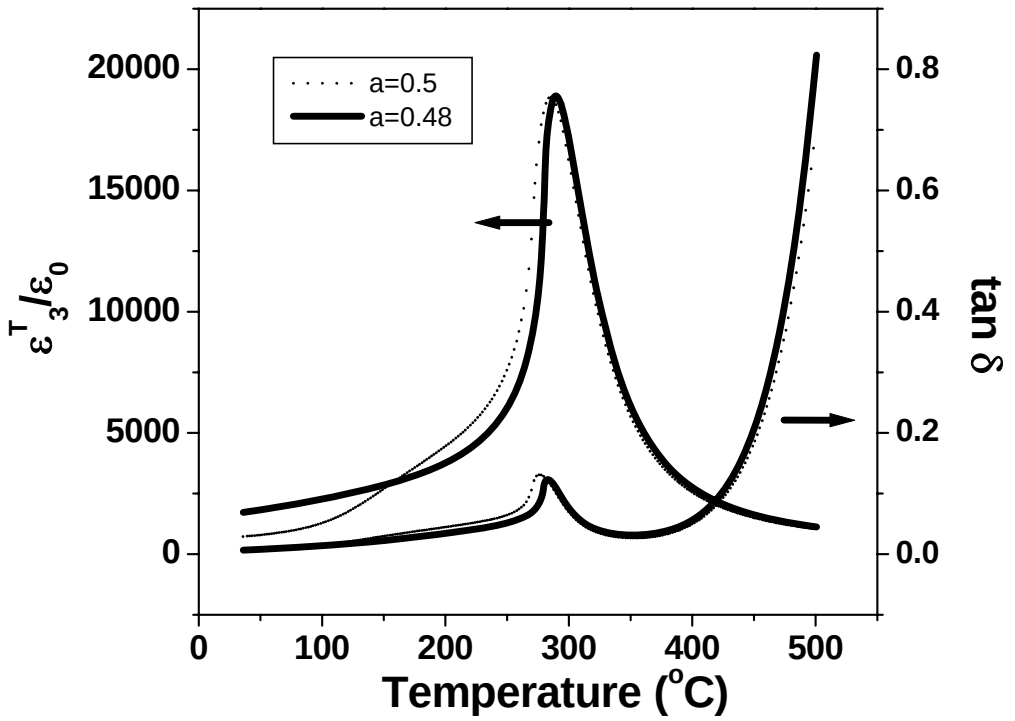

Figure **4.13**: Dielectric permittivity ($\varepsilon^T_3/\varepsilon_0$) temperature dependence of the specimens sintered at 1200°C for 2 h can be seen for two compositions $0.8Pb(Zr_dTi_{1-d})O_3$ - $0.2Pb[0.7\{0.7(Zn_{0.8}Ni_{0.2})_{1/3}(Nb_{0.9}Sb_{0.1})_{2/3}–0.3Li_{1/4}(Nb_{0.9}Sb_{0.1})_{3/4}\} – 0.3Mn_{1/3}(Nb_{0.9}Sb_{0.1})_{2/3}]O_3$ ceramics (d=0.48, 0.5) at 1 kHz.

In order to verify the usefulness under high voltage/power drive condition, the vibration velocity was measured for the $0.8Pb(Zr_dTi_{1-d})O_3$ - $0.2Pb[\ 0.7\ \{0.7(Zn_{0.8}Ni_{0.2})_{1/3}(Nb_{0.9}Sb_{0.1})_{2/3}–0.3Li_{1/4}(Nb_{0.9}Sb_{0.1})_{3/4}\} – 0.3\ Mn_{1/3}\ (Nb_{0.9}Sb_{0.1})_{2/3}\ ]O_3$ ceramics (d=0.48, 0.5) as a function of applied electric field (rms value). The k_{31} fundamental mode was used for this measurement (sample size: 42mm x 7mm x 1mm), and the measurement was conducted until the temperature at the sample center portion (i.e., the nodal line) reached up to 20°C from room temperature. In figure **4.14**, both d=0.5 and d=0.48

specimens which showed rather high maximum vibration velocity, 0.6 m/s and 0.58 m/s, respectively. The right hand side and points corresponds to 20 ^{o}C temperature rise from room temperature.

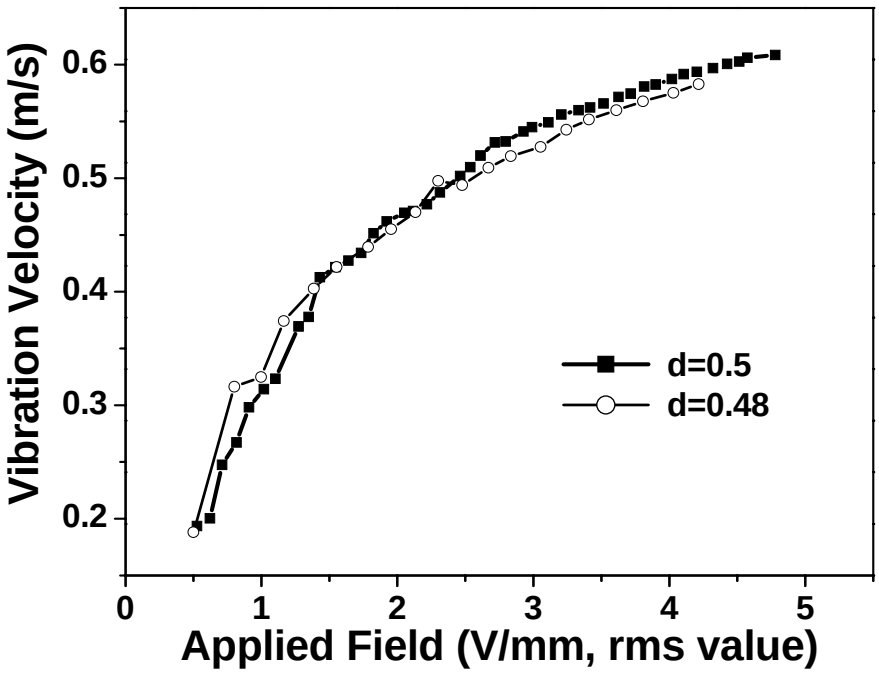

Figure **4.14**: Vibration velocity variation of the $0.8Pb(Zr_xTi_{1-x})O_3$ - $0.2Pb$ [0.7 {0.7 $(Zn_{0.8}Ni_{0.2})_{1/3}$ $(Nb_{0.9}Sb_{0.1})_{2/3}$ – $0.3Li_{1/4}(Nb_{0.9}Sb_{0.1})_{3/4}$} – $0.3Mn_{1/3}(Nb_{0.9}Sb_{0.1})_{2/3}$]$O_3$ ceramics (d=0.48 and d=0.5).

4.3 Low Temperature Sintering

Based on successful development of the high power composition at high temperature, the next step of the research was to lower the sintering temperature. Initially, the effect of the addition of CuO on the sinterability, crystal structure, piezoelectric and dielectric properties was investigated in $0.8Pb(Zr_{0.48}Ti_{0.52})O_3$ - $0.2Pb[\ 0.7\ \{0.7(Zn_{0.8}Ni_{0.2})_{1/3}\ (Nb_{0.9}Sb_{0.1})_{2/3}–0.3Li_{1/4}(Nb_{0.9}Sb_{0.1})_{3/4}\}\ –\ 0.3\ Mn_{1/3}\ (Nb_{0.9}Sb_{0.1})_{2/3}\ ]O_3$ ceramics. The sintering temperature of all the specimens was fixed at 900 ^oC which is cofiring compatible temperature with Ag electrode and low temperature cofired ceramics (LTCC) substrate.

Figure **4.15** shows the XRD patterns of the samples sintered at 900oC for 2h in $0.8Pb(Zr_{0.48}Ti_{0.52})O_3$ - $0.2Pb[\ 0.7\ \{0.7(Zn_{0.8}Ni_{0.2})_{1/3}\ (Nb_{0.9}Sb_{0.1})_{2/3}–0.3Li_{1/4}(Nb_{0.9}Sb_{0.1})_{3/4}\}$ $–\ 0.3\ Mn_{1/3}\ (Nb_{0.9}Sb_{0.1})_{2/3}\ ]O_3$ + x wt% CuO ceramics. It can be seen in figure **4.15** that all samples exhibit a perovskite structure, and that there is no secondary phase until x=0.2(no peak for secondary phase was detected in the range of 0.0-0.2). When x was over 0.3, a secondary phase peak was observed, however, a structure for the second peaks were not clearly identified. For over 0.2 wt% CuO addition, (100) and (200) peaks start to split, with keeping (111) in a single peak, which is consistent with an “increased” tetragonality.

Figure **4.16** shows the SEM images of the $0.8Pb(Zr_{0.48}Ti_{0.52})O_3$ - $0.2Pb[\ 0.7\ \{0.7(Zn_{0.8}Ni_{0.2})_{1/3}\ (Nb_{0.9}Sb_{0.1})_{2/3}–0.3Li_{1/4}(Nb_{0.9}Sb_{0.1})_{3/4}\}\ –\ 0.3\ Mn_{1/3}\ (Nb_{0.9}Sb_{0.1})_{2/3}\ ]O_3$ + x wt% CuO ceramics sintered at 900 ^oC for 2h. No secondary phases are observed in XRD

results or in the SEM images. The size of 2 μm and 0.2 μm grains coexisted when x=0.1 As the percentage of CuO addition increases, grain growth is enhanced. This grain growth with CuO addition can be explained with liquid phase sintering. Previously it was shown that the addition of CuO can reduce the sintering temperature of the $Pb(Zr,Ti)O_3$-$Pb(Ni,Nb)O_3$ system by the formation of a liquid phase [**69**]. Thus, we infer that a similar liquid phase formation can also present for the $0.8Pb(Zr_{0.48}Ti_{0.52})O_3$ - $0.2Pb[\ 0.7\ \{0.7(Zn_{0.8}Ni_{0.2})_{1/3}\ (Nb_{0.9}Sb_{0.1})_{2/3}–0.3Li_{1/4}(Nb_{0.9}Sb_{0.1})_{3/4}\} – 0.3\ Mn_{1/3}\ (Nb_{0.9}Sb_{0.1})_{2/3}\ ]O_3$ + x wt% CuO ceramics.

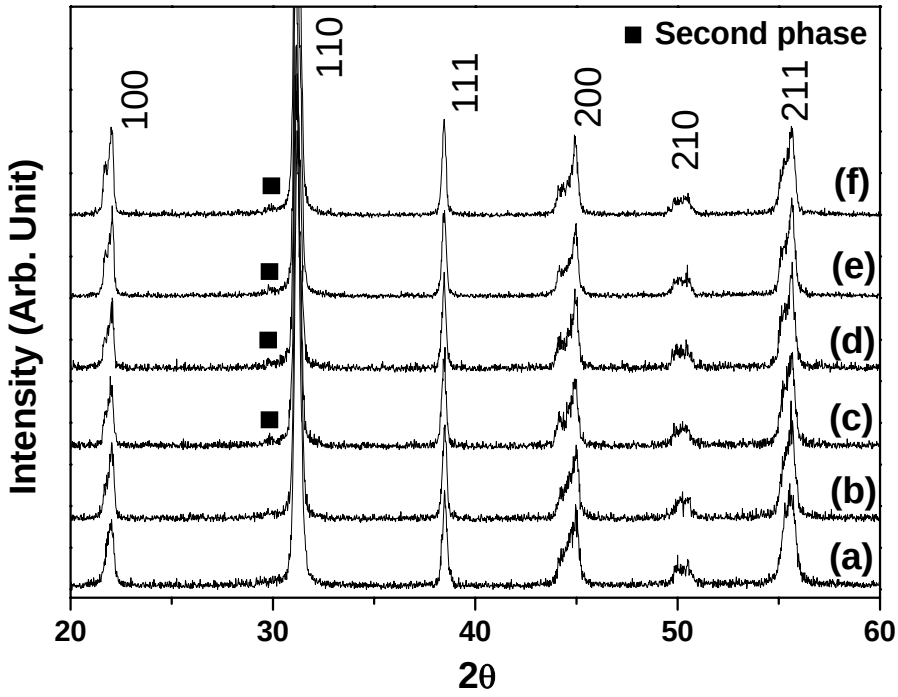

Figure **4.15**: XRD patterns of the samples sintered at 900°C for 2h in $0.8Pb(Zr_{0.48}Ti_{0.52})O_3$ - $0.2Pb[\ 0.7\ \{0.7(Zn_{0.8}Ni_{0.2})_{1/3}\ (Nb_{0.9}Sb_{0.1})_{2/3}–0.3Li_{1/4}(Nb_{0.9}Sb_{0.1})_{3/4}\} – 0.3\ Mn_{1/3}\ (Nb_{0.9}Sb_{0.1})_{2/3}\ ]O_3$ + x wt% CuO ceramics.: (a) x=0.1, (b) x=0.2, (c) x=0.3 (d) x=0.4 (e) x=0.5 and (f) x=0.6

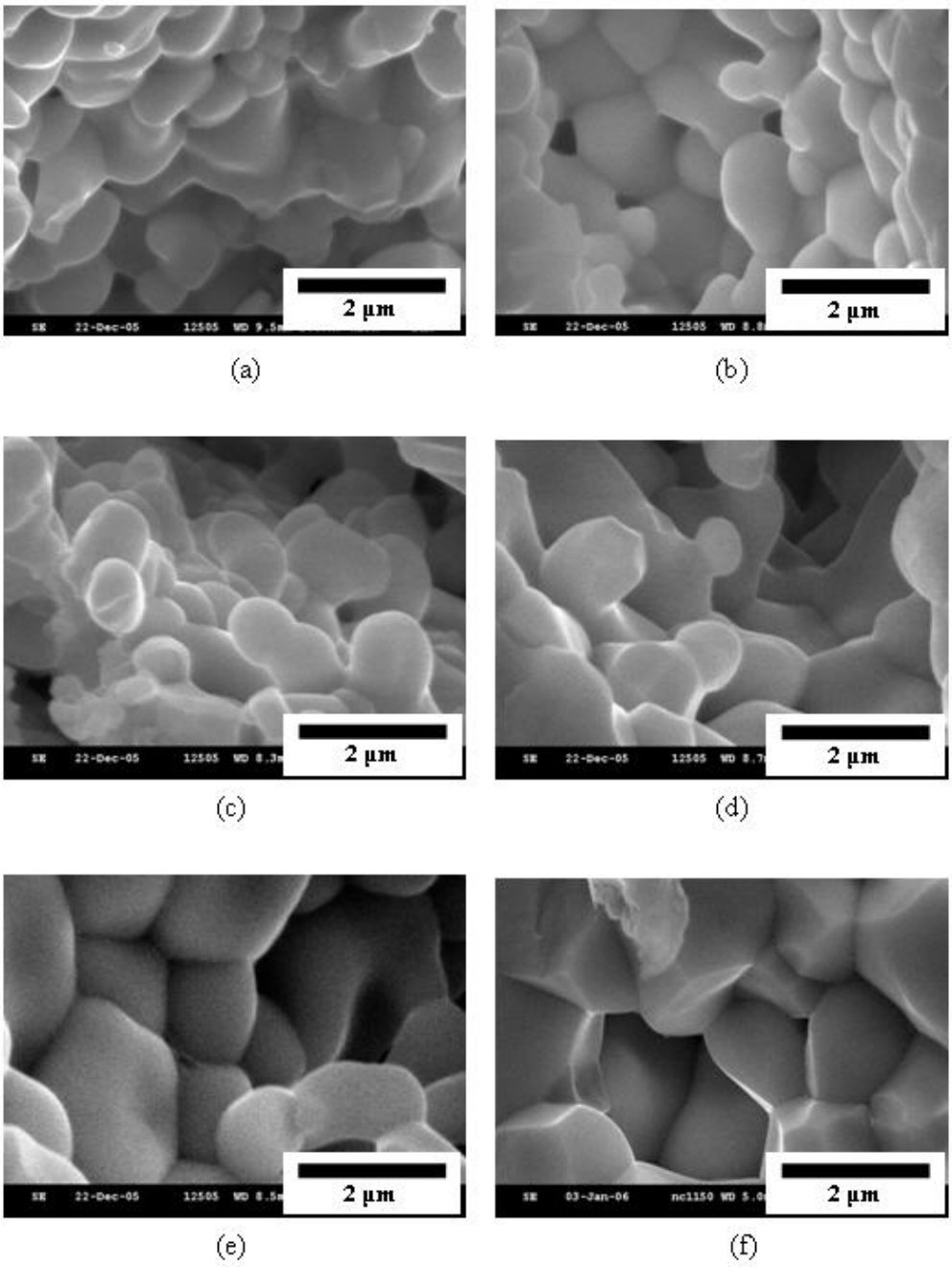

Figure **4.16**: SEM images of the samples sintered at 900°C for 2h in $0.8Pb(Zr_{0.48}Ti_{0.52})O_3$ - $0.2Pb[\ 0.7\ \{0.7(Zn_{0.8}Ni_{0.2})_{1/3}\ (Nb_{0.9}Sb_{0.1})_{2/3}–0.3Li_{1/4}(Nb_{0.9}Sb_{0.1})_{3/4}\}\ –\ 0.3\ Mn_{1/3}\ (Nb_{0.9}Sb_{0.1})_{2/3}\ ]O_3$ + x wt% CuO ceramics.: (a) x=0.1, (b) x=0.2, (c) x=0.3 (d) x=0.4 (e) x=0.5 and (f) x=0.6.

Density, dielectric permittivity ($\varepsilon^{T}_{3}/\varepsilon_{0}$), electromechanical coupling factor (k_p), mechanical quality factor and piezoelectric constant (d_{33}) were all plotted as a function of the amount of CuO addition, fired at 900 ^{o}C for 2 h, in figure **4.17**. A critical volume factor of CuO is required in order to get the microstructure homogenized and undergoing critical kinetic processes that underpin liquid phase sintering such as particle rearrangement, dissolution re-precipitation and grain growth. The density was increased with an increase of CuO content from 6.4 to 7.8 g/cm^3. This improvement of the density might be related to the formation of the liquid phase. Moreover, accompanying the densification is a variation of piezoelectric and dielectric properties. Therefore, the improved piezoelectric and dielectric properties, which were observed in the range of copper oxide addition of $x \geq 0.3$, might be due to the increased density as well as increased grain size shown in figure **4.16**.

Figure **4.18** shows the variation in the dielectric constant of the $0.8Pb(Zr_{0.48}Ti_{0.52})O_3$ - $0.2Pb[\ 0.7\ \{0.7(Zn_{0.8}Ni_{0.2})_{1/3}\ (Nb_{0.9}Sb_{0.1})_{2/3} – 0.3Li_{1/4}(Nb_{0.9}Sb_{0.1})_{3/4}\}$ – $0.3\ Mn_{1/3}\ (Nb_{0.9}Sb_{0.1})_{2/3}\ ]O_3$ + x wt% CuO ceramics sintered at 900 ^{o}C for 2h as a function of temperature. The magnitude of the dielectric constant at T_{max} (the temperature that shows the maximum dielectric permittivity) increased with the addition of CuO. This enhancement of the dielectric permittivity is correlated with the increase in the density and grain size of the samples as shown in figure **4.19**. T_c was slightly decreased approximately from 300 ^{o}C in the range of $0.1 \leq x \leq 0.2$ to 280 ^{o}C when x exceeded 0.2. Similarly, the tetragonality of the peaks in XRD patterns was increased in the range of $x \geq 0.3$ as shown in figure **4.15** (a)-(f).

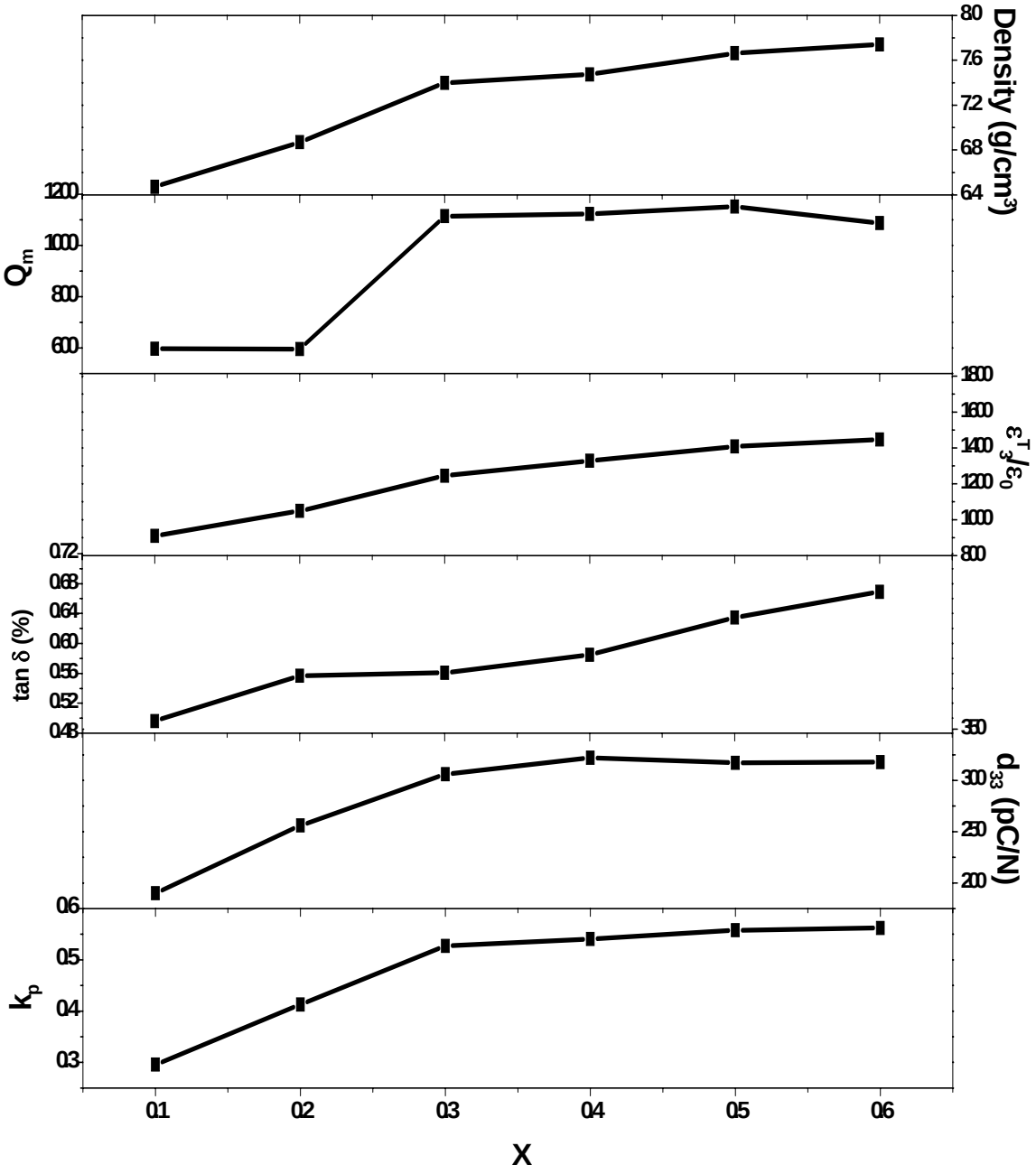

Figure **4.17**: Density, dielectric permittivity ($\varepsilon^T_3/\varepsilon_0$), electromechanical coupling factor (k_p), mechanical quality factor (Q_m) and piezoelectric constant (d_{33}) of the specimens sintered at 900°C for 2h in $0.8Pb(Zr_{0.48}Ti_{0.52})O_3$ - $0.2Pb[\ 0.7\ \{0.7(Zn_{0.8}Ni_{0.2})_{1/3}(Nb_{0.9}Sb_{0.1})_{2/3}–0.3Li_{1/4}(Nb_{0.9}Sb_{0.1})_{3/4}\} – 0.3\ Mn_{1/3}\ (Nb_{0.9}Sb_{0.1})_{2/3}\ ]O_3$ + x wt% CuO ceramics.

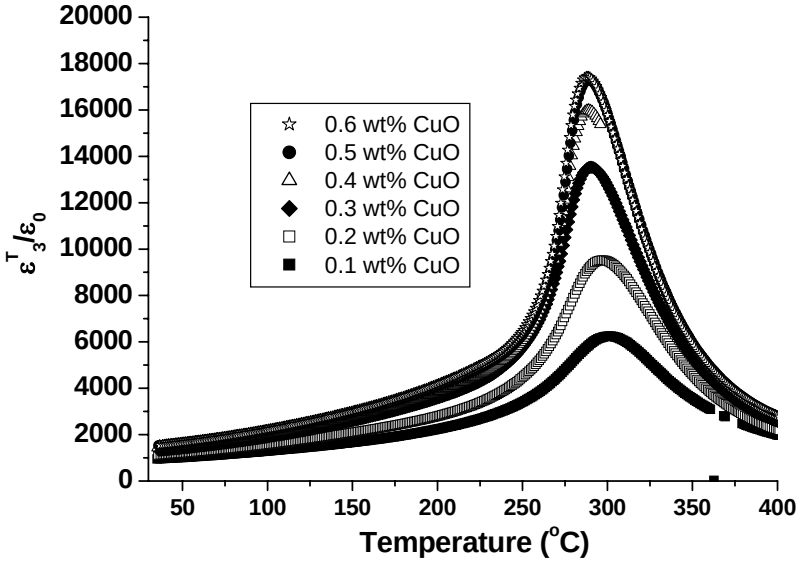

Figure **4.18**: Temperature vs dielectric permittivity ($\varepsilon^T_3/\varepsilon_0$) of the specimens sintered at 900^{o}C for 2h in $0.8Pb(Zr_{0.48}Ti_{0.52})O_3$ - $0.2Pb[\ 0.7\ \{0.7(Zn_{0.8}Ni_{0.2})_{1/3}\ (Nb_{0.9}Sb_{0.1})_{2/3}$– $0.3Li_{1/4}(Nb_{0.9}Sb_{0.1})_{3/4}\}$ – $0.3\ Mn_{1/3}\ (Nb_{0.9}Sb_{0.1})_{2/3}\ ]O_3$ + x wt% CuO ceramics.

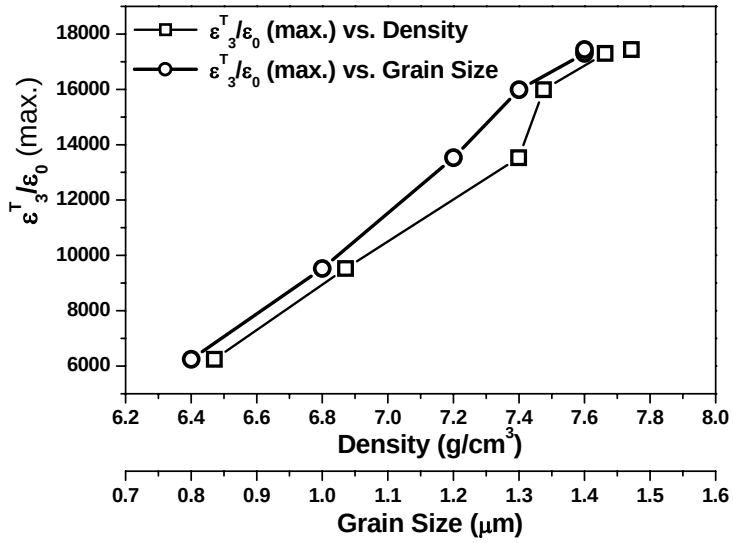

Figure **4.19**: Density and grain size effect on dielectric constant by CuO addition.

Figure **4.20** shows polarization versus electric field curves of 0.8 Pb $(Zr_dTi_{1-d})O_3$ - 0.2 Pb [0.7 { 0.7 ($Zn_{0.8}Ni_{0.2}$)$_{1/3}$ ($Nb_{0.9}$ $Sb_{0.1}$)$_{2/3}$ – 0.3 $Li_{1/4}$ ($Nb_{0.9}$ $Sb_{0.1}$)$_{3/4}$ }–0.3 $Mn_{1/3}$ ($Nb_{0.9}$ $Sb_{0.1}$)$_{2/3}$]O_3 + x wt % CuO ceramics (d=0.48, 0.5 and x=0, 0.5). Sintering conditions for x=0 cases were 1200 ^oC for 2h. The coercive field (E_c) of the ceramic with d=0.5 and x=0 was 1.06 kV/mm. It decreased to 1.00 kV/mm when the Zr/Ti ratio (d) was adjusted to 0.48 to increase d_{33} value. Meanwhile the remnant polarization (P_r) increased from 19 μC/cm^2 to 39 μC/cm^2. These results of a decreased E_c and an increased P_r are consistent with the increase in soft characteristics with adjusting the Zr/Ti ratio, which were shown in figure **4.12**. For d=48 and x=0.5 case, the sample was sintered at 900 ^oC for 2h. Due to this low temperature sintering conditions, ferroelectric hysteretic response in reduced and the E_c and P_r were 0.75 kV/mm and 11.5 μC/cm^2, respectively.

For the practical ultrasonic motor application with high voltage/power drive condition, the vibration velocity was measured for the $0.8Pb(Zr_{0.48}Ti_{1-48})O_3$ - 0.2Pb[0.7 $\{0.7(Zn_{0.8}Ni_{0.2})_{1/3}(Nb_{0.9}Sb_{0.1})_{2/3}–0.3Li_{1/4}(Nb_{0.9}Sb_{0.1})_{3/4}\}$ – 0.3 $Mn_{1/3}(Nb_{0.9}Sb_{0.1})_{2/3}$]O_3 + x wt% CuO ceramics (x = 0.1 ~ 0.6) as a function of applied electric field (rms value). In figure **4.21** , small amount of CuO added cases showed high vibration velocity of over 0.6 m/s, but it required high electric fields. As the addition amount of CuO increased, high vibration velocity was obtained with lower electric field owing to enhanced electro-mechanical properties. Over 0.5 wt% added, the maximum vibration was saturated at around 0.48 m/s. This vibration level is almost equal to that of high temperature sintered piezoelectric ceramics (~0.5 m/s) [**2**,**70**].

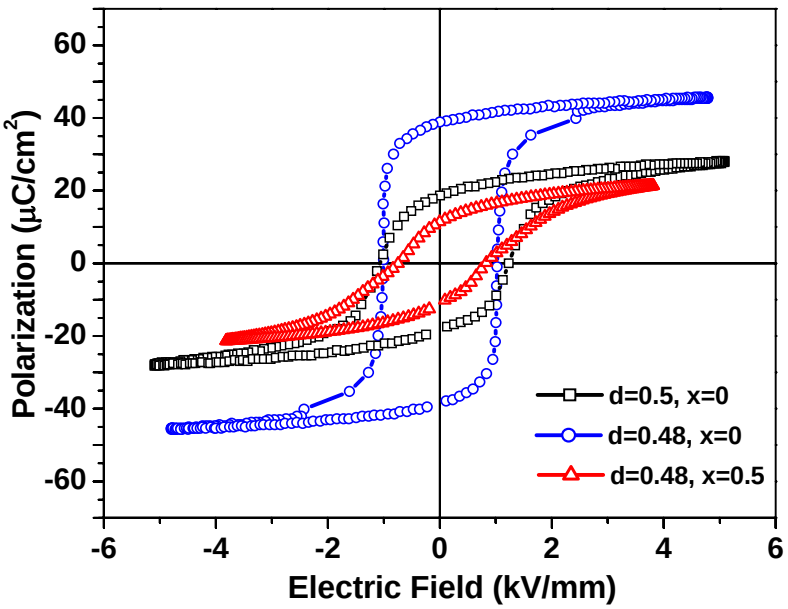

Figure **4.20**: Polarization vs. electric field curves of key compositions: 0.8 Pb $(Zr_dTi_{1-d})O_3$ - 0.2Pb [0.7 {0.7 $(Zn_{0.8}Ni_{0.2})_{1/3}$ $(Nb_{0.9}Sb_{0.1})_{2/3}$ – $0.3Li_{1/4}(Nb_{0.9}Sb_{0.1})_{3/4}$} – $0.3Mn_{1/3}(Nb_{0.9}Sb_{0.1})_{2/3}]O_3$ + x wt % CuO added ceramics.

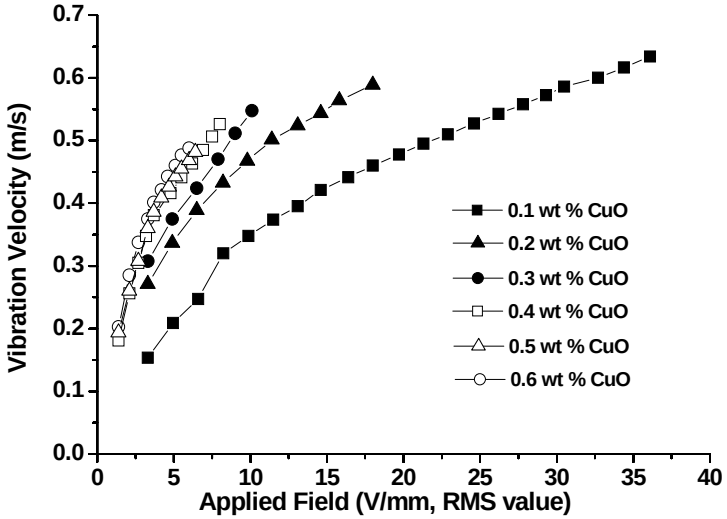

Figure **4.21**: Vibration velocity variation of the $0.8Pb(Zr_{0.48}Ti_{1-0.52})O_3$ - 0.2Pb [0.7 {0.7 $(Zn_{0.8}Ni_{0.2})_{1/3}$ $(Nb_{0.9}Sb_{0.1})_{2/3}$ – $0.3Li_{1/4}(Nb_{0.9}Sb_{0.1})_{3/4}$} – $0.3Mn_{1/3}(Nb_{0.9}Sb_{0.1})_{2/3}]O_3$ + x wt % CuO added ceramics (x=0.1 ~ 0.6)

4.4 Chapter Summary

In this chapter, a high-power, piezoelectric ceramic was developed as a base composition for low-temperature sintering. Sb, Li, and Mn were substituted into the $0.8Pb(Zr_{0.5}Ti_{0.5})O_3$-$0.16Pb(Zn_{1/3}Nb_{2/3})O_3$-$0.04Pb(Ni_{1/3}Nb_{2/3})O_3$ ceramics. All of these substituents shifted the structure from a tetragonal composition to a pseudo-cubic phase. The Sb and Li substitutions resulted in an increase of k_p and d_{33}, while Mn enhanced the Q_m value. The composition $0.8Pb(Zr_dTi_{1-d})$ - $0.2Pb[(1 - c)\{(1 - b)\ (Zn_{0.8}\ Ni_{0.2})_{1/3}\ (Nb_{1-a}\ Sb_a)_{2/3} - b\ (Li_{1/4}\ (Nb_{1-a}\ Sb_a)_{3/4})\ \} - c\ (Mn_{1/3}\ (Nb_{1-a}\ Sb_a)_{2/3})]O_3$ (a=0.1, b=0.3, c=0.3 and d=0.5) showed the value of k_p=0.56, Q_m=1951 (planar mode), d_{33}=239pC/N, $\varepsilon^T_3/\varepsilon_0$=739, and the maximum vibration velocity=0.6 m/s at 31-mode. By adjusting the Zr/Ti ratio, the structure of the ceramic was moved back to the morphotropic phase boundary and presented k_p=0.57, Q_m= 1502 (planar mode), d_{33}=330 pC/N, $\varepsilon^T_3/\varepsilon_0$=1653, and the maximum 31-mode vibration velocity=0.58 m/s when Zr/Ti=0.48/0.52.

Low-temperature sintering of Sb-, Li-, and Mn-substituted $Pb(Zr_{0.48}Ti_{0.52})O_3$-$Pb(Zn_{1/3}Nb_{2/3})O_3$-$Pb(Ni_{1/3}Nb_{2/3})O_3$ ceramics has been investigated using CuO as a sintering aid. The composition of $0.8Pb(Zr_{0.48}Ti_{0.52})O_3$ - $0.2Pb[\ 0.7\ \{0.7(Zn_{0.8}Ni_{0.2})_{1/3}\ (Nb_{0.9}Sb_{0.1})_{2/3}–0.3Li_{1/4}(Nb_{0.9}Sb_{0.1})_{3/4}\} - 0.3\ Mn_{1/3}\ (Nb_{0.9}Sb_{0.1})_{2/3}\ ]O_3$ has excellent piezoelectric and dielectric properties for high-power applications. However, the sintering temperature of this composition is rather high (1200 ^oC) to be cofired with LTCC system. In this chapter, the addition of CuO as a sintering agent was proposed. It was found that CuO can sustain reasonable piezoelectric properties even when the base composition developed for this research was sintered at low temperature. The composition

$0.8Pb(Zr_{0.48}Ti_{0.52})O_3$ - $0.2Pb[\ 0.7\ \{0.7(Zn_{0.8}Ni_{0.2})_{1/3}\ (Nb_{0.9}Sb_{0.1})_{2/3}–0.3Li_{1/4}(Nb_{0.9}Sb_{0.1})_{3/4}\}$ – $0.3\ Mn_{1/3}\ (Nb_{0.9}Sb_{0.1})_{2/3}\ ]O_3$ + 0.5 wt% CuO exhibited the values of k_p=0.56, Q_m= 1152 (planar mode), d_{33}=317 pC/N, $\varepsilon^T_3/\varepsilon_0$=1409, and the maximum vibration velocity=0.48 m/s for the 31-mode, when sintering was done at 900 ^oC for 2 h. The properties for the optimized compositions are shown in the Table **4.1**. The high temperature sintered samples showed better hard characteristics than commercialized APC-841. Low temperature sintered ceramics demonstrated a slight deterioration but still showing more than 1000 in Q_m and 300 in d_{33} values.

Table **4.1**: The materials properties summary.

Composition	Sintering Temp. (^oC)	Q_m (planar)	$\varepsilon^T_3/\varepsilon_0$	d_{33} (pC/N)	k_p	k_{31}	T_c (^oC)	v_o (m/s)
d = 0.5 x = 0 (High Temp.)	1200	1951	739	239	0.56	0.3	286	0.6
d = 0.48 x = 0 (High Temp.)	1200	1502	1653	330	0.57	0.33	290	0.58
d = 0.48 x = 0.5 (Low Temp.)	900	1152	1409	317	0.56	0.32	289	0.48
APC 841 (High Temp.)	1250	1400	1350	300	0.6	0.33	320	0.6
Composition Formula: $0.8Pb(Zr_dTi_{1-d})O_3$ - $0.2Pb[\ 0.7\ \{0.7(Zn_{0.8}Ni_{0.2})_{1/3}\ (Nb_{0.9}Sb_{0.1})_{2/3}–0.3Li_{1/4}(Nb_{0.9}Sb_{0.1})_{3/4}\} – 0.3\ Mn_{1/3}\ (Nb_{0.9}Sb_{0.1})_{2/3}\ ]O_3$ + x wt% CuO								

Chapter 5

DESIGN OF A 2-DEGREE OF FREEDOM ULTRASONIC MOTOR

5.1 Chapter Overview

This chapter explores the design options for a piezoelectric ultrasonic motor, in particular, the geometric optimization and properties measurement confirmation of a prototype for 2-degrees of freedom motor operation. Various shapes and geometries were considered such as L and delta structured motors. Ultimately, these motors are refined into a bimorph design capable of having 2-degrees of freedom motions at the tip. Within the work outlined below, finite element calculations were made to aid in the design, together with experimental characterization of the motors to verify design trends.

5.2 Principles of the Motor Operation

The basic motor design to be considered in this study was L-shaped, consisted of two piezoelectric rectangular bars joined at a 90^o angle. The fundamental structure of the motor and the various design variables include width (w), thickness (t), angle (θ), and length of the legs (ℓ). Figure **5.1**, schematically shows the basic design and variables.

Two driving voltage source inputs with a 90^o phase difference are applied in the form of:

$$V_{in1}=V_o \sin(\omega t) \qquad \text{(Eq. 5)}$$

$$V_{in2}=V_o \cos(\omega t) \qquad \text{(Eq. 6)}$$

where V_o is peak voltage (Volts), ω is frequency (radians/second) and t is time (seconds). Two resonance modes can be generated in this motor structure as shown in figure **5.2**. One resonance mode produces a vibrational motion along the normal direction to a driving surface and the second mode creates a parallel motion relative to the surface motion. Superimposing the two modes, at an in-between drive frequency, results in an elliptical displacement at the motor tip. Clockwise and counter clockwise motion can be obtained by applying inverse input signals.

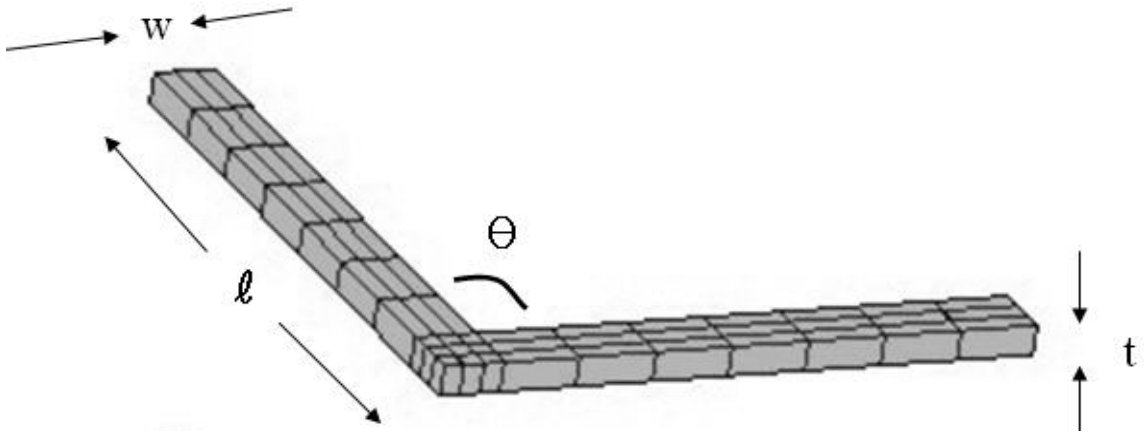

Figure **5.1**: Fundamental structure and design variables for the Λ-shape motor.
(w: width, ℓ: length, t: thickness and θ: angle).

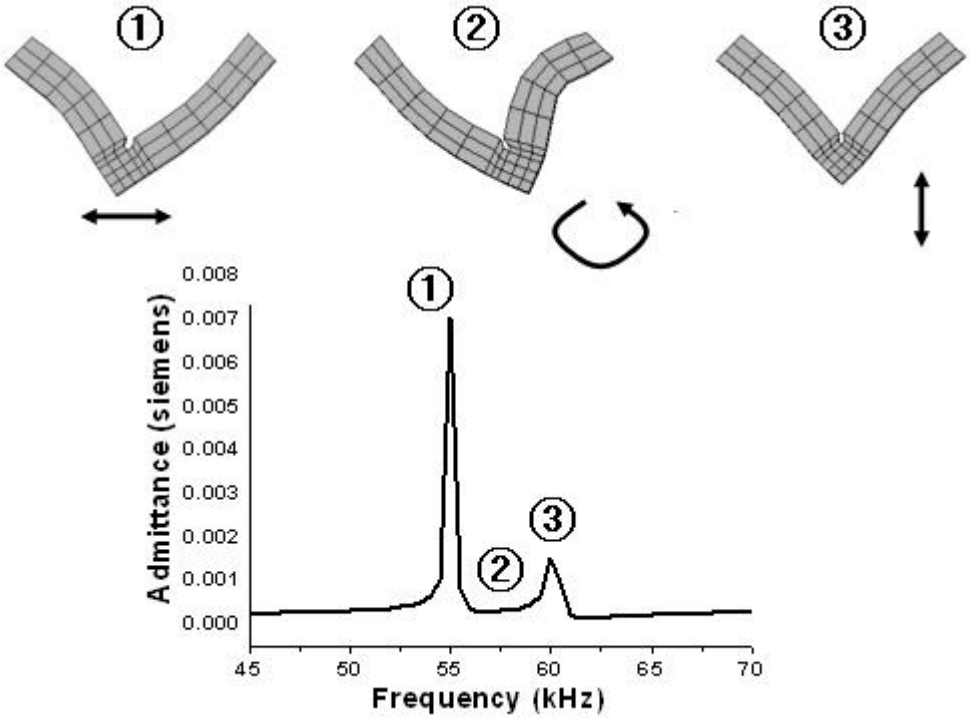

Figure **5.2**: Motion of the motor when driven at various frequencies ① and ③ are the fundamental motions, ② is the frequency at which superimposes and into an elliptical displacement.

5.3 Lambda-shaped Motor Optimization

Using the ATILA simulation, the basic performance of the motor with various drive conditions and geometries was analyzed. The length was fixed as 10 mm to fulfill the requirement for a new generation of small piezoelectric motors. To simplify the modeling, thickness and driving voltage were also fixed as 0.5 mm and 1 V, respectively. By changing the width (w) and angle (θ), frequencies and vibrational amplitudes can be

changed. As shown in figure **5.2**, the elliptical motion at the motor tip is induced through the superimposing of two resonance vibration modes. Therefore, the maximum elliptical displacement can be obtained when the gap between two resonance frequencies is minimized. Figure **5.3** shows the relation between the width of stator and the displacement of the motor at the tip for constant width length and angle (90^o). The width that would indicate the maximum displacement at the motor tip was 1.5 mm, and this would be approximately an order of magnitude times higher displacement than a structure with a width of 2.5 mm.

In addition to changes in width (w), magnitude of the relative resonance frequencies can also be varied through different angles (θ). The modeled resonance peaks in the range of 70 to 86 kHz, for angles of 95^o, 90^o, 85^o, 80^o and 75^o is shown in the figure **5.4**. These thick lines indicate displacement along x-axis and the thin lines show displacement along y-axis. These two motions are corresponding to the two resonance modes which were shown in figure **5.2**. By changing θ, the resonance mode that provides x-axis directional bending is shifted to the higher frequency range, while the y-axis directional bending mode is moved down to lower frequency region. These two modes came closest to each other when $\theta=80^o$. At this angle, the maximum elliptical displacement at the motor tip is expected. In this study, the angle change was found to be the most effective way to obtain maximum elliptical displacement.

In addition to changes in width (w), magnitude of the relative resonance frequencies can also be varied through different angles (θ). The modeled resonance peaks in the range of 70 to 86 kHz, for angles of 95^o, 90^o, 85^o, 80^o and 75^o is shown in the figure **5.4**. These thick lines indicate displacement along x-axis and the thin lines show

displacement along y-axis. These two motions are corresponding to the two resonance modes which were shown in figure **5.2**. By changing θ, the resonance mode that provides x-axis directional bending is shifted to the higher frequency range, while the y-axis directional bending mode is moved down to lower frequency region. These two modes came closest to each other when $\theta=80^{o}$. At this angle, the maximum elliptical displacement at the motor tip is expected. In this study, the angle change was found to be the most effective way to obtain maximum elliptical displacement.

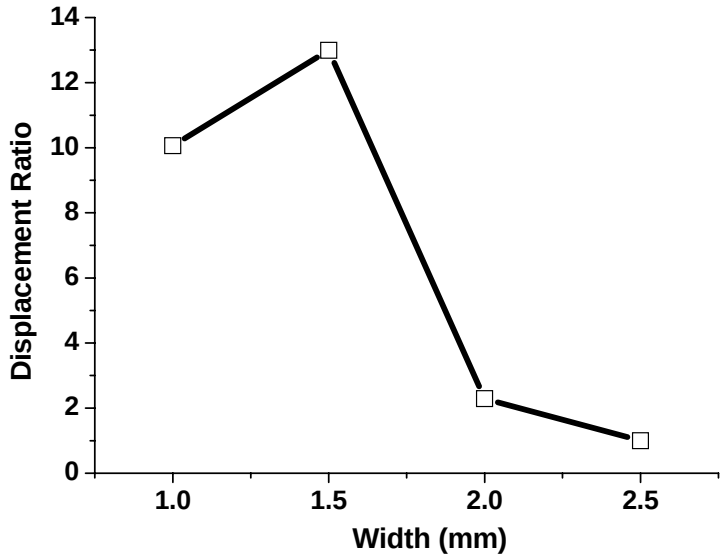

Figure **5.3**: Displacement ratios of the motors with various widths (1.0~2.5 mm) when displacement ratios are relative to the 2.5 mm width motor.

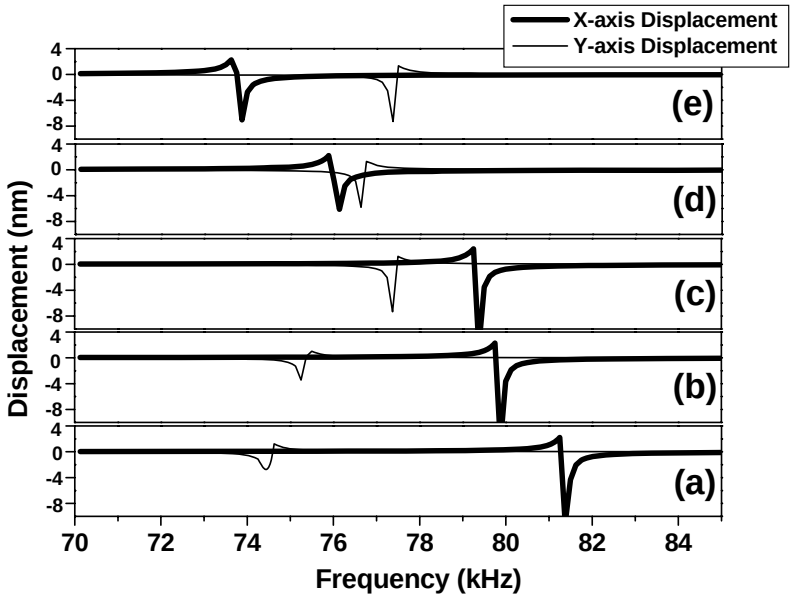

Figure **5.4**: Displacement at the motor tip with various angles(θ): (a) 95^{o}, (b) 90^{o}, (c) 85^{o}, (d) 80^{o} and (e) 75^{o}, with a driving condition of 1 V_{pp}.

5.4 2-degrees of Freedom Ultrasonic Motor

Based on the effects of dimensional changes observed for the lambda-shape motors, we now consider a more complex motor that involves the bonding of two lambda motors and a common bar. The basic structure is shown in figure **5.5**, with four input electrodes and one ground electrode. The main advantage of this bimorph structure is to obtain two degrees of freedom for the motor under drive condition. In addition, the inactive bar was used to obtain the surface for the ground electrode and a feature that will later aid the integration of the motor into packaged structure.

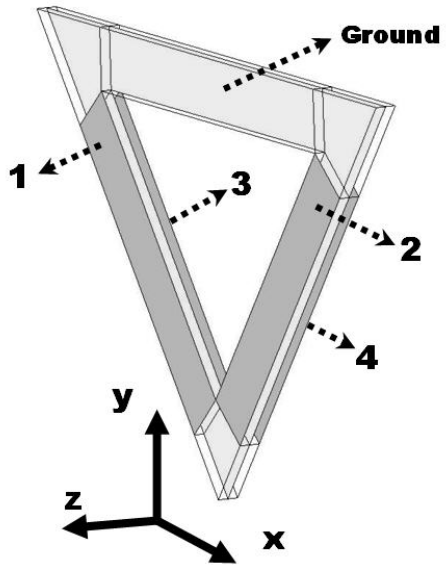

Figure **5.5**: Electrodes of the bimorph type delta-shape motor: 1, 2, 3 and 4 indicate four input electrodes.

Table **5.1** summarizes modeling results of how different drive conditions into the electrode ultimately control the bimorph delta-shape motor in 2-dimensional space. When the z-axis was used as the polarization direction, 2-dimensional motion was observed in x-z plane. The x-axis directional motion is the same as with the single layer case. For z-axis motion, a fundamental principle of driving is the same with x-axis case. Two phases were applied into 1 and 2 electrodes and other two phases with 90^o phase difference were given into 3 and 4 electrodes. For positioning efficiency, diagonal motion of the motor may be needed. This action can be achieved by applying three signals with same phase and one signal with 90^o phase difference. Beyond the modeling performed here it is noted that vibration amplitude, frequency and load condition can all determine the speed of the

motor, as the driving force depends on the friction between the contact point of stator and slider, this is more difficult to model.

ATILA simulation results for the bimorph structure delta-shape motor are summarized in the figure **5.6**. Total thickness of the motor was maintained as 0.5mm (0.25 mm for each layer) and other parameters were the same as in the lambda-shape motor case. At an angle of 80^{o}, all of the x, z and diagonal-axis directional motions were observed at 65 kHz. The resonance frequency differences between lambda and delta motors might be due to the additional inactive bar and common ground electrode between two lambda motors. Consequent motions are also shown next to the displacement graphs. The important aspect of the results beyond the geometric trends is that this motor can have 2-degrees of freedom at the motor tip at specific frequencies.

Table **5.1**: 2-dimensional driving conditions for the bimorph type delta-shape motor.

Direction \ Electrode	1	2	3	4
+ x	SIN	COS	SIN	COS
- x	COS	SIN	COS	SIN
+ z	COS	COS	SIN	SIN
- z	SIN	SIN	COS	COS
+ x and + z	SIN	COS	SIN	SIN
+ x and – z	SIN	SIN	SIN	COS
- x and + z	COS	SIN	SIN	SIN
- x and – z	SIN	SIN	COS	SIN

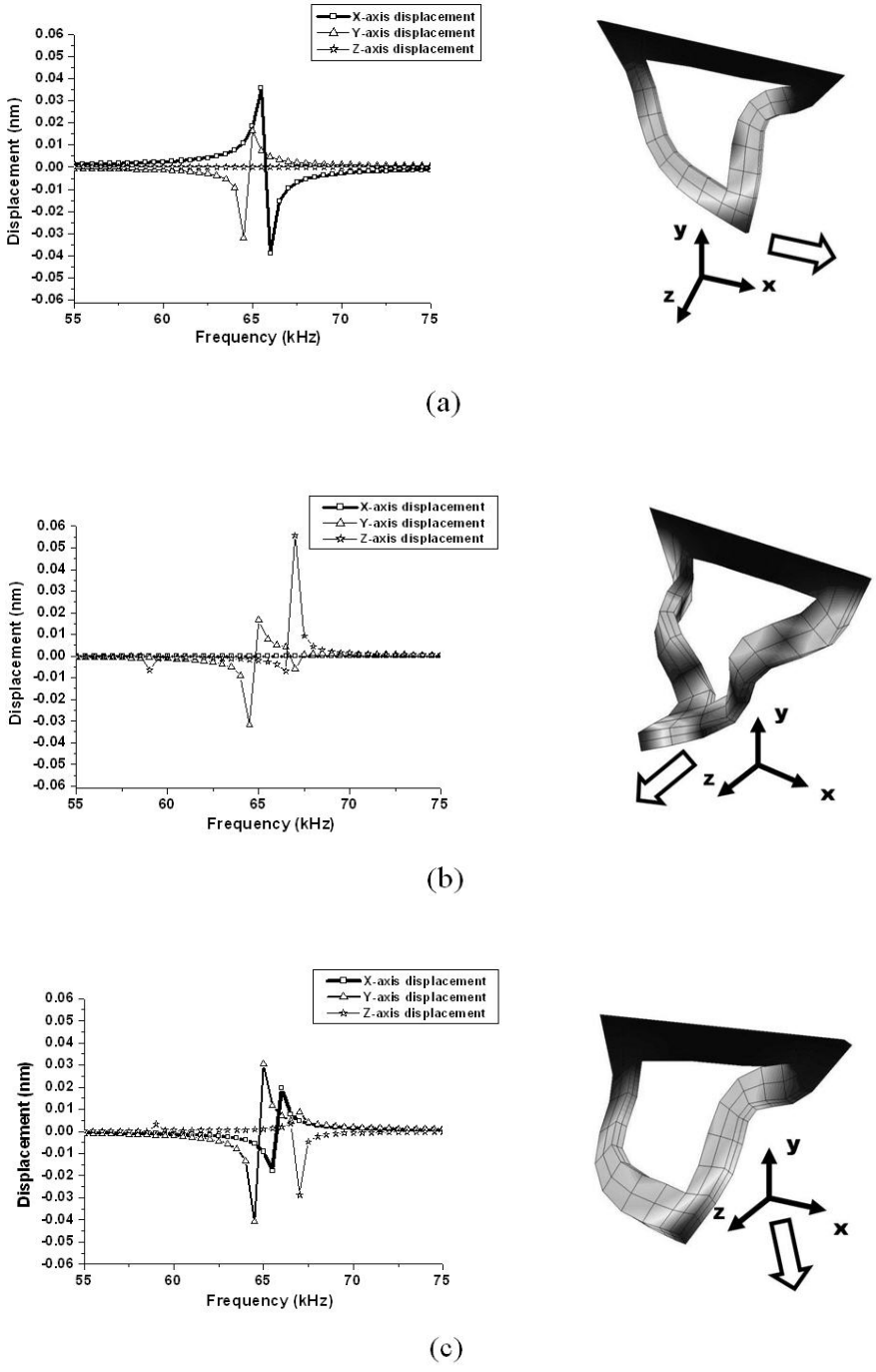

Figure **5.6**: FEM simulation results for 2-dimensional driving of the bimorph type Δ-shape motor for the: (a) x-axis, (b) z-axis and (c) diagonal axis movement.

5.5 Experimental Evaluation of Motors

Fabricated bimorph-structure delta motors are shown in the figure **5.7** (a). They are prepared by a punch and bond method which is described in Chapter 3.2. The delta motors maintain the angle (θ), during a sintering process, while the lambda motor was found to experience an approximately 5^{o} change. The SEM image shows a side view of the motor with inner electrode. The vertical stripes with around 200 μm width were observed and these are from the punching process of the tape.

Figure **5.8** shows the displacements at the motor tip as measured by a laser interferometer for x vs. y and x vs. z axis under various driving voltages. Several tens of nanometer displacements with elliptical motions were measured along the x and z axis. At 78 kHz, both x and z directional motions were observed simultaneously, by utilizing a single frequency driving for the two motions. A single frequency driving simplifies the driving circuit that finally reduces the production cost. Then to obtain the required displacements, the applied voltage magnitude can be changed to control to the elliptical motion. This possibility was experimentally observed in figure **5.8**. Resonance modes of piezoelectric materials shift with applied electric field level. Furthermore, there is non-linearity in piezoelectricity, even though it is not considered in FEM simulations. This could be a reason for the abrupt increase in displacement amplitude at the driving condition of 70 V_{pp}. The speed of the motor was calculated from the driving frequency and displacement at the motor tip. When the motor rotates a 19 mm diameter bearing under a 70 V_{pp} driving voltage condition, 7.4 radians/sec and 2.5 radians/sec were expected for x and z directional motions, respectively.

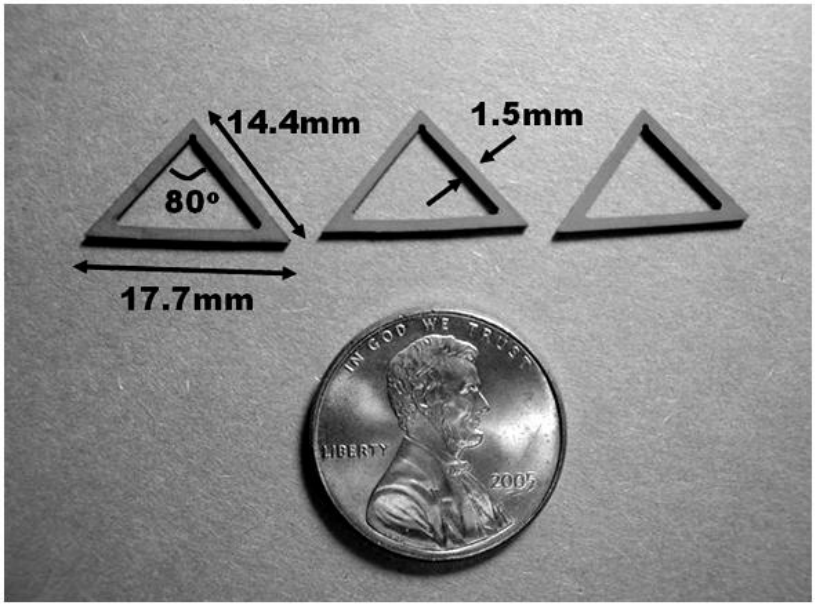

(a)

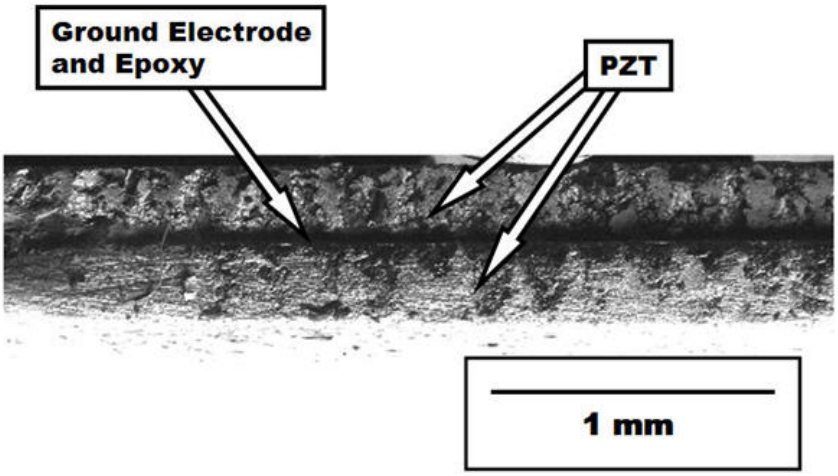

(b)

Figure 5.7: Bimorph structure delta shape motor: (a) fabricated motors from thick films and (b) a side view SEM image of the motor.

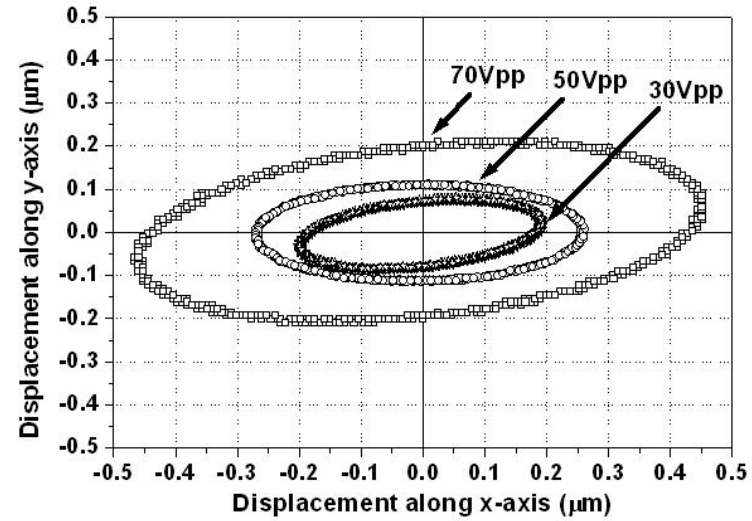

(a)

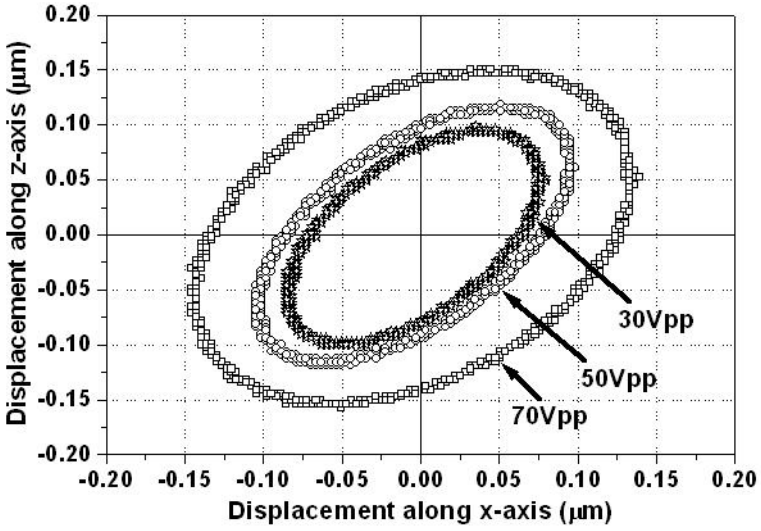

(b)

Figure **5.8**: Displacement at the motor tip measurement result by laser interferometer: (a) x-axis and (b) z-axis directional motions.

A method, outlined by Nakamura et al. [**71**], can be used to characterize torque, speed of revolution and efficiency of the motor. To use this method, transient speed of the motor was measured for a pre-load condition of 1.1 N. Angular acceleration is equal to the time rate of change of transient speed. Therefore, the torque is the product of the moment of inertia of the load and the angular acceleration.

A metallic bearing with weight of 5.9 g and diameter of 19 mm, i.e. a moment of inertia of 5.04×10^{-7} $kg \cdot m^2$, was used to measure the speed, torque and efficiency. The motor was driven between 40 kHz to 100 kHz with an alternating current (AC) voltage of 100 V_{pp}. An optical encoder was used to measure the speed of revolution and transient speed. The results of speed, torque and efficiency vs. frequency data with a 1.1 N pre-load condition are summarized in figure **5.9**. The fastest speed in any direction in this range was found to be approximately 10 rad/sec. The highest torque was 3 mNm, and efficiency was ~ 20 %. In x and z directional motion cases, apparent three peaks were observed and rotation direction of the bearing was changed in between these peaks. These low speed points indicate the admittance maximum frequencies because at those frequencies motion at the motor tip is either normal or parallel to operating surface; therefore, no elliptical motion can be obtained. Furthermore, the maximum speed of 10.2 radians/sec, 7.0 radians/sec and 2.8 radians/sec for x, z and diagonal axis motions were obtained between normal and parallel motions. These maximum speed frequencies are in excellent agreement with the ATILA simulation results, shown in figure **5.6**. The small 5 kHz deviation might be due to pre-load condition and thicknesses of epoxy and electrodes which were not considered in the simulation.

A maximum torque of 2.8 mNm and thrust of 1.09×10^{-3} N was obtained along x directional movement when the bearing started to rotate. This small thrust compare to the pre-load condition of 1.1 N might be due to a small friction between the motor tip (ceramic) and the bearing surface (steel). The input electrical power to the motor was measured by monitoring input voltage and current with phase difference simultaneously with rotation speed measurement in order to calculate the efficiency of the motor. The output power is the product of the torque and the angular speed of the motor. Therefore, the efficiency can be calculated as

efficiency = (Torque (Nm) x Angular Speed (radians/sec)) / Input Power (W) (Eq. 7)

A maximum efficiency of 18 % was obtained for z directional motion, when the torque was 1.6 mNm and the motor reached maximum output power of 9.44 mW at a speed of 5.9 rad/sec. The highest efficiencies for x and diagonal motion were 9.9 % and 3.5 %, respectively. These different maximum efficiencies for each direction might be due to easy bending motion along z direction respect to x direction.

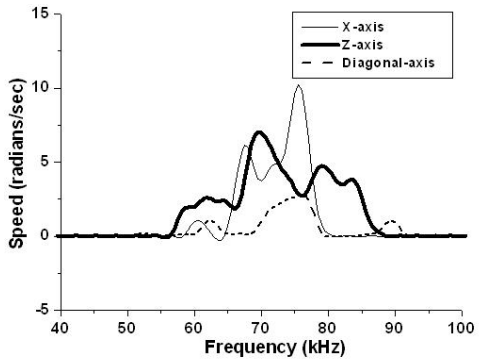

(a)

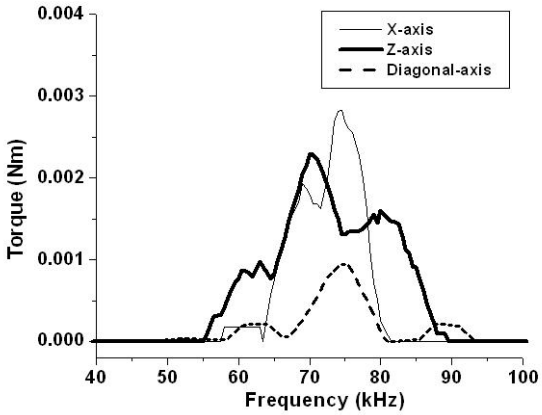

(b)

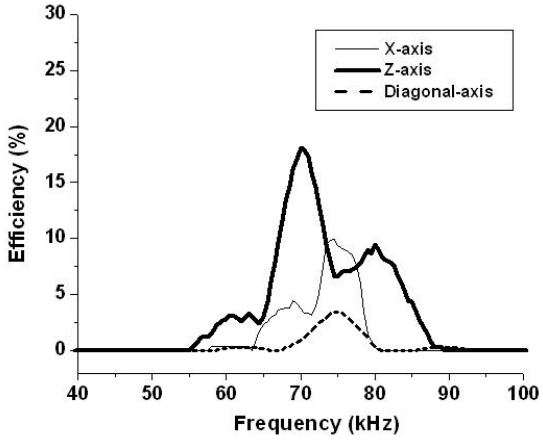

(c)

Figure **5.9**: The bimorph structure delta shape motor with pre-load 1.1 N: (a) speed, (b) torque and (c) efficiency vs. frequency.

5.6 Chapter Summary

In this chapter, the design of a miniature piezoelectric motor was outlined. The concepts, built upon previous L-shaped motors, and lead to a new delta-motor driven with 4-input electrodes and a common ground electrode with a bimorph structure. Various dimensions aspects of the design are considered, with the major goal to obtain 2-degrees of freedom that can be affected with the drive voltage phases.

Initial prototyping and testing of the delta motor was obtained with an epoxy to fabricate the basic design. From the basic testing of the motor, characteristics were confirmed and quantified, as summarized in the table **5.2**. Based on this work we can next consider the issues of integration of the delta-motor, such as cofiring the motor into a package structure.

Table **5.2**: The motor characteristics.

Direction	Speed (rad/sec)	Torque (mNm)	Power (mW)	Efficiency (%)	Driving Voltage (V_{pp})	Frequency (kHz)
z	5.9	1.6	9.4	18	100	70
x	8.3	2.8	23.2	9.9	100	74.5

Chapter 6

FABRICATION PROCESSES FOR COFIRED ULTRASONIC MOTORS

6.1 Chapter Overview

This chapter addresses a cofiring process of the materials developed in Chapter 4 and a device designed and characterized in Chapter 5. The first step for developing ultrasonic motors for cofiring, the stator of the motor was cofired with a silver electrode as an individual component. The next stage was cofiring motors with the LTCC platform structure as well as the silver electrode. Delamination, bending, and inter-diffusion were the key issues to overcome in the processing.

6.2 Cofiring with Silver Electrode

All the parts of the optical fiber alignment package, except the spring, should ultimately be cofired at the same time. The first step in the cofiring research was co-sintering the ultrasonic motor with the silver electrode (DuPont 6145) patterns. Shrinkage during sintering of piezoelectric tape was accounted for by adjusting the amount of mixing solution (FERRO Resin Solution UN1866) for tape casting. Optimized shrinkage of the tape was approximately 11 % and 13 % for in-plane and normal direction, respectively. A density of the tape was 7.4 g/cm^3 which is 3.5 % smaller than that of the bulk sample. Even though the shrinkage ratios for the PZT film and silver electrode were the same, severe delamination and bending could occur as shown in figure **6.1 (a)**. To

solve these problems, sintering conditions, such as binder burn-out temperature, holding time, and rising time were optimized. Cofiring conditions that showed the minimum structural damage were 0.25 ^{o}C/min for temperature rising steps, 4 hr for a binder burn-out period, 2 hr for sintering time, and 1 ^{o}C/min for the final cooling stage. Especially the speed of temperature increase was the critical parameter for the motor structure stability during the cofiring process. By changing the thermal treatment, the degree of delamination and bending was reduced, but the structures were still unstable in the firing process.

The next approach began with mechanical issues. It has been confirmed that a small amount of delamination, provoked by the punching and cutting processes, already exists even before the sintering process. Therefore, the punching and cutting processes were optimized to avoid delamination. A depth of punching (1 mm deeper than the film thickness), a distance gap between each punch (0.2 mm) and the size of the punch (0.3 mm) were the main optimized parameters. Another important factor in cofiring was the adhesion strength of the silver electrode. By changing the screen printing and lamination procedures, the adhesive force was increased and the delamination problem reduced. Exposure time in the air of the printed electrode was minimized for better adhesion to the tape. The lamination conditions of the printed tapes used a pressure of 30,000 psi at 80 ^{o}C. However, a small degree of bending was unavoidable due to the delta-shaped structure, which cannot release the shrinkage force as shown in figure **6.1 (b)**. The arrows in figure **6.1 (b)** indicate the force induced from sintering shrinkage, which was concentrated at the corners of the delta-shaped motor.

To release the force, various methods were contrived, such as cutting in the middle of the inactive bar to release the concentrated stress, stacking the motors during the sintering process in order to use their mass to suppress the bending force, and reducing the total size of the motor to half. Shrinking forces at the corners are proportional to the total length, so that a smaller motor would show less localized force at the corners. Finally, a motor that is free of delamination and camber is shown in figure **6.2**.

(a)

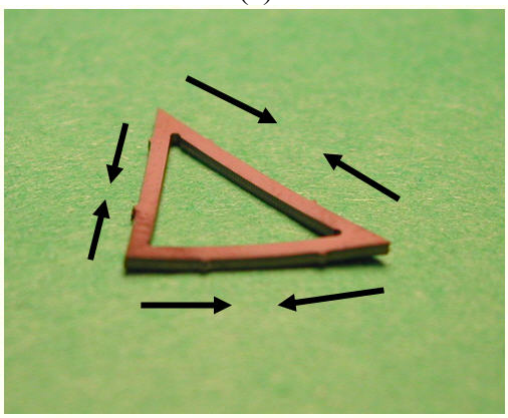

(b)

Figure **6.1**: Problems in cofiring an ultrasonic motor with silver electrode: (a) delamination and (b) camber.

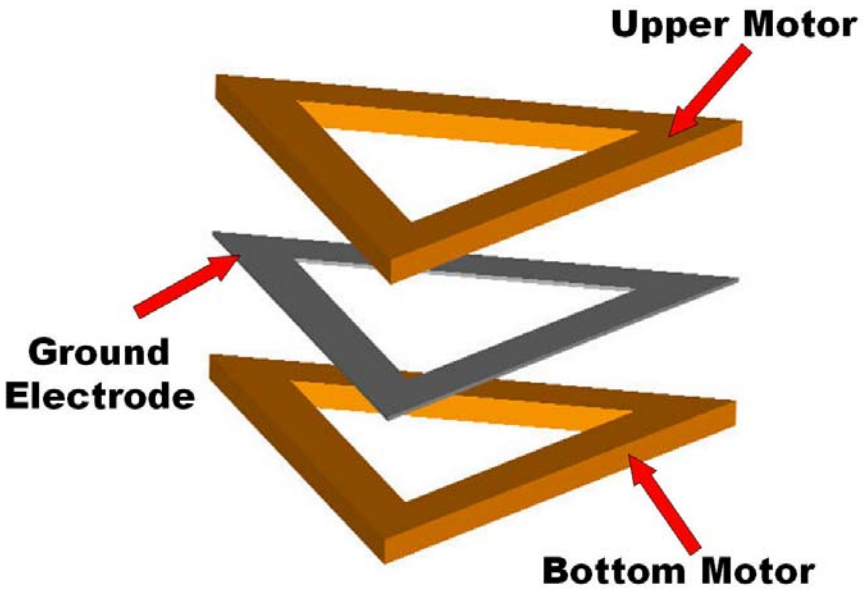

(a)

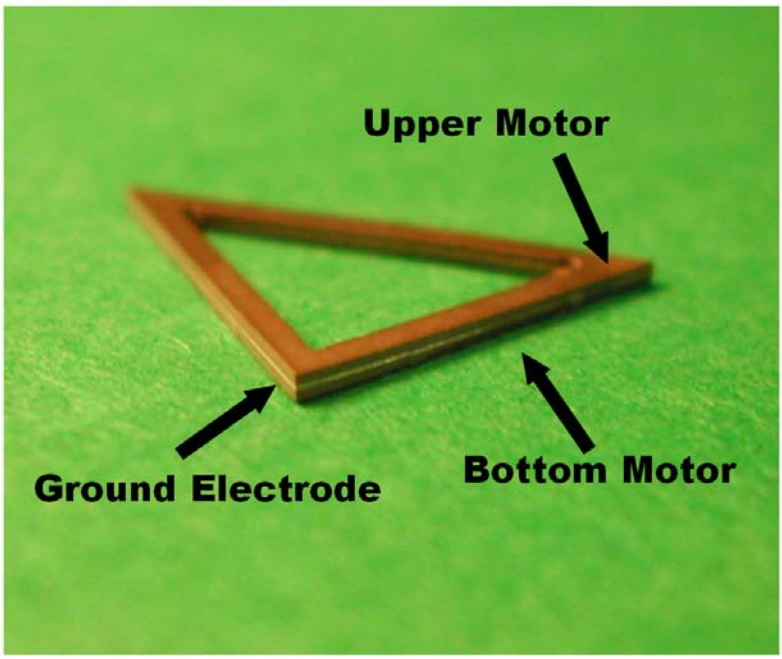

(b)

Figure **6.2**: A bimorph-structure delta-shaped ultrasonic motor with silver ground electrode: (a) schematic figure and (b) cofired sample.

6.3 Cofiring with LTCC

The final goal of the cofiring process was sintering ultrasonic motors, not only with inner silver electrodes but also with an LTCC platform structure. Based on successful cofiring of the motor with electrode owing to the reduced motor size, the investigation of cofiring with LTCC is discussed in this chapter.

Due to the very weak adhesion between PZT-based ceramics and LTCC materials (DuPont 951), various adhesive materials, such as epoxies, glues and honey/water mixtures, were tested, and silver electrode was the most effective one. However, the sintering conditions for LTCC (3-hour process), provided from DuPont, and the optimized cofiring conditions for a motor with silver electrode (3-day process) which were described in Chapter 6.2 were very different. With the LTCC firing conditions, delamination and bending occurred to the motor. Likewise, the motor with silver electrode cofiring conditions brought severe distortion in the LTCC structure. This problem was solved by providing more mechanical stability to the motor. Most of the delamination and bending initiate from the corner of the motor where an adhesion between piezoelectric film and silver electrode is the weakest. Figure **6.3** shows the new motor design and illustrates that removal of the ground electrode areas at the corners of the motor. This provided excellent resistance against structural damage during the cofiring process, so the motor can be sintered even with the firing conditions for LTCC.

A new material, the development of which is described in Chapter 4, was used in the cofiring process. In addition, motor size and design were changed to enhance structural stability against the stress from mismatched shrinkages of the components.

Therefore, design optimization of the motor using ATILA FEM simulations was again performed. The materials parameters obtained from Chapter 4 were used for this analysis.

It was modeled that changing the angles between the motor's component sides is an effective way to control two resonance modes in order to optimize the motor. This process is discussed in Chapter 5, and the angle of the motor was changed in the new design. The simulation results are shown in figure **6.4**. As the angle decreases, the gap between two resonance modes, f_2 - f_1, also decreases, i.e., the degree of superimposition increases, which would result in large elliptical motion at the motor tip. At an angle of 65^o, the gap was almost zero.

However, this was only for the x-directional motion case, therefore z-directional motions were also simulated as shown in figure **6.5**. At a 65^o angle, two resonance modes along z and y axes have considerable overlap. Though, in figure **6.5** (a), the displacement amount for the y-axis is too small. When the angle was changed to $70^o \sim 75^o$, the gap between the two modes increased similar to the x-axis case in figure **6.4**. Especially, when the angle was 70^o, the two modes are still superimposed, and displacements along the two axes are still large. Therefore, the angle of 70^o was chosen as the new optimum angle for the bimorph- structure, delta-shaped ultrasonic motor.

The newly-optimized motor that has high structural stability was successfully cofired with LTCC platform structure. The motor cofired with LTCC and silver electrode is shown in figure **6.6**. Even though the delta motor has sufficient mechanical strength to be cofired with the processing conditions for LTCC, a sintering time at 900 ^{o}C should be at least 2 hours to yield desired piezoelectric properties. Therefore firing conditions, that could provide both reasonable densification of the piezoelectric film and structural

stability of the LTCC structure, should be obtained. Finally the sintering conditions that allow the motor and LTCC package to be cofired were optimized as shown in figure **6.7**.

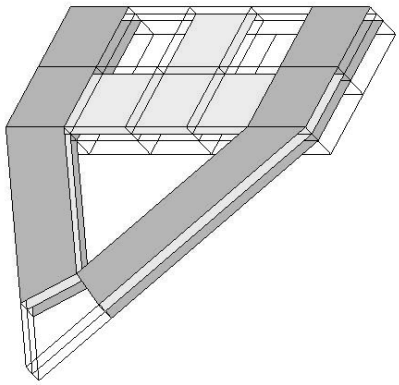

Figure **6.3**: A modified bimorph-structure delta-shaped ultrasonic motor for cofiring with LTCC.

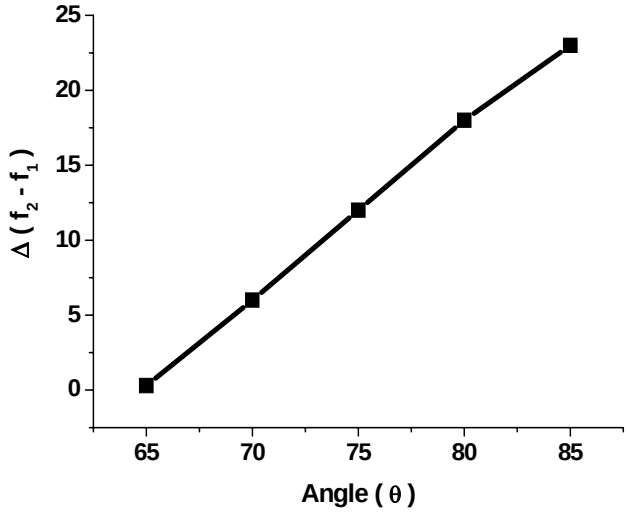

Figure **6.4**: The effect of the angle variation in resonance modes in the delta-shaped motor.

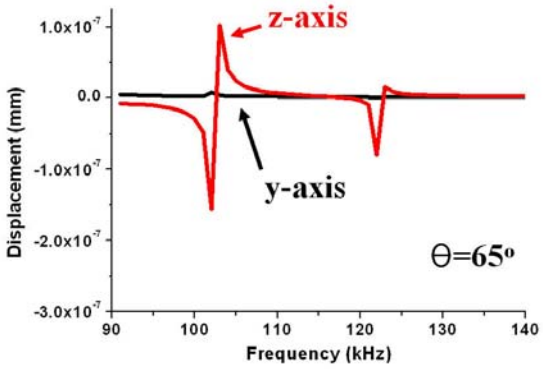

(a)

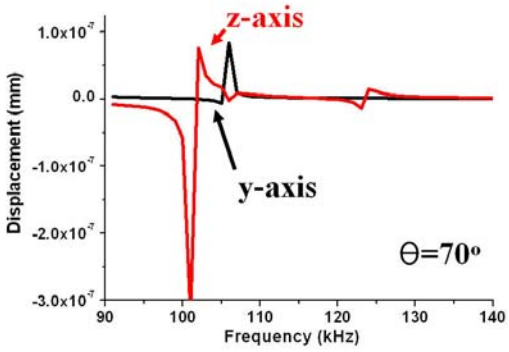

(b)

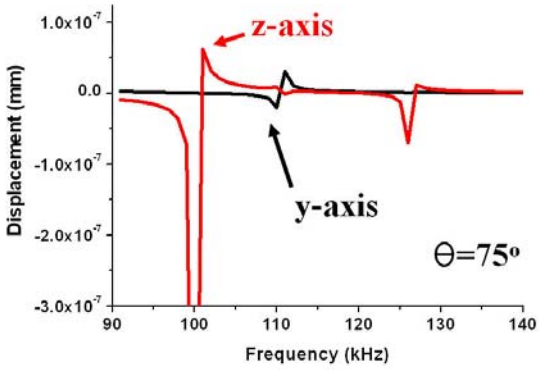

(c)

Figure **6.5**: The effect of different angles on z-directional motion of the motor: (a) $\Theta = 65^{o}$, (b) $\Theta = 70^{o}$ and (c) $\Theta = 65^{o}$.

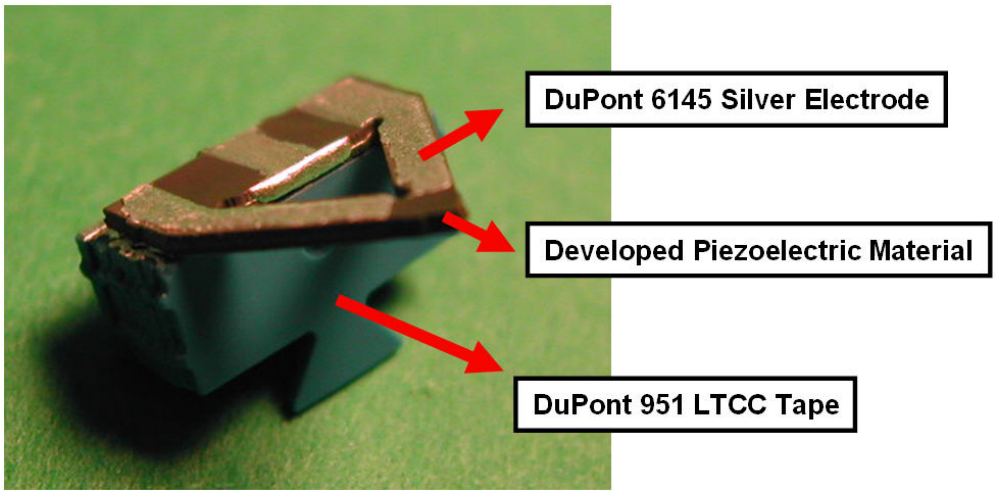

Figure **6.6**: The bimorph-structure delta-shaped ultrasonic motor cofired with LTCC and silver electrode.

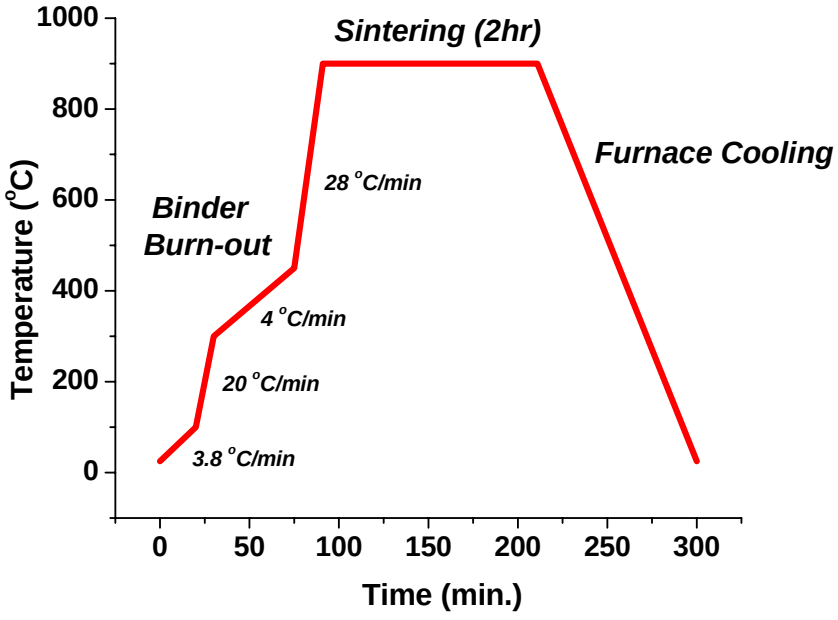

Figure **6.7**: A cofiring condition for the ultrasonic motor with LTCC.

6.4 Cofired Motor Properties

Even though the ultrasonic motor was physically cofired with LTCC platform structure and silver electrode, there are still problems such as inter-diffusion of LTCC and electrode materials into the piezoelectric-ceramic motor that would deteriorate motor properties. The first step of the investigation of the inter-diffusion issue was the use of a scanning electron microscope energy dispersive spectrometer (SEM EDS) to perform a semi-quantitative assessment of the elements in the piezoelectric ceramic body. A post-fired motor, which was fired with silver electrode and again post-fired with LTCC, was prepared for better comparison. For the cofired sample, the scanning area of the stator was sectioned into two regions. One is a "dummy area," which is in direct contact with LTCC to sustain the stator structure. The other is an active region that is vibrating with motion in two dimensions.

Figure **6.8** shows SEM images and spectrum of the cofired motor. For investigation of inter-diffusion in the active region of the motor, the stator was cut into two pieces in the middle of the rectangular bar. The fracture surface of the motor is shown in figure **6.8** (a). A magnified image of piezoelectric ceramic is shown in figure **6.8** (b). Grains of the tape were smaller than that of the bulk samples. Numerous small pores were also observed in the tape which was not significant in bulk cases. The pores might be originated from a tape casting and a binder burn-out process. **6.8** (c) presents EDS spectrum of the cofired motor. The scanned spot was near to LTCC structure, therefore Al and Si concentrations are considerable.

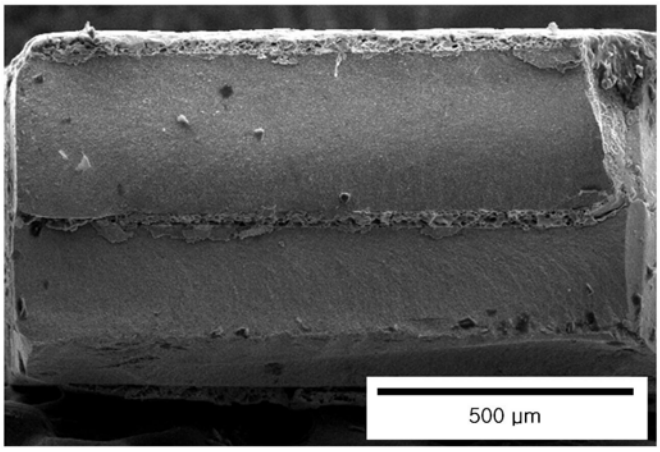

(a)

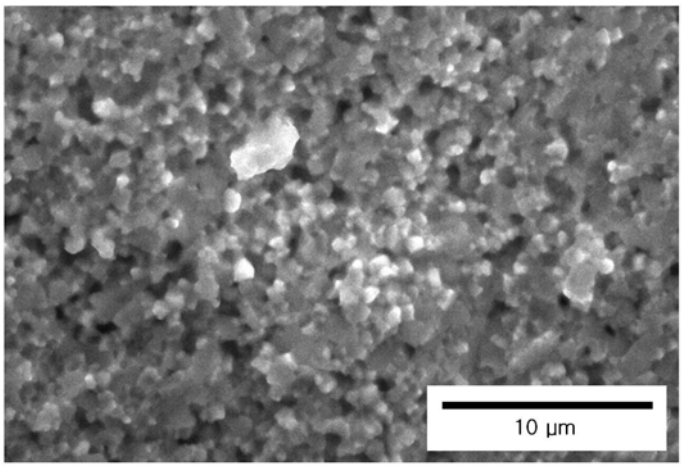

(b)

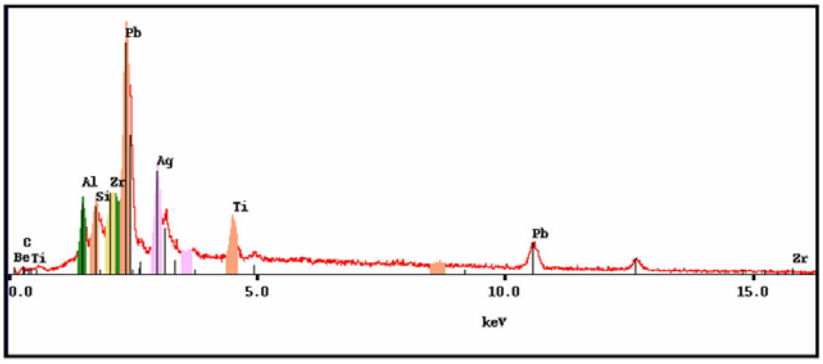

(c)

Figure **6.8**: SEM images and EDS spectrum of the cofired motor: (a) Fracture surface, (b) Piezoelectric Ceramic Film, (c) EDS spectrum of the piezoelectric film close to LTCC structure.

Figure **6.9** shows the silver concentration in the PZT ceramics. Post-fired samples, active, and inactive regions of the cofired samples showed similar silver concentrations of approximately 2 atomic %. Even so, silver migration occurred, and all the samples had concentration levels low enough to be poled owing to the low-temperature sintering condition. High silver concentrations at both ends of the graph are due to the existence of bottom and ground electrodes.

Figure **6.10** and **6.11** show major LTCC elements (Al and Si) in PZT ceramics due to diffusion. Clearly, the dummy region of the cofired samples contained more Al and Si compared to the post-fired samples or the active region of the cofired motor. Diffusion of LTCC materials into PZT was apparent. The cofired case showed a more severe diffusion problem than did the post-fired case. However, the active part of the motor is not directly touching the LTCC platform structure. Therefore, only the dummy region exhibited high Al and Si concentrations, while the active region in the cofired case showed similar Al concentrations to post-fired case, but there was no Si. In other words, even though diffusion is a problem in the cofiring process, it is not critical in this research, owing to the fact that the alignment package structure of the active region is not directly connected to LTCC. Details of the alignment package structure will be discussed in Chapter 7.

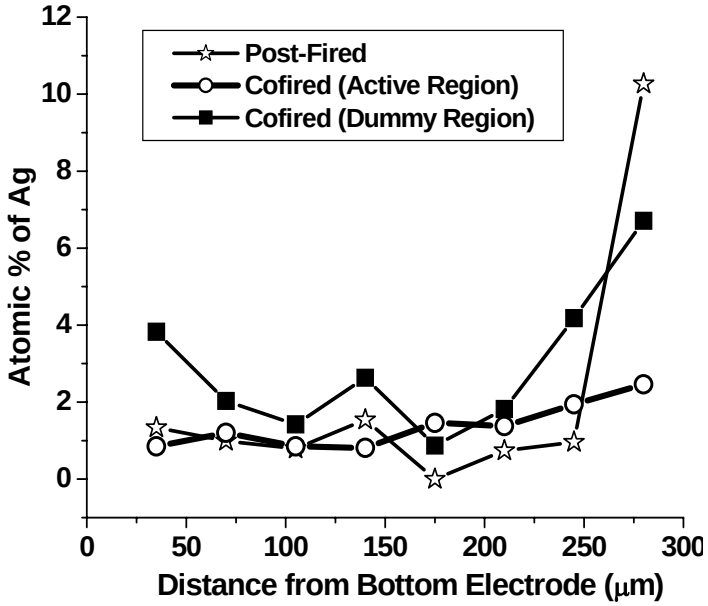

Figure **6.9**: Comparison of Ag concentration in the PZT ceramic.

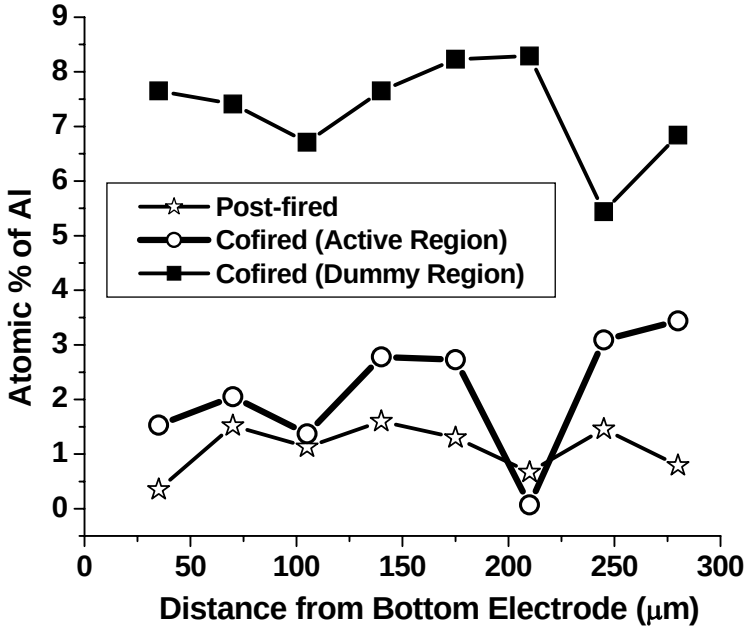

Figure **6.10**: Comparison of Al concentration in the PZT ceramic.

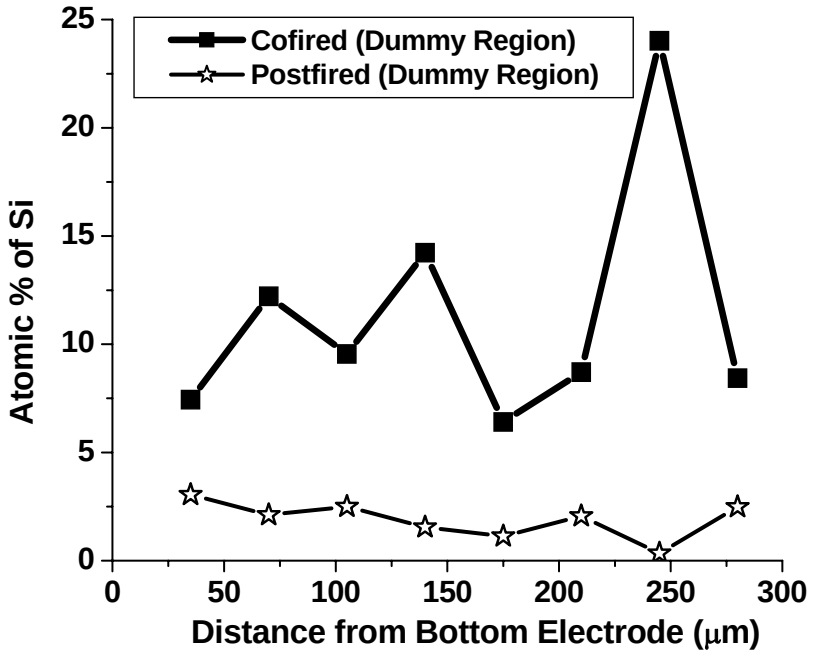

Figure **6.11**: Comparison of Si concentration in the PZT ceramic.

For electro-mechanical response comparisons, three kinds of samples were prepared. Cofired and post-fired samples were prepared in the same way and subjected to diffusion analysis with SEM EDS. Additionally, glued samples were prepared in which the motor and LTCC platform were sintered separately and then joined with epoxy.

Figure **6.12** shows impedance versus frequency curves for the samples. The impedance becomes minimum at resonance and maximum at anti-resonance. The mechanical quality factor (Q_m) is a parameter that characterized the sharpness of the electromechanical resonance spectrum [**11**]. The cofired motor, demonstrated in figure **6.12** (a), presented the sharpest and largest response with less noise when compared with

the other cases as shown in figure **6.12** (b) and (c). These results show that the cofired structure can provide a most stable and reliable platform structure to the motor for mechanical vibration.

Figure **6.13** shows displacement at the motor tip of a cofired sample. The largest elliptical motion was found in the frequency range of 20 kHz to 120 kHz with 60 V_{pp} driving voltage. The largest elliptical displacement was found at 86.1 kHz. This frequency is close to that of resonance, as shown in figure **6.12** (a).

The bottom line in this electromechanical response comparison is importance of the fabrication processes of platform structure for ultrasonic motors. One of the demerits of the ultrasonic motor is small displacement. To effectively transfer this motion to a rotor or a slider, a stable and reliable platform structure is essential which does not damp the mechanical vibration. In that sense, the cofired structure is an important contribution to the final performance of an alignment package, even though the gluing with epoxy is a simple and cheap method.

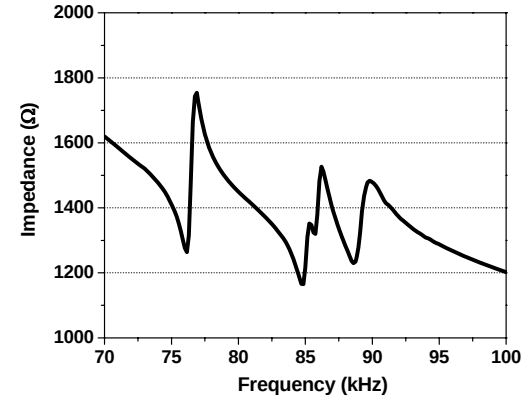

(a)

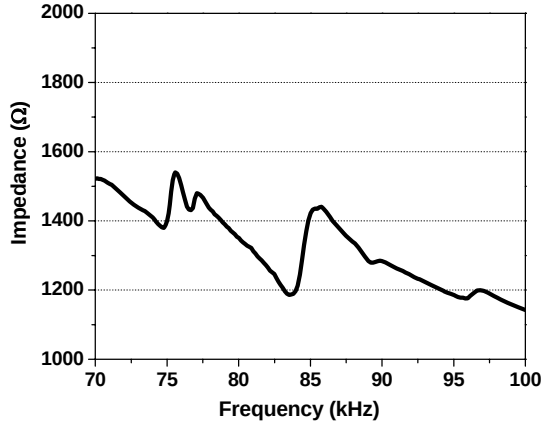

(b)

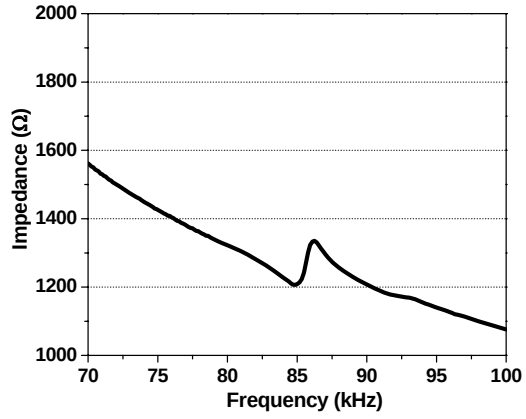

(c)

Figure **6.12**: Comparison of impedance versus frequency response: (a) cofired, (b) post-fired, and (c) glued motors.

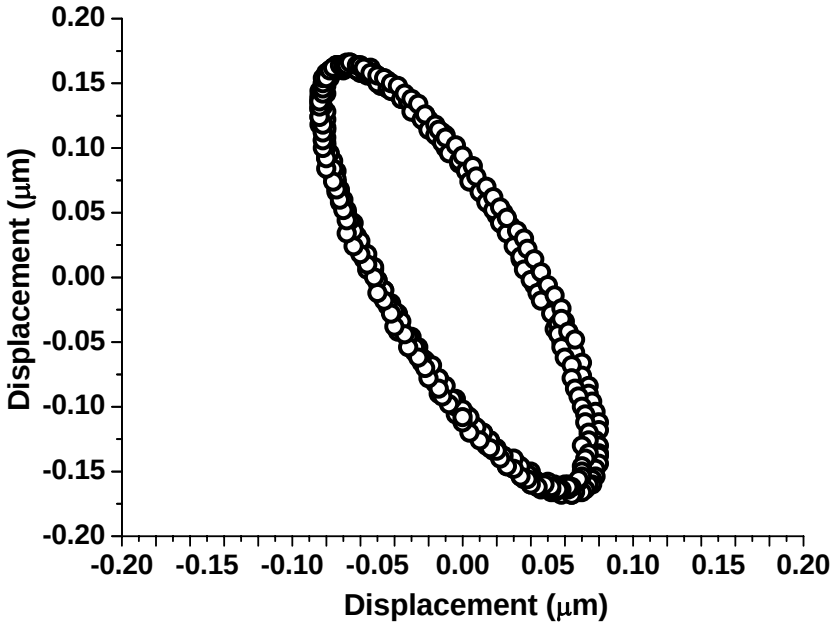

Figure **6.13**: Displacements at the tip of the cofired motor with 60 V_{pp} at 86 kHz.

Figure **6.14** and **6.15** show cofired motor characteristics. The electric field applied was 64 V_{rms} and frequency was fixed at 74 kHz. The pre-load varied in the range of 0.05-1.2 N. As the pre-load increased, the speed of the motor decreased and the torque increased. These trends are similar to that of other ultrasonic motors [**71**,**72**,**73**], even though magnitude of each parameter is different. When the pre-load was 0.54 N, the maximum efficiency of 4.1 % and the maximum output power of 14.4 mW were obtained. Under those conditions, the speed and the torque were 14.9 radians/sec and 0.96 mNm, respectively. The decreased performance of the motor, compare to the results in the Chapter 5, would be because of the size of the motor and the deterioration of material properties due to cofiring and the energy consumption of the driving circuitry.

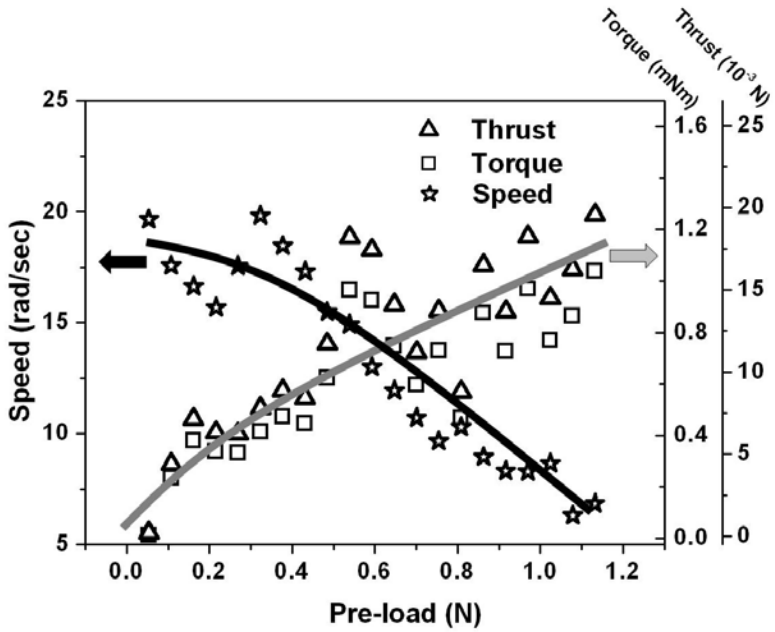

Figure **6.14**: Variation in speed, torque and thrust with pre-load conditions.

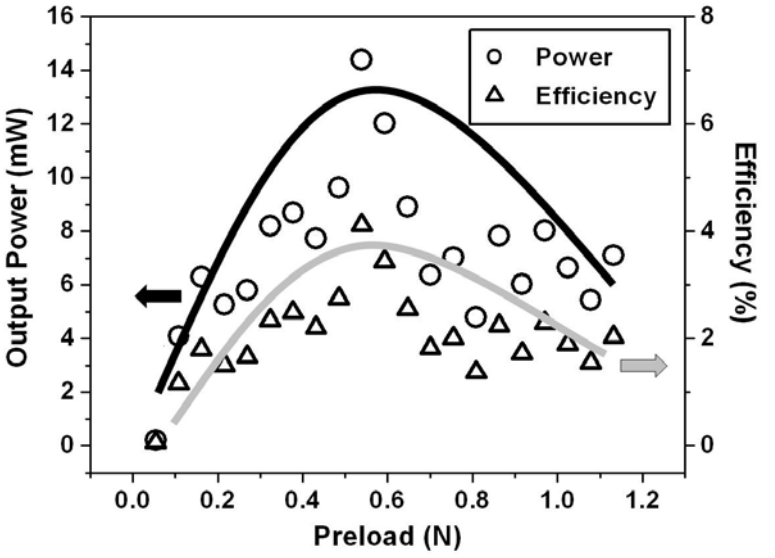

Figure **6.15**: Efficiency and output power change with various pre-load conditions.

6.5 Chapter Summary

The ultrasonic motor was successfully cofired with LTCC platform structure as well as silver electrode. Reducing the size of the motor and changing the ground electrode pattern provided a stable structure that can endure the stress induced by mismatched sintering characteristics among PZT ceramics, LTCC system, and the electrode material. Even though silver and LTCC components migrated into the PZT ceramic, it seemed not to be a major concern in this research case. The cofiring process produced a better housing structure than either the post-firing or gluing processes. The cofired motor showed rather lower performance compared to properties measured in Chapter 5. Nevertheless, the ultrasonic motor was cofired effectively with the LTCC system. The cofired motor characteristics along x-direction with driving conditions of 180 V_{pp} at 74 kHz are shown in the Table **6.1**.

Table **6.1**: The cofired motor characteristics.

Speed (rad/sec)	Torque (mNm)	Thrust (10-3 N)	Power (mW)	Efficiency (%)
14.9	0.96	18.1	14.4	4.1

Chapter 7

OPTICAL FIBER ALIGNMENT DEMONSTRATION AND CHARACTERIZATION OF INTEGRATED DELTA-MOTOR

7.1 Chapter Overview

This chapter presents a practical optical fiber alignment demonstration using an LTCC cofired piezoelectric ultrasonic motor. Based on the cofiring technique introduced in Chapter 6, an alignment package was designed to effectively transfer the 2-dimensional motions to an optical fiber. A pre-stressed structure with springs was used to enable the precise adjustment of the fiber's position and stable contact between a stator and a slider. A simple driving circuitry that can control the ultrasonic motor was prepared. Accurate alignment of the optical fiber was successfully performed by the control system. Alternative designs are also explored to consider a multi-fiber packages and search for more efficient ways to package the alignment assembly.

7.2 Package Design

Figure **7.1** shows the fundamental concept of the optical fiber alignment package. An optical fiber is connected to a slider that has an aperture. The operator can move the slider by controlling the delta motor with the aid of a developed driving control circuit. Consequently, the fiber can be aligned with the laser, another fiber, or a detector. The first prototype alignment package is shown in figure **7.2**. The prototype was coated with

silver electrode, and 1-mm-diameter zirconia media were used as bearings to reduce the power required to shift the slider.

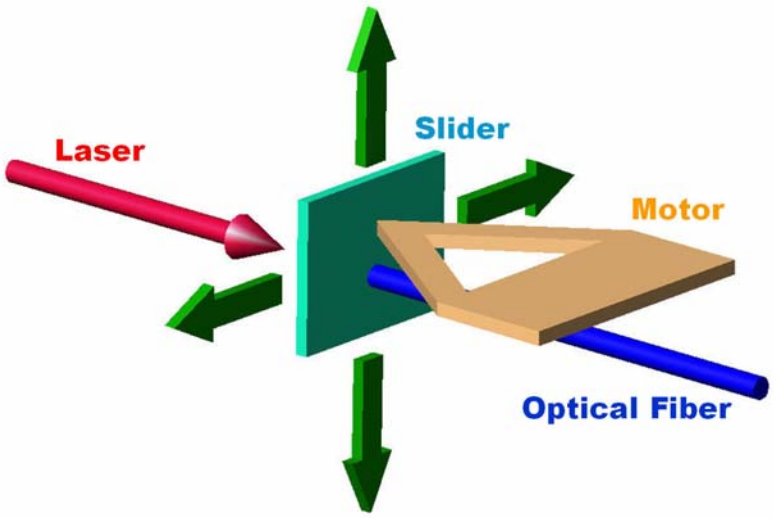

Figure **7.1**: The fundamental concept of the alignment system.

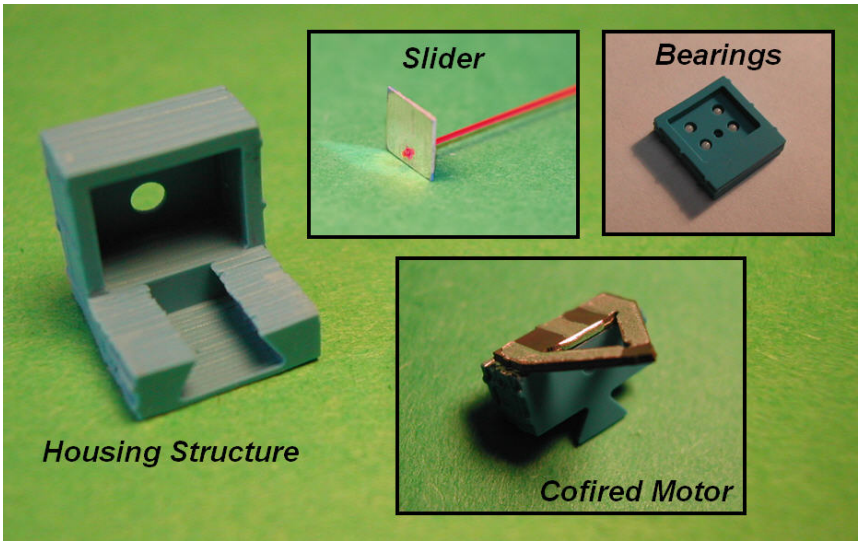

Figure **7.2**: The first prototype of the optical fiber alignment package.

Even though the first prototypes were successfully fabricated with the cofiring process, a balancing problem was encountered. This structure used only one spring, and the force from the spring was inadequate for achieving proper alignment with the motion of the motor. Hence the slider could not be controlled as intended. Figure **7.3** shows an improved design concept. For better stability, four springs were used, and the motor is touching the center of the slider.

Based on the design in figure **7.3**, a new optical fiber alignment package was fabricated, as shown in figure **7.4**. One of the problems with the previous design was the asymmetric structure of the cofired motor itself. As shown in Figure **7.2**, only one side of the motor is connected to the LTCC. Therefore, when the motor is driven with electric signals, induced vibration motions were not in a state of equipoise. Figure **7.4** (b) shows the stability-enhanced, cofired motor that is pressed by an upper and a lower LTCC platform structure. This design can provide asymmetric vibrating motions to the motor.

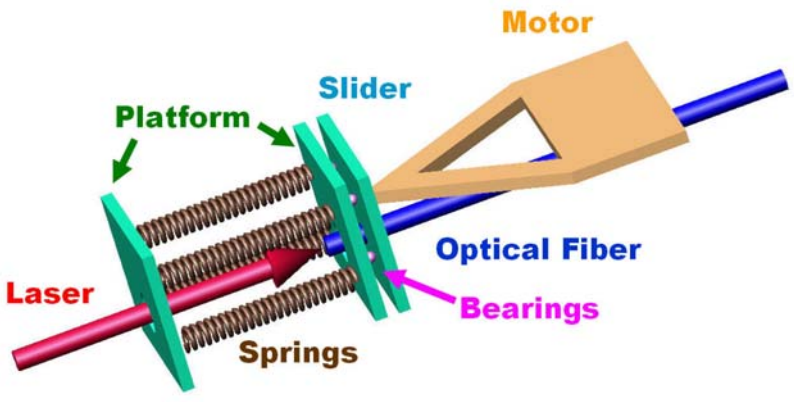

Figure **7.3**: The second design for the optical fiber alignment system for improved stability.

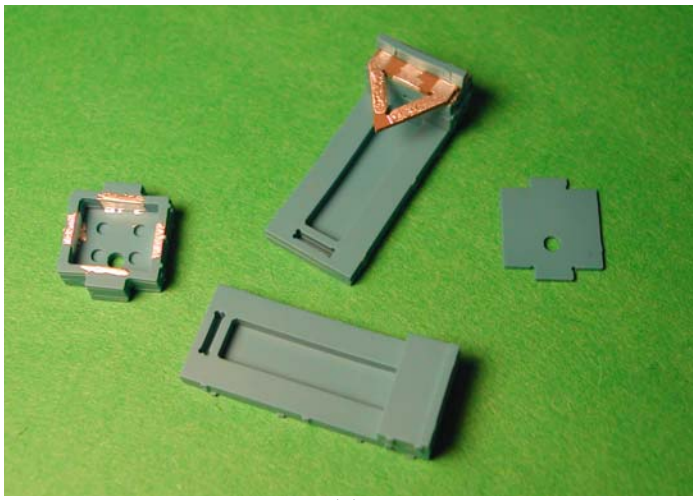

(a)

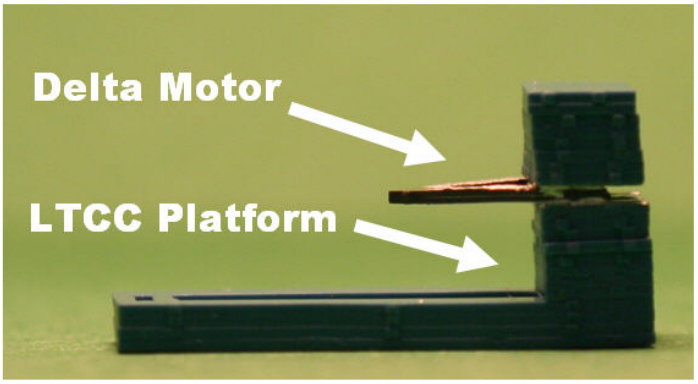

(b)

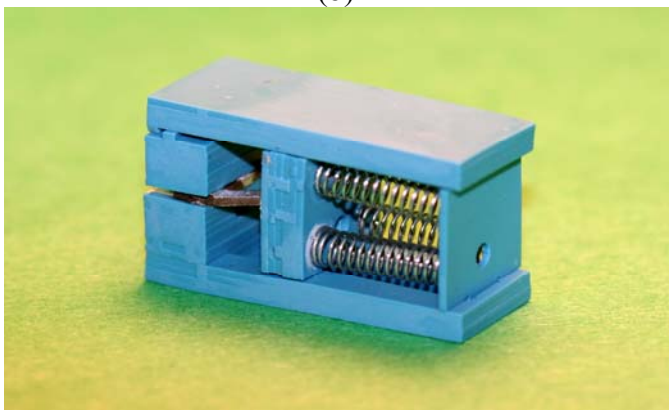

(c)

Figure **7.4**: A prototype with the second design: (a) cofired package part (b) side view of the cofired motor and (c) assembled optical fiber alignment package.

Figure **7.5** shows a multiple arrays of the optical fiber in an alignment package. Three optical fiber alignment systems were cofired together. This prototype showed possibilities of aligning several fibers sequentially at one time.

Figure **7.6** demonstrates a further improved optical fiber alignment package. In the second design of figure **7.4**, the active part of the motor was not directly connected to the LTCC platform structure, and this resulted in decreased property deterioration by inter-diffusion. However, this structure has a problem of bending during the cofiring process. As a solution for this issue, the motor's structure was inclined in the upper direction at an initial angle by inserting one or two layers of LTCC film under the motor. This solved the problem of bending, but the reproducibility of the product was not acceptable. This problem was resolved by again changing the design of structure, creating a third generation alignment package design. The motor was cofired with LTCC structure that has four holes for springs and one slit for the motor. The motor was placed in the slit before sintering, and the motor was held straight during the cofiring process by the squeezing force from sintering shrinkage. The size of the alignment package of the third design was reduced to approximately half of the size of the third design, as shown in figure **7.6** (c). This size reduction was made possible by using smaller springs and putting the springs into the holes in the cofired structure that was shown in figure **7.6** (b).

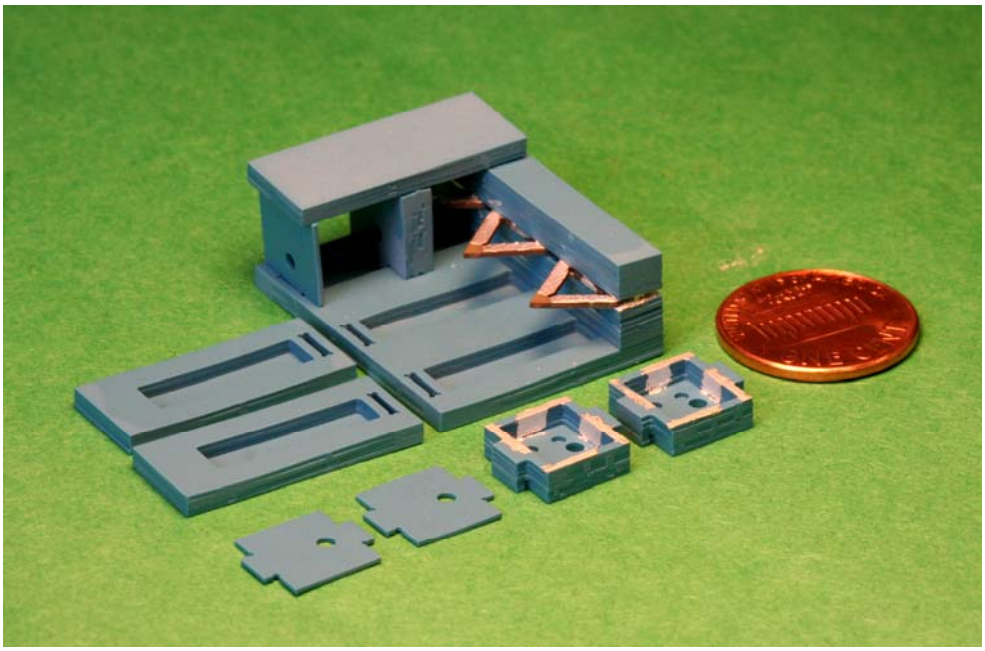

Figure 7.5: Multiple arrays of the optical fiber alignment package.

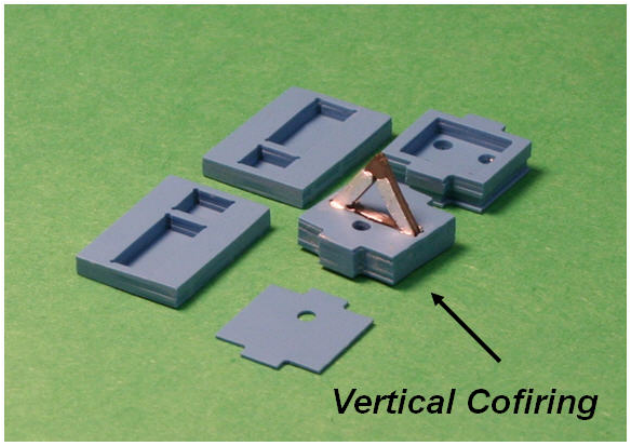

(a)

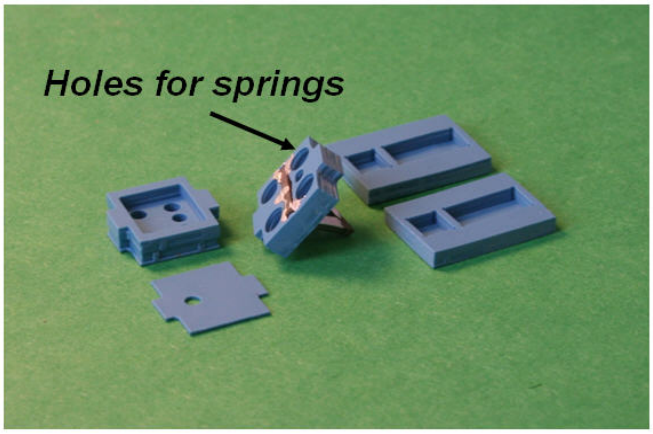

(b)

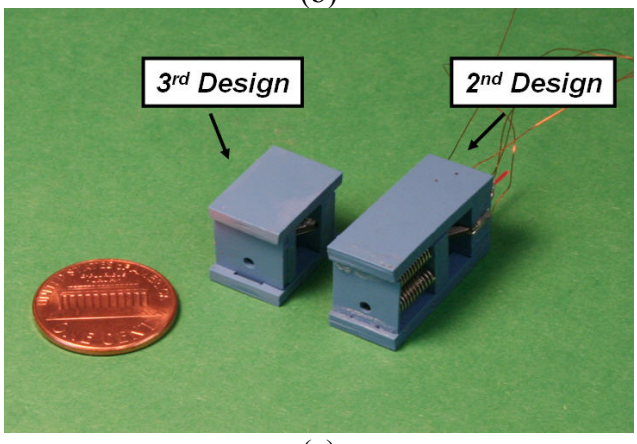

(c)

Figure **7.6**: The fabricated prototype with the third design: (a) showing a vertically cofired ultrasonic motor with other parts (b) back side of the cofired structure that has four holes for springs and (c) size comparison between the second and the third design.

7.3 Alignment Control and Results

Figure **7.7** shows a circuit diagram for optical fiber alignment. Basically, two signals with 90^o phase difference, i.e. sine and cosine, are required to control the motor. As explained in Chapter 5, the tip of the bimorph structure delta-shaped ultrasonic motor can move along x, z and diagonal directions depending on how two signals are allocated into four input electrodes of the motor.

Figure **7.8** demonstrates a prepared driving circuit that controls the optical fiber alignment package manually. A multi-phase oscillator (LTC 6902) generated two square shaped phases with 90^o phase difference from 5 VDC power. Low-pass filters were used to convert these phases into sinusoidal waves. These signals were magnified by high-speed power supplies and sent to relay switches. The switches were controlled by a computer through the parallel port using a buffer (SN54LS541). In figure **7.9**, a control panel for the optical fiber alignment system which was coded with Visual Basic as shown. There are a total of 8 relay switches to allocate cosine and sine signals for each of the 4 input electrodes of the optical fiber alignment package. The software can adjust travel the distance as well as the directions of the slider by controlling the relay switches. Details of the codes can be found in the Appendix A.

A practical alignment test was performed with the developed optical fiber alignment package. Figure **7.10** shows the laser-to-fiber alignment results. The alignment consisted of three steps: 1) a coarse alignment; 2) the location of an initial peak; and 3) a fine alignment. The coarse alignment step is a rough-scan process to find the initial peak point with large travel distance (several tens of μm range) of the slider. After locating the

initial peak point, the fine alignment process that has diminutive control distance (several hundreds of nm range) was used. A conventional hill-climbing concept, which analyzes a gradient of the intensity change, was applied to the overall alignment steps.

Figure **7.11** shows the intensity change of the laser with temperature variation. The temperature was increased after an optimum alignment position was found. Various fibers were used to evaluate their characteristics. A scintillating fiber showed poor temperature stability. The intensity of the laser decreased rapidly even with a small temperature increase. When the temperature reached 50 ^{o}C, permanent bending occurred in the scintillating fiber, i.e. the intrinsic stability of the fiber was the reason for laser intensity drop, not the packaged alignment system. The intensity of the general fibers was slightly enhanced as temperature increased. These results show one of the advantages of the developed optical fiber alignment package. Generally, the intensity of the laser decreases as temperature increases, due to thermal expansion (~ 10^{-5}/K) of the adhesive materials that are used to fix the fiber position [**74**]. In the developed alignment system case, the optical fiber is fixed to the slider that has an aperture that is precisely matched to the fiber's diameter. Furthermore, the thermal expansion coefficient of the LTCC tape (DuPont 951) is 5.8 ppm/K, which is an order of magnitude smaller than the expansion coefficient of the adhesive materials. Therefore, alignment deterioration with temperature change did not occur with the developed alignment system. The slight increase of the laser intensity is due to the distance between the fiber and the power meter sensor. It was observed that a small amount of change in the distance between a fiber and the detector causes variations in the feedback intensity. Therefore, longitudinal expansion of the fiber due to thermal strain could be the reason for the small increase in intensity.

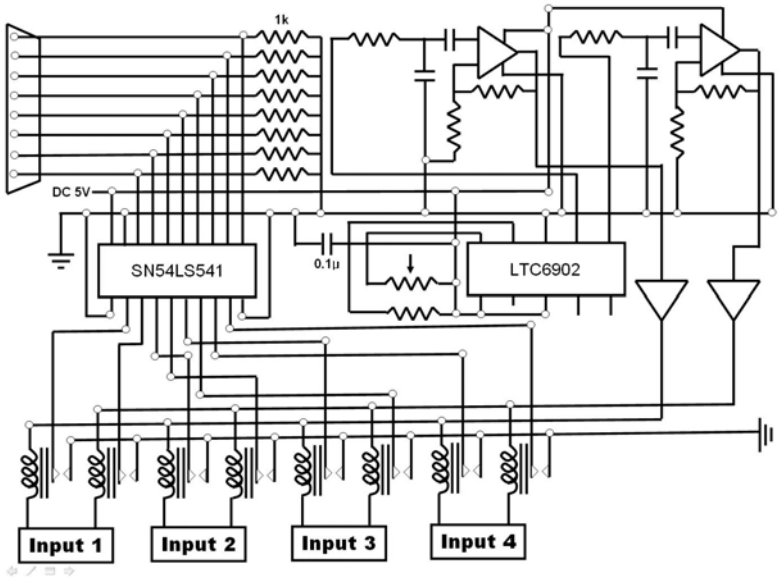

Figure **7.7**: The driving circuit diagram used in the optical fiber alignment control.

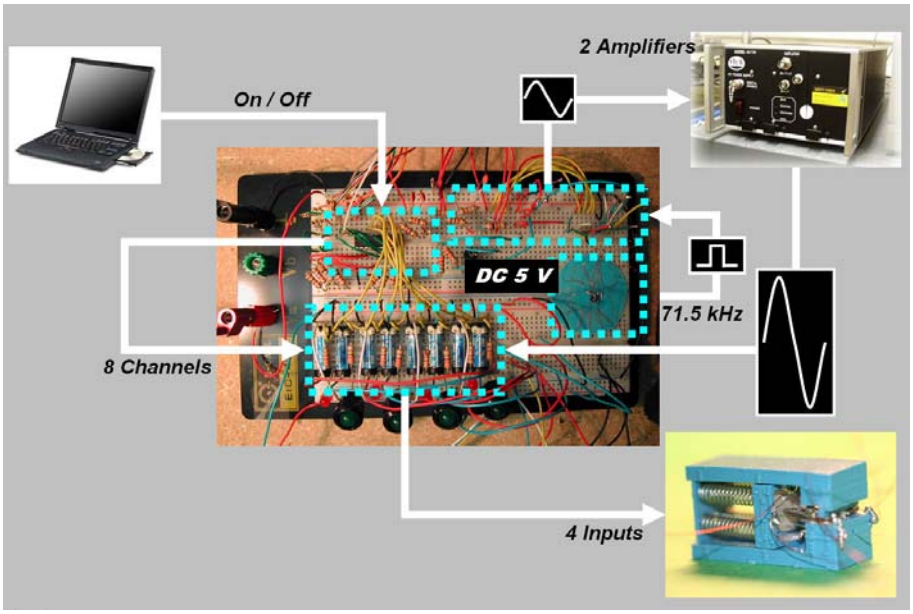

Figure **7.8**: Prototype of the actual driving circuit for alignment control, with key features outlined.

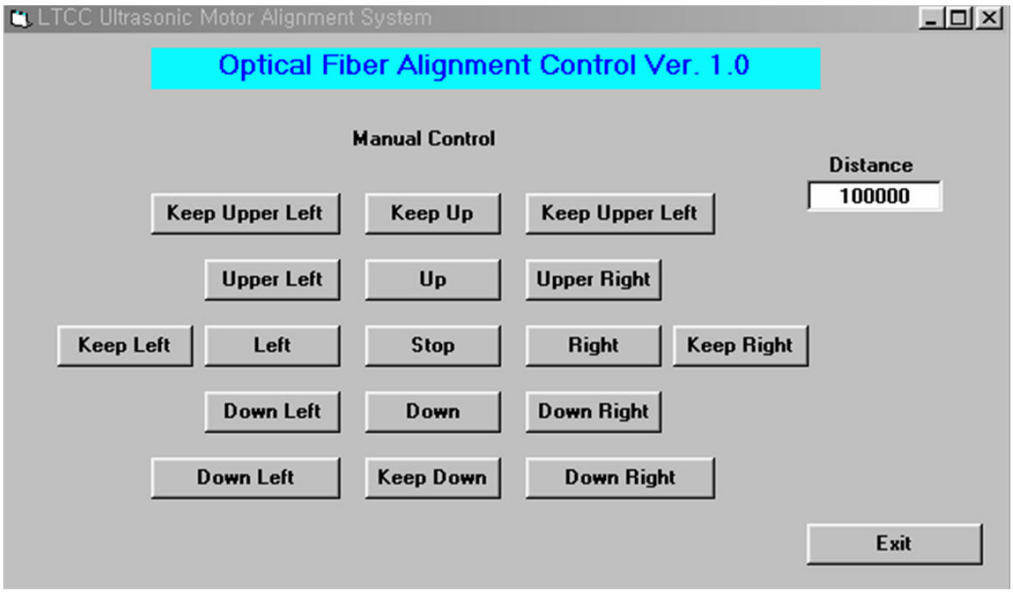

Figure **7.9**: Optical fiber alignment control panel.

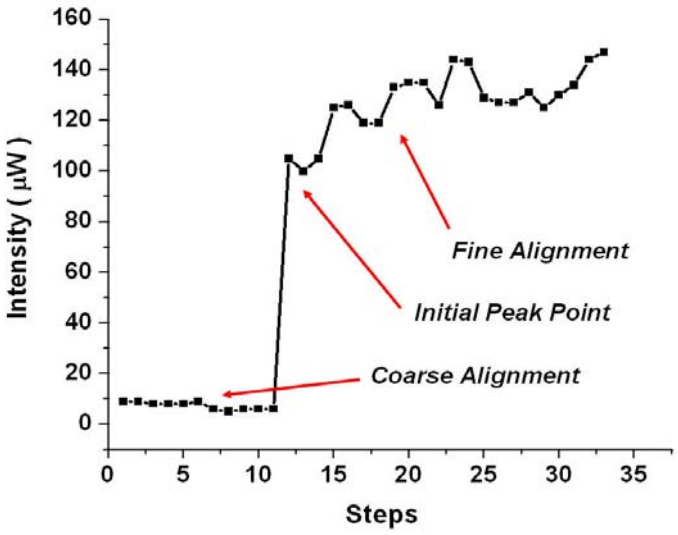

Figure **7.10**: Optical fiber-to-laser alignment results with the developed package (Steps: number of control signals sent to the alignment package).

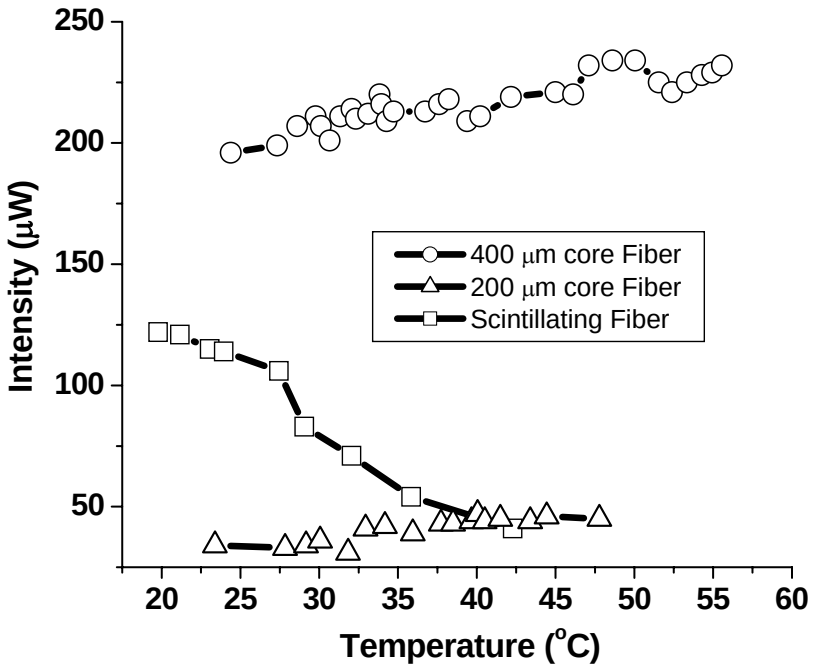

Figure **7.11**: Aligned laser intensity with temperature variation.

7.4 Chapter Summary

This chapter built upon all the technology that was outlined in the earlier chapters. In this chapter a prototyped package was built and redesigned a number of times to continuously improve package size and performance.

The piezoelectric delta motor was integrated and cofired into an LTCC package. The package was electrically controlled by a drive circuit. This drive circuit was also designed and built for this demonstration. The system demonstrated alignment between laser and fiber. In addition, temperature stability was also checked, and this was found to be as good as that of optical epoxy. But with the unique advantage of being able to re-align the fiber position, when misalignment happens, made developed alignment package promising optical component for full optical network.

Chapter 8

SUMMARY AND FUTURE WORK

8.1 Summary

This research was validated with a physical demonstration of a new active optical fiber alignment package system. It consists of a piezoelectric ultrasonic motor with two degrees of freedom and an LTCC platform structure that is pre-stressed by springs. This pre-stressed design provides a unique functionality that can readjust fiber position when misalignment occurs during installation or use. Power is only required to perform the readjustment.

The motor, housing structure, and silver electrodes were cofired. For this process, a composition was specially developed to provide a material that was sinterable at low-temperature and stable under high power driving conditions. The base composition was a perovskite based $Pb(Zr,Ti)O_3$-$Pb(Zn,Ni)NbO_3$ ceramic. Sb, Li, and Mn were substituted to enhance the high-power characteristics and make this composition a good basic material for low-temperature sintering. CuO was used as a sintering aid to lower the sintering temperature to 900 ^{o}C. The deterioration of piezoelectric properties was not significant.

This new composition was used for a ultrasonic motor with two degrees of freedom. The design of the motor was optimized with ATILA FEM simulation by changing various geometric aspects of the design, such an angle and width. The angle

change was an effective way to maximize the elliptical motion at the motor tip. The two degrees of freedom were obtained from bimorph structure, and the structural stability of the motor was enhanced by changing the motor shape from lambda to delta.

Camber and delamination were the major issues in the cofiring process. These problems were solved by changing the size of the motor and electrode pattern. For adhesion between piezoelectric and LTCC tapes, a silver electrode was used as a connecting element as well as a conducting material. The active part of the motor was not directly contacting the LTCC housing structure. Therefore the migration of LTCC elements into piezoelectric ceramic was minimal.

A final prototype, based on material development, device design, and fabrication process that included a control system was prepared. Preliminary optical fiber alignment tests were successfully performed, and reliability tests at various temperatures proved to have thermal stability equivalent to commercial resins but with the ability to re-align fiber position with minimal power consumption.

The optical fiber is the essential component required for high-speed data transmission, and optical fiber alignment is the bottleneck of the optoelectronics industry due to the laborious processes involved and their high costs. For the establishment of a high-speed network, an inexpensive and precise alignment system is required. The developed new alignment package provides a cost-effective way for active alignment with high precision and compact size. In addition, the re-alignment function of the package reduces the laborious processes and extends the lifetime of the optical network system. In conclusion, fast and reliable optical data communication will be widely possible, owing to this novel device.

8.2 Future Work

8.2.1 Further Investigation in High Power Characteristics

A Sb, Li, and Mn substituted $PbZrO_3$-$Pb(Zn,Ni)_{1/3}Nb_{2/3}O_3$- $PbTiO_3$ ternary system performed successfully as a base material for low temperature sintering. However its excellent piezoelectric properties can make this composition attractive to other high power applications which do not require low temperature sintering.

For better performance of this composition, an optimum sintering temperature should be found, because the sintering temperature was initially 1200 ^oC in this thesis. Sb and Li substitutions as well as $Pb(Ni,Nb)O_3$ relaxor in this system could have lowered the sintering temperature without any flux addition.

In this research, there was no PbO excess, which is generally used to compensate Pb volatilization, during a sintering process. An adequate amount of excessive PbO before or after calcination could enhance the properties.

8.2.2 Low Temperature Sinterable High Power Composition

A high-power composition containing 0.5 wt% CuO was sintered at 900 ^oC. The role of CuO as a sintering aid was clear, but it is not clear whether it acts as an acceptor or a donor, because both mechanical quality factor and piezoelectric properties saturated when the CuO concentration was greater than 0.5 wt%. Therefore compositions with more than 0.6 wt% CuO added should be investigated. In addition, variation of the

sintering temperature would provide better understanding about the role of CuO addition at low temperatures.

8.2.3 Miniaturization and Alignment Package Design

In the third design, shown in figure 7.6, the size of the optical fiber alignment package was reduced by half from the size of the previous design. Nevertheless, further miniaturization is possible by decreasing the motor size and developing smaller, effective bearings and springs. Eventually, developed motor could be integrated into the Micro Electro Mechanical Systems (MEMS). In this case, the delta-shaped structure can be also used as an actuator. Miniaturization is not only an issue of size, but price must also be considered, since the smaller the LTCC ceramics, the more inexpensive the product can be.

8.2.4 Alignment Control System

The currently prepared control system is only for a preliminary proof of concept. It has low efficiency and large size. Furthermore, additional power supplies are required. Therefore, further improvement and optimization of the circuit and control software are necessary.

The final control system should be portable and easy to be used to maximize the unique fiber position re-adjustability so the operator can fix the misalignment problem in

any place. For this, an automatic alignment algorithm needs to be integrated into the control system.

8.2.5 Other Applications of the Motor and Alignment System

Gymbal actuator

The developed piezoelectric ultrasonic motor can be used for the Gymbal actuator that can generate three dimensional motions. This can be achieved by combining the delta-shaped motor with a metal ball with bearings. Then two-dimensional motions at the motor tip can be transferred into the ball, enabling rotation in any direction. Figure **8.1** shows a concept of the idea. This "eye-ball" like device could be used for a surveillance camera that can scan wide area with small size and accurate control.

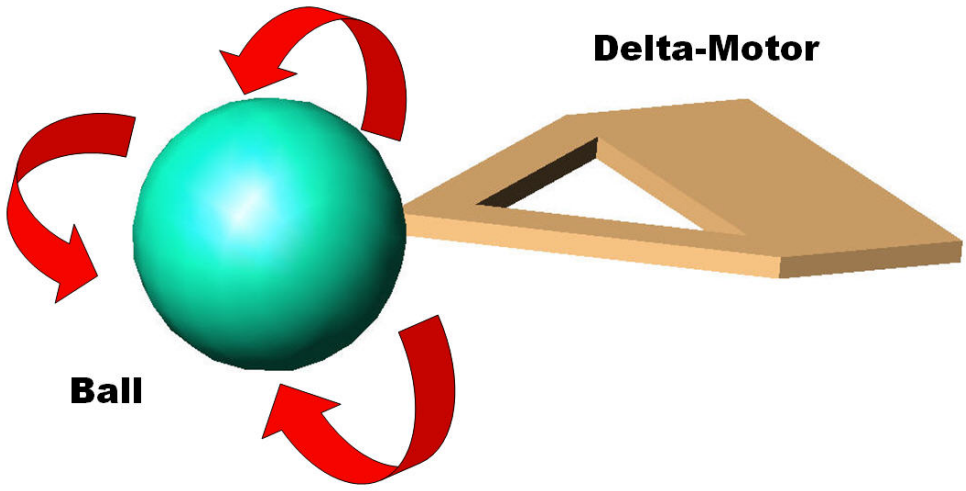

Figure **8.1**: A concept of 3-dimensional control with the delta-motor.

Nano-positioning stage

Owing to the high-speed and high-thrust characteristics of the developed ultrasonic motor, it can be used for the nano-positioning stage for micro machining. Furthermore, the motions with two degrees of freedom would reduce the price and the size of the stage.

On-board structure actuator

Currently, passive electronic components are integrated into substrates by LTCC technologies. Based on the developed cofiring techniques and materials, various actuators or ultrasonic motors can be integrated into the substrate.

Apparatus for fiber optics research labs

Many efforts have been made to align optical equipments in fiber optics research laboratories. The alignment system developed in this research could provide convenient alignment methods with a reasonably low price.

Bibliography

1. K. Uchino, J. R. Giniewicz: Micromechatronics (Marcel Dekker, New York, 2003)

2. K. Uchino, J. Zheng, A. Joshi, Y.H. Chen, S. Yoshikawa, S.Hirose, S. Takahashi and J.W. C. DE Vries: J. Electroceram. **2** (1998) 33.

3. B. Jaffe, J.W. Cook, and H. Jaffe, Piezoelectric Ceramics, Academic Press (1971)

4. F. D. Bloss, Crystallography and crystal chemistry (Holt, Rinehard and Winston, Inc. 1971)

5. Y. Xu, Ferroelectric materials and their applications (Elsevier Science Publishers 1991 New York)

6. R.C. Buchanan, Ceramic Materials for Electronics, New York, Marcel Dekker, Inc. (1991)

7. G. H. Haertling, Journal of American Ceramic Society, **82**, (1999) 797

8. A. J. Moulson and J. M. Herbert, Electroceramics, Cambridge, University Press (1990)

9. C. A. Randall, A. Kelnberger, G. Y. Yang, R. E. Eitel and T. R. Shrout: Journal of Electroceramics, **14** (2005) 1777

10. K. Uchino: Piezoelectric Actuators and Ultrasonic Motors (Kluwer Academic Publishers, Norwell, 1996)

11. K.Uchino: Ferroelectric Devices (Marvel Dekker, New York, 2000)

12. S. Kawashima, O. Ohnishi, H. Hakamata, S. Tagami, A. Fukuoka, T. Inoue and S. Hirose: Proc. IEEE Int'l Ultrasonic Srmp. France (1994)

13. M. Kondo, M. Hida, M. Tsukada, K. Kurihara and N. Kamehara: Ceram. Soc. Jpn. **105** (1997) 719

14. Y. Gao, Y. Chen, J. Ryu, K. Uchino and D. Viehland: Jpn J. Appl. Phys. **40** (2001) 687

15. S. Priya, K. Uchino, J. Ryu, C. Ahn and S Nahm: Appl. Phys. Lett. **83** (2003) 5020

16. C. Ahn, H, Song, S. Park, S. Nahm, K. Uchino, S. Priya, H. Lee and N. Kang: Jpn. J. Appl. Phys. **44** (2005) 1314

17. S. Takahashi: Jpn. J. Appl. Phys. **19** (1980) 771

18. P. G. Lucuta, F. Constantinescu and D. Barb: J. Am. Ceram. Soc. **68** (1985) 533

19. G. Zhilun, L. Longtu, G. Suhua and Z. Xiaowen: J. Am. Ceram. Soc. **72** (1989) 486

20. N. D. Patel and P. S. Nicholson: Am. Ceram. Soc. Bull. **65** (1986) 783

21. T. Yamamoto: Am. Ceram. Soc. Bull. **71** (1992) 978

22. S. Kaneko, D.Dong and K. Murakami: J. Am. Ceram. Soc. **81** (1998) 1013

23. X. Wang, K. Murakami and S. kaneko: Jpn. J. Appl. Phys. **39** (2000) 5556

24. T. Hayashi, T. Inoue and Y. Akiyama: Jpn. J. Appl. Phys. **38** (1999) 5549

25. L. Wu and C. H. Wang: Jpn. J. Appl. Phys. **32** (1993) 2757

26. D. E. Whittmer and R. C. Buchauan: J. Am. Ceram. Soc. **64** (1981) 485

27. S.-H. Park, Y.-D. Kim, J. Harris, S. Tuncdemir, R. Eitel, A. Baker, C. Randall, and K. Uchino: Proc. Actuator 2006, Bremen Germany, 2006, p. 432

28. H.V. Barh, IBM Technical Disclosure Bull., **16** (1973) 2263

29. R.A. Bizzigotti: U.S. Patent No. 3902085 (1975)

30. K. Uchino, K. Kato and M. Tohda: Ferroelectrics **87** (1988) 331

31. T. Bein, E. J. Breitbach and K. Uchino: Smart Mater. Struct. **6** (1997) 619

32. M. Kurosawa, O. Tsuchitoi and T. Higuchi: IEEE Transactions on. Ultrasonics and Ferroelectrics Frequency Control **45** (1998) 1188

33. Burhanettin Koc, A Thesis in Electrical Engineering, The Pennsylvania State University, U.S.A., 1999

34. M. Hu, S.-F. Liang, H. Du, and K.-H. Teo: IEEE Ultrason. Proc., San Juan, Puerto Rico, 2000, p. 667

35. M. Aoyagi, S. P. Beeby, and N. M. White: IEEE Trans. Ultrason. Ferroelectr. Freq. Control **49** (2002) 151

36. S. Shimoda, M. Ueyama, S. Matsuda, T Matsuo, K. Sasaki, and K. Itao: Proc. IEEE/RSJ Int. Conf. on Intelligent Robots and Systems, Maui Hawaii, U.S.A., 2001, p. 1972

37. C.-H. Yun, S. Niwano, J. R. Friend, K. Nakamura and Sadayuki Ueha: Jpn. J. Appl. Phys. **42** (2003) 3000

38. C. Zhao, Z. Li and W. Huang: Sensors and Actuators A **121** (2005) 494

39. C. A. Randall and J. P. Dougherty: The era of materials, The Pennsylvania academy of science (1998) 290

40. R. R. Tummala, J. Am. Ceram. Soc. **74** (1991) 895

41. Y. Imanaka: Multilayered low temperature cofired ceramics (LTCC) technology, Springer Science (2005)

42. M. Hrovat, J. Holc, S. Drnovsek, D. Belavic, J. Bernard, M. Kosec, L. Golonka, A. Dziedzic, and J. Kita: J. Mater. Sci. Lett. **22** (2003) 1193

43. M. Hrovat, J. Holc, S. Drnovsek, D. Belavic, J. Cilensek, and M. Kosec: J. Eur. Ceram. Soc. **26** (2006) 897

44. J. Juuti, A. Lozinski, S. Leppavuori: Sensors Actuators **110** (2004) 361

45. M. Zarnik, and D. Belavic: Proc. 6th Int. Conf. Therm. Mechanical and Multi-Phys. Simul. Exp. Microelectron. Micro Syst., Berlin, Germany, 2005, 338

46. L. F. Golonka, M. Buczek, M. Hrovat, D. Belavic, A. Dziedzic, H. Roguszczak, and T. Zawada: Microelentron. Int. **22** (2005) 13

47. Y. Tseng and T. Chang, "Active fiber-solder-ferrule alignment method for high-performance opti-electronic device pacakging", IEEE Trans. Components Packaging Tech., Vol **25**, No 3, pp. 541-547, 2003

48. J. Chun, Y. Wu, Y. Dai and S. Li, "Fiber optic active alignment method based on a pattern search algorithm", Optical Engineering, Vol. **45**, No. 4, pp.045005-1 – 045005-6, 2006

49. Z. Zhang, J. Liu, P. Zhao, G. Xiao and C. Grover, "Active alignment of optical fibers to planar waveguides using a thermal-curing adhesive", J. Lightwave Tech., Vol. 23, No. 2, pp. 567-572, 2005

50. H. Kosaka, M. Kajita, M. Yamada, Y. Sugimoto, K. Kurata, T. Tanabe and Y. Kasukawa: Electronics Letters, **32** (1996) 1991

51. M. Owen: IEEE Transactions on Advanced Packaging, **23** (2000) 182

52. Y. Kikuya, M. Hirano, K. Koyabu and F. Ohira: Optics Letters, **18** (1993) 864

53. P. Krulevitch, A. Lee, P. Ramsey, J. Trevino, J. Hamilton and M. A. Northup: J. Microelectromechanical Systems, **5** (1996) 270

54. S. Aoshima, N. Yoshizawa and T. Yabuta: IEEE Photonics Technology Letters, **4** (1992) 462

55. L.A. Field, D. L. Burriesci, P. R. Robrish and R. C. Ruby: Sensors Actuators A **53** (1996) 311

56. V.A. Henneken, M. Tichem and P.M. Sarro: Journal of Micromechatronics and Microengineering, **16** (2006) S107

57. R.E. Eitel, A.L. Baker, J. Agraz, M. Lanagan, K. Uchino and C.A. Randall: Proc. IMAPS/ACerS 1st Int. Conf., Baltimore, U.S.A., 2005, p. 20

58. J. M. Haake: U.S. Patent No. 5553182 (1996)

59. J. Tuominen, J. Lappalainen, J. Hiltunen, J. Ollila, and V. Lantto: J. Opt. A **8** (2006) S398

60. IEEE Standard on Piezoelectricity, The Institute of Electrical and Electron Engineers, Inc., (1987)

61. Y. Yamashita, N. Ichinose: Proc. 10TH IEEE Int'l Symposium on Applications of Ferroelectrics, East Brunswick, NJ, USA

62. Z. Zhu, B. Li, G. Li, W. Zhang and Q. Yin: Mater. Sci. Eng. B **117** (2005) 216

63. J. Yoo, C. Lee, Y. Jeong, K. Chung, D. Lee and D. Paik: Mater. Chem. Phys. **90** (2005) 386

64. C. Galassi, E. Roncari, C. Capiani and F. Craciun: J. Eur. Ceram. Soc. **19** (1999) 1237

65. J. Yoo, J. Hong and S. Suh: Sens. Actuators **78** (1999) 168

66. S. Seo, S. Lee, C. Yoon, G. Park and H. Kim: J. Am. Ceram. Soc., 87 (2004) 1238

67. C. Chen and H. Lin: Ceram. Int. **30** (2004) 2075

68. Y. Hou, M. Zhu, H. Wang, B. Wang, C. Tian and H. Yan: J. Eur. Ceram. Soc. **24** (2004) 3731

69. C. –W. Ahn, H. –C. Song and S. Nahm, S. Priya, S. –H. Park, K. Uchino, H. –G. Lee and H. –J. Lee: J. Am. Ceram. Soc. **89** (2006) 921

70. S. Takahashi and S. Hirose: Jpn. J. Appl. Phys. **32** (1993) 2422

71. K. Nakamura, M. Kurosawa, H. Kurebayashi and S. Ueha: IEEE Trans. Ultrason. Ferroelectr. Freq. Control **38** (1991) 481

72. Kenji Uchino: Smart Materials and Structures **7** (1998) 273

73. S. Cagatay, B. Koc and K. Uchino: IEEE Transactions on Ultrasonics, Ferroelectrics and Frequency Control, 50 (2003) 782

74. N. Murata: Proceedings 48th Electronic Components and Technology Conference, Seattle, WA, USA (1998) pp 1178

Appendix A

ALIGNMENT PACKAGE CONTROL PROGRAM CODES

```
'General_Declarations'
Dim distance As Long            'distance control

Private Sub cmdExit_Click()
  vbOut 888, 0
  Unload Me
End Sub

Private Sub Command1_Click()
Dim x As Integer
distance = Dis.Text
 For x = 1 To distance
    vbOut 888, 105
  Next x
vbOut 888, 0
End Sub

'Private Sub Command10_Click()
    vbOut 888, 90
```

```
End Sub

Private Sub Command10_Click()
    vbOut 888, 90
End Sub

Private Sub Command11_Click()
vbOut 888, 165
End Sub

Private Sub Command12_Click()
vbOut 888, 105
End Sub

Private Sub Command13_Click()
    vbOut 888, 150
End Sub

Private Sub Command14_Click()
Dim x As Long
distance = Dis.Text
  For x = 1 To distance
vbOut 888, 101
```

```
    Next x
vbOut 888, 0
End Sub

Private Sub Command15_Click()
Dim x As Long
distance = Dis.Text
  For x = 1 To distance
vbOut 888, 149
    Next x
vbOut 888, 0
End Sub

Private Sub Command16_Click()
Dim x As Long
distance = Dis.Text
    For x = 1 To distance
      vbOut 888, 89
    Next x
   vbOut 888, 0
End Sub

Private Sub Command17_Click()
```

```
Dim x As Long
distance = Dis.Text
    For x = 1 To distance
     vbOut 888, 86
    Next x
   vbOut 888, 0
End Sub

Private Sub Command2_Click()
Dim x As Long
distance = Dis.Text
  For x = 1 To distance
      vbOut 888, 150
    Next x
vbOut 888, 0
End Sub

Private Sub Command3_Click()
Dim x As Long
distance = Dis.Text
    For x = 1 To distance
      vbOut 888, 165
    Next x
```

```
  vbOut 888, 0
End Sub

Private Sub Command4_Click()
Dim x As Long
distance = Dis.Text
 For x = 1 To distance
    vbOut 888, 90
  Next x
vbOut 888, 0
End Sub

Private Sub Command5_Click()
vbOut 888, 89
End Sub

Private Sub Command6_Click()
vbOut 888, 86
End Sub

Private Sub Command7_Click()
vbOut 888, 149
End Sub
```

```
Private Sub Command8_Click()

vbOut 888, 101

End Sub


Private Sub Command9_Click()

vbOut 888, 0

End Sub
```

Nomenclature

k: Electromechanical coupling factor

d: Piezoelectric constant

Q_m: Mechanical quality factor

v_0: Vibration velocity

$\varepsilon^T_3/\varepsilon_0$: Relative dielectric permittivity

w: width of the motor

Θ: angle of the motor

LTCC: Low temperature cofired ceramics

FEM: Finite element methods

VITA

SEUNG HO PARK

Seung Ho Park was born on July 23, 1977, in Seoul, Korea. In 2000, He received Bachelor of Science degree in Materials Science and Engineering from Korea University, Seoul, Korea. He got Master degree in Materials Science and Engineering in the same university in 2004. His major research topic during master degree was piezoelectric materials development and expanded his perimeter of interests to piezoelectric device design and control when he enrolled Intercollege Graduate Degree Programs in Materials in 2005. His graduate work has been supported and funded by International Center for Actuators and Transducers (ICAT), Center for Dielectric Studies (CDS), Center for Optical Technologies (COT) and Office of Naval Research (ONR).